# MODELLING THE EVOLUTION OF KARST AQUIFERS IN THREE DIMENSIONS

Conceptual models and realistic scenarios

Inauguraldissertation
zur Erlangung des Doktorgrades Dr. rer. nat.
am Fachbereich Geowissenschaften
im Institut für Geologische Wissenschaften
der Freien Universität Berlin

vorgelegt von
Diplom Geowissenschaftler (Angewandte Geophysik)
**Thomas Hiller**

Berlin 2013

Erstgutachter: Prof. Dr. Georg Kaufmann
Zweitgutachter:Prof. Dr. Martin Sauter

Tag der Disputation: 11. Februar 2013

# Erklärung

Hiermit versichere ich an Eides statt, daß ich die vorliegende Arbeit selbstständig verfasst und keine anderen als die angegebenen Quellen und Hilfsmittel benutzt habe.

Berlin, den 23. Oktober 2012

Thomas Hiller

# Abstract

This work presents the development of three–dimensional karst evolution models for various settings and conditions. As karst aquifers are very sensitive to changes of their hydraulic boundary conditions a comprehensive understanding of the governing processes inside a karst aquifer is indispensable. Especially if a karst aquifer is influenced by anthropogenic utilization like e.g. the construction of a dam–site, the resulting changes inside the aquifer need to be understood as good as possible to prevent any unpredictable incidents. The use of numerical models to simulate the development of a karst aquifer is therefore a suitable tool in the preliminary investigations. It will be shown that simple three–dimensional dam–site models can be used to evaluate the parameters that control the karst aquifer evolution. Based on these simple models an enhanced three–dimensional model of a real dam–site is developed. This model is used to simulate the evolution of the aquifer close to this dam–site and to expose how the construction of the dam influenced the nearby bedrock significantly. It is shown that the karstified zone around the dam–site is the reason for the subsidence of an adjacent highway. The presented numerical results can be verified by field observations.

Additionally to the dam–site models a three–dimensional model approach is presented that describes the formation of large collapse dolines. Collapse dolines are significant surface features of karst landscapes and their evolution which is usually linked to a subsurface karst system is of high interest in the karst community. To simulate the evolution and interaction of such a doline system, a three–dimensional model with several spatially distributed dolines is used. There, based on the concept of a mechanically weakened crushed zone, the evolution over time is presented. The applied collapsing mechanism used in this work also allows to estimate the bedrock removal and surface lowering over time. The determined rates are in good agreement with values reported in literature.

# Zusammenfassung

Die vorliegende Arbeit beschreibt die Entwicklung von dreidimensionalen Karst – Evolutions – Modellen für variierende Konfigurationen. Da Karstaquifere sehr empfindlich auf Veränderungen ihrer hydraulischen Randbedingungen reagieren, ist ein umfassendes Verständnis der Prozesse innerhalb eines Karstaquifers unverzichtbar. Insbesondere bei anthropogener Nutzung eines Aquifers, wie z.B. dem Bau eines Staudammes, müssen die sich daraus ergebenden Veränderungen so detailliert wie möglich untersucht werden, um unvorhersehbare Zwischenfälle zu verhindern. Die Verwendung von numerischen Modellen, um die Entwicklung eines Karstaquifers zu simulieren, ist daher ein geeignetes Instrument in der Vorerkundung betreffender Gebiete. Diesbezüglich zeigt diese Arbeit, dass mit Hilfe einfacher dreidimensionaler Damm Modelle die Parameter, welche die Aquiferevolution steuern, untersucht werden können. Ausgehend von diesen einfachen Modellen wird ein erweitertes dreidimensionales Modell eines echten Staudammes präsentiert. Dieses Modell wird verwendet, um die zeitliche Entwicklung des Aquifers unterhalb dieses Dammes zu simulieren. Darüber hinaus werden die signifikanten Änderungen am anstehenden Gestein, verursacht durch den Bau des Staudammes, dargelegt. Es erweist sich, dass die entstandene verkarstete Verwitterungszone der Auslöser für die Absenkung der angrenzenden Autobahn ist. Die hier vorgestellten numerischen Ergebnisse stehen in gutem Einklang mit den Ergebnissen der Geländemessungen.

Zusätzlich zu den Damm Modellen wird ein dreidimensionales Modell, dass die Entstehung von großen Einsturzdolinen beschreibt, vorgestellt. Einsturzdolinen sind signifikante Oberflächenmerkmale von Karstlandschaften und von großem Interesse für die Karst Gemeinschaft, da ihre Entwicklung und Entstehung im Regelfall eng mit unterirdischen Karstsystemen verknüpft ist. Um die Entstehung und Interaktion von Einsturzdolinen zu untersuchen, wird ein dreidimensionales Modell mit mehreren räumlich verteilten Dolinen verwendet. Mit diesem Modell wird,

basierend auf dem Konzept einer räumlich begrenzten und mechanisch geschwächten Störungszone als initiale Bedingung für die Entstehung einer Einsturzdoline, ihre zeitliche Entwicklung präsentiert. Der in dieser Arbeit verwendete Einsturzmechanismus erlaubt eine realistische quantitative Aussage über die durch Lösungsprozesse entfernte Gesteinsmenge und der daraus resultierenden Oberflächenabsenkung. Die ermittelten Werte sind in guter Übereinstimmung mit den bekannten Literaturwerten.

# Contents

# Chapter 1

# Introduction

Karst landscapes can be found on every continent on Earth and so it is no wonder that $\approx 25\%$ of the world's population is dependent on drinking water stored inside karst aquifers (Ford and Williams, 2007). Therefore, it is natural to assume that karst landscapes have been the living environment for humans since thousands of years and that there is an inherent need to understand the processes acting in those regions. The oldest known explorations of karst landscapes date to the times of Assyrian kings around 1100 BC (Ford and Williams, 2007) and until today many questions regarding their development are unanswered. Karst landscapes show very unique surface characteristics like steep valleys and surface depressions. But without a doubt the most fascinating karst landscape features are hidden in the subsurface, the karst caves. The history of karst sciences is closely connected with the discovery and exploration of karst caves ranging from passages not much higher than a few decimeter up to large chambers which are several tens of meters high. Most of the features typical to karst regions, on the surface and subsurface, can be found on the *Kras* plateau in southeast Europe. This plateau is not only the linguistic origin of the name *karst*, but also for other typical karst landforms like e.g. poljes (large flat depressions), ponors (flat *sinkhole–like* swallow holes where a surface stream disappears into the ground) or dolines (valleys created by e.g (sub)surface dissolution and / or collapse).

Because karst bedrocks consist of dolostone (dolomite $CaMg(CO_3)_2$), gypsum ($CaSO_4 \cdot 2H_2O$), limestone (calcium carbonate $CaCO_3$) or salt (e.g. halite $NaCl$) they are all prone to dissolution by water and hence water is the main driving force for karst landscape evolution. Of course several other parameters beside the pure presence of water have to be active to create a karst landscape. In the case of e.g. limestone, which is the major karst bedrock, water has to be enriched by carbon dioxide ($CO_2$) as the rate of dissolution is controlled by the ternary system calcite–carbon dioxide–water. For the creation of a karst cave system the host rock should also have a kind of tectonic history. Water needs sufficiently large pathways (network of fissures) to flow through the rock and enlarge these fissures by dissolution. Note that sufficiently large is still in the sub–millimeter range. Finally, also the amount of available water in terms of groundwater recharge is important because the flow through the bedrock induced by pressure differences is either controlled by precipitation, so water entering from the surface, or the groundwater level in the subsurface.

As karst landscapes are widely spread around the globe they are of course also influenced by anthropogenic use. Not only in karst regions dam–sites play an important role in supplying water to humans, be it as drinking water, for agriculture or as energy source. But in karst regions the impact of dam–sites on the environment can be substantial because karst aquifers are heterogeneous geological formations exhibiting complex hydraulic properties and are very sensitive to environmental changes (Ford and Williams, 2007). When water is impounded in large reservoirs, the local aquifer system can change dramatically and a lot of effort is needed to protect not only the dam structure itself but also the surrounding area and nearby facilities. If in the pre–construction phase of a dam–site the local karst system is not thoroughly investigated, constructional faults can lead to hazardous failures of the dam. The costs caused by these failures may be not only economically high. Often, the sensitive ecosystem inside a karst aquifer is threatened or even destroyed or, in the worst case, the loss of human lives is to bemoaned. There are numerous events in literature documenting the aforementioned consequences e.g. (Milanović, 2000, 2004). Therefore, there is an essential interest to understand the complex interactions inside a karst aquifer and especially when the human impact on this sensitive system can not be neglected. Generally, only mature karst systems with an accessible cave system can be explored by humans. But because the early evolution of a karst aquifer, when it cannot be directly investigated, is of substantial importance for its future development, people have started to study karst aquifers by numerical means. In the following a short overview on these efforts shall be given.

## 1.1 Historical abstract on karst evolution modelling

During the last decades, several numerical models concerned with the evolution of karst aquifers have been developed.

If one wants to model the evolution of a karst aquifer, it is of course necessary to understand and simulate the dissolution process inside the karst bedrock. In the early 80's of the last century Buhmann and Dreybrodt (1985a) have developed a numerical model for the aforementioned ternary system calcite–carbon dioxide–water that describes the dissolution of calcite. They have shown that for the open system (carbon dioxide can be exchanged with the atmosphere) as well as for the closed system (Buhmann and Dreybrodt, 1985b) the dissolution rate depends linearly on

the calcium concentration in the water. For the open system these results could be verified experimentally by Dreybrodt et al. (1996). An extension of the work by Buhmann and Dreybrodt (1985a) has been presented by Kaufmann and Dreybrodt (2007) which overcomes some limitations of the earlier works. For calcium concentrations close to equilibrium Plummer et al. (1978) has shown that this linear dependence no longer holds and the calcium concentration drops by several orders of magnitude. This was later also experimentally verified by Svensson and Dreybrodt (1992) (open system) and Eisenlohr et al. (1999) (closed system). In summary this means that depending on the calcium concentration in the water different linear and non–linear dissolution rate laws need to be considered (this will be shown in more detail in chap. 2).

Based on the numerical models for calcite dissolution, one–dimensional models that describe the evolution of a single channel or fracture have been presented by e.g. (Huyakorn et al., 1983; Dreybrodt, 1990, 1992, 1996; Palmer, 1991; Groves and Howard, 1994b; Dreybrodt and Gabrovšek, 2000; Gabrovšek, 2000). These one–dimensional models have shown the importance of the non–linear high order dissolution kinetics close to equilibrium for the enlargement of a single channel over time. By varying the parameters that drive the evolution of a single channel like e.g. geometry, flow rate, and calcium concentration a relation was found that combined those parameters and could characterize the evolution of a single channel over time — the one–dimensional breakthrough equation. This relation which defines the so–called *breakthrough time* (Dreybrodt, 1996) will also be explained later in the theory chapter (chap. 2).

The one–dimensional models were then extended into the second dimension (Groves and Howard, 1994a; Howard and Groves, 1995; Hanna and Rajaram, 1998; Siemers and Dreybrodt, 1998; Kaufmann and Braun, 1999, 2000; Kaufmann, 2002, 2003a,c, 2005; Gabrovšek and Dreybrodt, 2000, 2001; Bauer et al., 2002, 2003; Romanov et al., 2003c; Dreybrodt et al., 2005). First, the early evolution of two–dimensional fracture networks was studied with simple constant head boundary conditions, while later on also the importance of recharge boundary conditions was discovered. With these recharge boundary conditions the evolution of more natural cave networks could be simulated. In the progress of the further development of the two–dimensional models more complex fracture networks, model setups and boundary conditions were applied. Furthermore, the porous matrix was incorporated into

several models as it was found that the matrix flow component is also important for the early evolution of a karst aquifer.

With the increasing availability of computational resources the focus is now shifted on the three–dimensional modelling (Annable, 2003; Kaufmann, 2009; Kaufmann et al., 2010). Introducing a third dimension makes it now possible to take into account the complex geometry of a karst aquifer system, and therefore create more realistic model setups. This work is the logical follow up of the latest three–dimensional models. It shows the development of three–dimensional models for the evolution of karst aquifers for different models under different conditions.

## 1.2 Structure of the thesis

**Chapter 2 – Theory** In this chapter the basic processes governing the simulation of a karst aquifer are explained by means of a single conduit evolution. The reaction kinetics needed for the dissolutional widening and the resulting change of flow parameters are explained. In a next step the integration of the single conduit concept into a three–dimensional network is presented.

**Chapter 3 – Conceptual dam–site models** This chapter introduces the topic of three–dimensional karst evolution modelling of reservoirs or dam–sites respectively. First, simple models are presented and the governing model parameters and their influence on the evolution of the aquifer is investigated by means of a sensitivity analysis. In a next step the simple 3D models are further enhanced by implementing non–uniform (statistical) conduit networks and topography. This chapter gives the theoretical groundwork for the study of a real case scenario.

**Chapter 4 – A real dam–site scenario** Here, a three–dimensional karst evolution model is developed for a real dam–site in Switzerland. There, a small dam–site has caused subsidence of an adjacent highway and the objective is to support the findings from field observations by means of numerical modelling. Also a possible future evolution of the aquifer is presented and discussed.

**Chapter 5 – Collapse dolines** This chapter addresses the three–dimensional modelling of a typical surface characteristics of karst landscapes — large collapse dolines. Here, the concept of a breakdown or crushed zone is used to simulate

the early evolution of such dolines. Furthermore, the material removal rates are estimated by a novel collapsing mechanism and the interaction of spatial distributed collapse dolines is examined.

**Chapter 6 – Summary & Outlook** Finally, this chapter summarizes the findings of this work and gives an outlook on the future development of karst evolution modelling.

**Appendix A** Here, the benchmarks that have been carried out to test the performance of KARSTAQUIFER are presented and discussed.

**Appendix B** Appendix B holds additional plots for chapter 5.

**Appendix C** The program KARSTTOOL is introduced and its basic use is exemplarily described.

Chapter 2

# Basic theory of karst evolution modelling

The term karstification generally describes the alteration of a soluble bedrock such as limestone or gypsum by means of dissolution. Water can penetrate from the bottom of a reservoir or a river into the bedrock through a fine network of fissures. With time water circulates through the rock, removes material and therefore the fissures are widened to fractures or conduits. In general, modelling karstification can be partitioned into three major sub–steps. The first one is to calculate the flow of water through the rock depending on the hydraulic conductivity of the rock and the head pressure of the impounded water. The second step is to calculate the transport of the dissolved species in the subsurface water. And finally in the last step the dissolutional widening determined by flow and calcium concentration is derived. To describe briefly the basic principles of karst evolution modelling this chapter is structured as follows. First, the evolution of a 1D single conduit is introduced as it is the foundation on which the 3D modelling is build on. Therefore, the flow through a conduit and the reaction kinetics that control the chemical dissolution and therewith the evolution are shown. Finally, the 1D conduit is embedded into the 3D domain and the simulation process is briefly described.

As only the basic theoretical concepts are shown, references to the relevant literature is given at the corresponding sections.

## 2.1 The evolution of a single conduit

The evolution of a 1D single conduit depends on several physical and chemical parameters. Flow through a conduit is controlled by the pressure difference between entrance and exit and its hydraulic conductivity which is determined by its geometrical shape. The reaction kinetics of the soluble minerals governs the dissolution process and therewith the increase of the conduit diameter. The descriptions in this section follows mainly the structure of Kaufmann (2009) and is given here for a consistent overview of the theoretical principles behind the modelling studies presented in this work.

### 2.1.1 Geometry of a single conduit

The use of circular conduits for modelling the evolution of karst aquifers follows from the idealized concept that the most probable flow paths inside a karst aquifer are along the junctions of small fissures and bedding planes (see Fig.2.1). These

conduits are used to simulate the flow trough the aquifer and can be described by their diameter $d$ [m] and their length $l$ [m]. The cross-sectional area of the conduit is $A = \pi d^2/4$ [m$^2$].

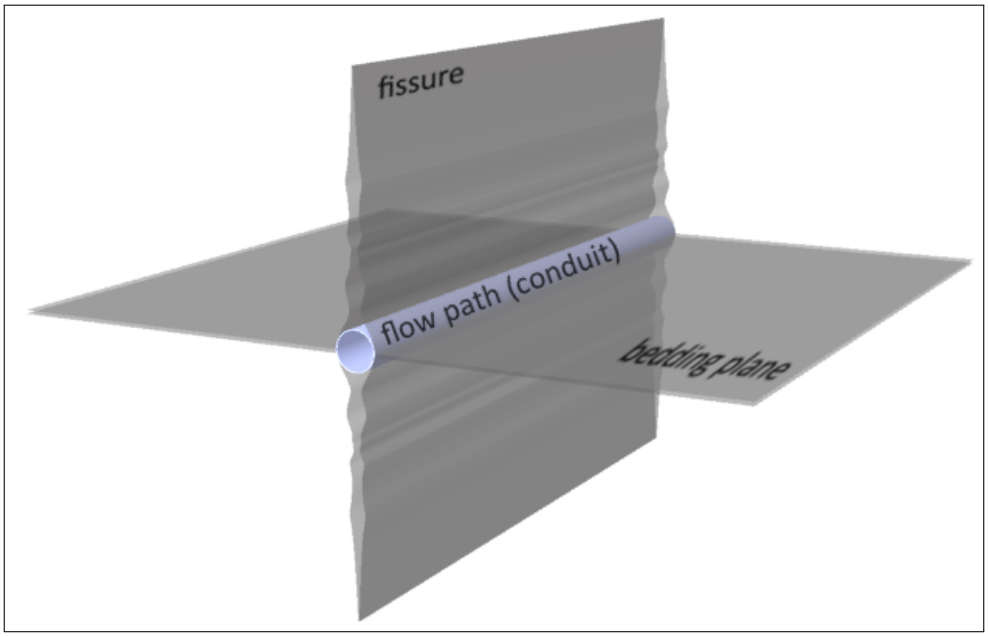


**Fig. 2.1:** Geometrical model of a 1D conduit; The flow path along a junction between a fissure and a bedding plane can be described by a circular conduit. Modified after Kaufmann (2009).

### 2.1.2 Flow in a single conduit

Flow $Q$ [m$^3$ s$^{-1}$] through the conduit is modelled as fully developed, incompressible Poiseuille flow with no buoyancy forces. It is driven by the hydraulic pressure difference between entrance and exit $\Delta p$ and the coefficient $K'$. Generally $\Delta p$ is expressed as head loss and is given by

$$\Delta h = \frac{\Delta p}{\rho g} + \Delta z, \tag{2.1}$$

with $\rho$ [kg m$^{-3}$] the density of water, $g$ [m s$^{-2}$] the gravitational acceleration and $\Delta z$ [m] the height difference between entrance and exit of the conduit. Flow and head loss are then related by the power–law equation (Kaufmann, 2009)

$$Q^n = K'\Delta h. \tag{2.2}$$

where $K'$ holds the properties of the conduit geometry and the flow (conductivity). Although for laminar flow the units of $K'$ in eq. 2.2 are $[\mathrm{m}^2\,\mathrm{s}^{-1}]$ which corresponds to a viscosity one may also find in literature the term hydraulic resistance $R\,[\mathrm{m}^{-2}\,\mathrm{s}]$ which is the reciprocal of $K'$.

**Laminar flow** First laminar flow is assumed. For laminar flow $n = 1$ in eq. 2.2 and $K'$ is derived by the Hagen-Poiseuille law (e.g. Beek and Muttzall (1975))

$$K'_l = \frac{gd^4}{40\nu l} \tag{2.3}$$

with $\nu\,[\mathrm{m}^2\,\mathrm{s}^{-1}]$ the kinematic viscosity of water. Because of $u = K\nabla h$ the hydraulic conductivity $K_c^l\,[\mathrm{m\,s}^{-1}]$ of a conduit is given by

$$K_c^l = \frac{gd^2}{32\nu}. \tag{2.4}$$

**Turbulent flow** For turbulent flow $n = 2$ in eq. 2.2 and the non-linear Darcy-Weissbach law is applied to derive $K'$

$$K'_t = \frac{\pi^2 g d^5}{8fl}. \tag{2.5}$$

The hydraulic conductivity $K_c^t$ of a conduit is then given by

$$K_c^t = \frac{2gd}{f}. \tag{2.6}$$

Because the flow trough a conduit can either be laminar or turbulent the Reynolds number $Re$ is used to distinguish between both cases. The Reynolds number is given by

$$Re = \frac{ud}{\eta}, \tag{2.7}$$

with $u = Q/A\,[\mathrm{m\,s}^{-1}]$ the Darcy-flow velocity, the conduit diameter $d$ and the dynamic viscosity $\eta\,[\mathrm{kg\,m}^{-1}\,\mathrm{s}^{-1}]$. Generally a critical Reynolds number of $Re_c = 2200$ is used, where values smaller than $Re_c$ assign a laminar flow rate and values

larger than $Re_c = 2200$ a turbulent flow rate respectively. It is important to note that the Reynolds number $Re$ in eq. 2.7 depends on the flow rate $Q$. Therefore, first a laminar flow rate is assumed for deriving $Re$. If $Re < Re_c$ then the flow is laminar and the laminar friction factor is given by

$$f_l = \frac{64}{Re}. \tag{2.8}$$

If $Re > Re_c$ the flow is turbulent and has to be recalculated with a turbulent friction factor $f$. It is derived by the maximum of

$$\begin{aligned} f_s &= 0.3164\, Re^{-0.25}, \\ f_t^{-0.5} &= 1.14 - 2log(\frac{w}{d} + \frac{9.35}{Re} f_t^{-0.5}), \\ f_r^{-0.5} &= 1.14 - log(\frac{w}{d}), \end{aligned} \tag{2.9}$$

where $f_s$ is smooth turbulence, $f_t$ is the transition between smooth and rough turbulence, $f_r$ is rough turbulence and $w\,[\mathrm{m}]$ is the wall roughness. Note that for the transitional regime $f_t$ needs to be derived iteratively (Colebrook-White equation) whereas for the rough regime $f_r$ becomes independent from $Re$.

Generally, if flow through a given conduit is turbulent, the flow rate is smaller than the corresponding laminar flow rate (see 2.1.4). So if for larger conduits turbulence is not considered, the flow rates are generally overestimated.

### 2.1.3 Reaction kinetics

Before modelling the evolution of a single conduit the reaction kinetics within a karst aquifer have to be known. The chemical part in the removal of karst bedrock is governed by the dissolution rate or flux rate F $[\mathrm{mol\,m^{-2}\,s^{-1}}]$.

The flux rate F as a function of calcium concentration describes the removal of bedrock per unit area and time and has been intensively studied by Buhmann and Dreybrodt (1985a,b); Dreybrodt (1988); Eisenlohr et al. (1999); Kaufmann and Dreybrodt (2007); Plummer et al. (1978); Svensson and Dreybrodt (1992). It can be described by

$$\mathrm{F} = k_i \left( m_i - \frac{c}{c_{eq}} \right)^{n_i}, \quad i = 0, n \quad , \tag{2.10}$$

with $k_i\,[\mathrm{mol\,m^{-2}\,s^{-1}}]$ a rate coefficient, $c\,[\mathrm{mol\,m^{-3}}]$ the actual concentration of

$Ca^{2+}$ in the water and $c_{eq}$ [mol m$^{-3}$] the equilibrium concentration with respect to the soluble mineral. Furthermore, there are two dimensionless parameters, the coefficient $m_i$ [−] and the power-law exponent $n_i$ [−]. The calcium equilibrium concentration $c_{eq}$ as a function of carbon–dioxide partial pressure $pCO_2$ and temperature $T$ is given for the open system after Dreybrodt (1988) by

$$c_{eq}^3 = \frac{K_1 K_C K_H}{4 K_2 \gamma_{Ca^{2+}} \gamma_{HCO_3^-}^2} pCO_2, \tag{2.11}$$

with the equilibrium constants $K_1$, $K_2$, $K_C$ and $K_H$ and the activity coefficients $\gamma_{Ca^{2+}}$ for calcium and $\gamma_{HCO_3^-}^2$ for bicarbonate, respectively. For the closed system $pCO_2$ is reduced according to Dreybrodt (1988) to

$$pCO_2 = p_i CO_2 \frac{c_{eq}}{K_H \left(1 + \frac{1}{K_0}\right)}, \tag{2.12}$$

with $p_i CO_2$ the initial carbon–dioxide partial pressure and the equilibrium constant $K_0$. The given equilibrium coefficients and activity coefficients are given in Tab. 2.1.

The coefficient $k_i$ and the exponent $n_i$ in eq. 2.10 are characteristic parameters for the bedrock mineral, and depend on the amount of undersaturation in the subsurface water. For the initial linear kinetics the parameters $k_0$, $m_0$ and $n_0$ have been derived by Kaufmann and Dreybrodt (2007) and are given in Tab. 2.1. For the low–order linear kinetics where $i = 1$ in eq. 2.10 the coefficients $k_1$, $m_1$ and $n_1$ are based on theoretical and experimental studies of Buhmann and Dreybrodt (1985a,b); Svensson and Dreybrodt (1992); Dreybrodt et al. (1996); Eisenlohr et al. (1999) and $k_1$ is given by

$$k1 = k_1^{'} \left(1 + \frac{k_1^{'} d(t)}{6 D c_{eq}}\right)^{-1} \tag{2.13}$$

with the rate coefficient $k_1^{'}$ and the diffusion coefficient $D$. For high–order kinetics a power law according to Palmer (1991); Eisenlohr et al. (1999) is used

$$k_2 = k_1 \left(1 - \frac{c_1}{c_{eq}}\right)^{n_1 - n_2}. \tag{2.14}$$

For a comprehensive summary on calcite dissolution kinetics the reader is referred

to Kaufmann and Dreybrodt (2007). For gypsum dissolution Jeschke et al. (2001) derived a similar rate law as shown in eq. 2.10. Details on the derivation of the equilibrium concentration $c_{eq}$ can be found, e.g. in Dreybrodt (1988). For calcite $c_{eq}$ is a function of temperature $T$ [°C] and carbon dioxide partial pressure $pCO_2$ [atm] (closed system conditions are assumed throughout this thesis). For gypsum $c_{eq}$ can assumed to be a constant value (see Tab. 2.1 for the reference parameters).

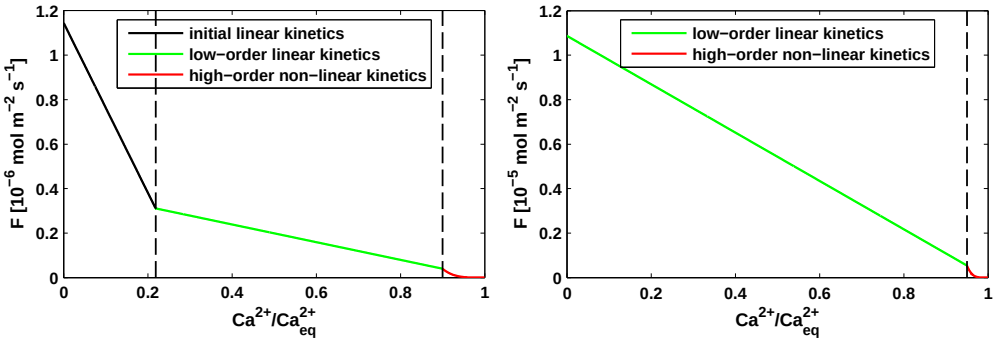


**a)** Flux rates $F$ for calcite $CaCO_3$ **b)** Flux rates $F$ for gypsum $CaSO_4$

**Fig. 2.2:** Flux rates $F$ for calcite (**a**) and gypsum (**b**); **a)** initial linear kinetics (black line) show fast drop in flux rates, low–order linear kinetics (green line) show slow drop in flux rates whereas with high–order non–linear kinetics (red line) rates drop with a power–law relation; $d = 0.1$ [mm], $Ca^{2+}_{eq} = 2.1$ [mol m$^{-3}$], $T = 10$ [°C], $pCO_2 = 0.05$ [atm]; **b)** low–order linear kinetics (green line) show a fast drop in flux rates until the switch to high–order non–linear kinetics (red line) where the rates drop with a power-law relation; $d = 0.1$ [mm], $Ca^{2+}_{eq} = 15.4$ [mol m$^{-3}$].

Fig. 2.2a shows the relation between calcium saturation $Ca^{2+}/Ca^{2+}_{eq}$ and flux rate $F$ for calcite. The values have been calculated for a conduit diameter of $d = 0.1$ [mm] and a calcium equilibrium concentration of $Ca^{2+}_{eq} = 2.1$ [mol m$^{-3}$] ($T = 10$ [°C], $pCO_2 = 0.05$ [atm]). For the initial linear kinetics at high undersaturation (black line) the rate drops very fast over almost on order of magnitude. For the slow low–order linear kinetics (green line) the rate also drops linearly but much slower than for the initial kinetics (eq. 2.13). If the calcium concentration increases above the switch concentration $c_s$ ($c_s = 0.9c_{eq}$ for calcite) the system exhibits higher–order kinetics (red line) where the rate becomes non–linear and the coefficients $m_2$, $k_2$, and $n_2$ are used (eq. 2.14).

A similar behaviour can be seen for gypsum flux rates in Fig. 2.2b. The conduit diameter is again $d = 0.1$ [mm] and the calcium equilibrium concentration is

$Ca^{2+}_{eq} = 15.4\,[\mathrm{mol\,m^{-3}}]$. For gypsum there is only one low–order linear regime (green line). Here the rate drops significantly over one order of magnitude until the switch concentration ($c_s = 0.95 c_{eq}$ for gypsum) is reached. Note that the flux rates for gypsum are one order of magnitude higher than for calcite.

The consequences from the flux rate law in eq. 2.10 are manifold and can be found in the aforementioned literature. They are only briefly summarized here. The rates for calcite depend not only on the diameter $d$ but also on temperature $T$ and carbon dioxide partial pressure $pCO_2$. For diameters below $d < 0.1$ [mm] the rates are controlled by the surface dissolution rates and the $CO_2$–conversion. For larger diameters the rate limiting effect of diffusion $D$ (eq. 2.13) becomes more important. Furthermore, the warmer the solution the less calcium can be dissolved whereas with increasing $pCO_2$ the dissolution rates increase (Kaufmann, 2009).

The linear kinetics are responsible for high dissolution rates close to the entrance of the conduit where the solution is strongly undersaturated with respect to calcite / gypsum. With increasing saturation the non–linear part becomes significantly important for the evolution of pre–mature karst aquifers. The reduced rates allow for a solution close to equilibrium to penetrate deep into the aquifer and maintain the dissolution process (Gabrovšek, 2000).

### 2.1.4 Dissolutional widening

With the formulations in 2.1.2 and 2.1.3 the evolution of a single conduit can be simulated by numerical means. Several authors have studied the evolution of single fractures or conduits. For a comprehensive summary on karst evolution modelling see the references given in 1.1 or e.g. Dreybrodt et al. (2005) and the references therein.

The increase of the conduit diameter $d$ can be derived from

$$d(t_i) = d(t_{i-1}) + \mathrm{F}\frac{M_{MIN}}{\rho_{MIN}}(t_i - t_{i-1}). \tag{2.15}$$

Here $t_{i-1}$ and $t_i$ are two consecutive time steps, F is the flux rate as described in 2.1.3, $M_{MIN}$ [kg mol$^{-1}$] is the molar mass and $\rho_{MIN}$ [kg m$^{-3}$] the density of the soluble mineral (calcite or gypsum), respectively. For each time step the conduit is subdivided into smaller portions $\Delta l_j$ as described in Groves and Howard (1994a). For each of these portions the calcium concentration, the wall retreat (removal of

dissolved calcium) and the new radius $\Delta r_j$ is calculated following the procedure given in Kaufmann and Braun (1999). The new effective conduit diameter $d_e$ after this process is given according to Groves and Howard (1994a)

$$d_e^4 = \frac{l}{\sum_{j=1}^{n} \frac{\Delta l_j}{(2\Delta r_j)^4}}. \tag{2.16}$$

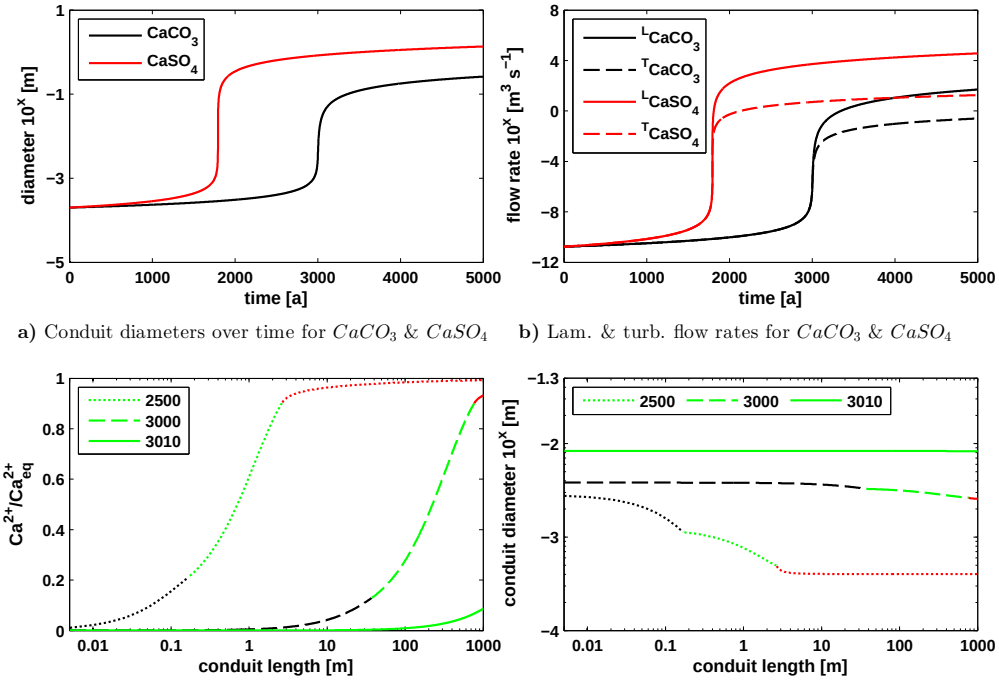


**a)** Conduit diameters over time for $CaCO_3$ & $CaSO_4$ **b)** Lam. & turb. flow rates for $CaCO_3$ & $CaSO_4$

**c)** Calcium saturation during evolution for $CaCO_3$ **d)** Conduit diameters during evolution for $CaCO_3$

**Fig. 2.3:** Single conduit evolution; see sub–captions for description; the colors in **c** and **d** are according to Fig. 2.2a and mark the different kinetics regimes for the three different time steps.

Fig. 2.3 shows the evolution of a single conduit for calcite and gypsum respectively. The initial diameter of each conduit is $d_0 = 0.2\,[\text{mm}]$, its length is $l = 1000\,[\text{m}]$ and the head difference between entrance and exit is $\Delta h = 50$ [m]. In Fig. 2.3a the increase of the conduit diameter $d$ over time is shown. The black curve represents the calcite conduit the red curve the gypsum conduit respectively. Both conduits show only little growth for the first 1000 years. A significant increase is visible for the gypsum conduit at $\approx$ 1800 years. Here the diameter increases rapidly over almost

four orders of magnitude. A similar behaviour can be seen for the calcite conduit later in time. Here the rapid increase of the diameter happens at $\approx 3000$ years and is a little less then three orders of magnitude. After this *jump* the diameters of both conduit grow constantly on a slower pace. An identical behaviour can be seen in Fig. 2.3b where the evolution of flow rates are shown. Black curves represent again the calcite conduit and red curves the gypsum conduit respectively. Like for the diameters in Fig. 2.3a also the flow rates show this significant *jump* over several orders of magnitude. Note that the solid lines represent flow rates if only laminar flow is considered. For the dashed lines turbulent flow is activated if the Reynolds number is above the critical threshold $Re > Re_c$. From Fig. 2.3b can be seen that turbulent flow decreases the flow rate in a conduit (see 2.1.2).

The short time interval when the strong increase of diameter and therewith also a strong increase of flow rates occur is called breakthrough time $T_B$ and was introduced by Dreybrodt (1996). The breakthrough time is a characteristic parameter for the growth of a single conduit and is given by

$$T_B = 1.77 \times 10^{-8} \, (d)^{-3} \, (l)^{\frac{8}{3}} \, (\Delta h)^{-\frac{4}{3}} \, (c_{eq})^{-\frac{4}{3}} \, (k_1)^{\frac{1}{3}}. \tag{2.17}$$

It depends on the geometry of the conduit ($d$,$l$), the chemical parameters of the reaction kinetics ($c_{eq}$,$k_1$) and the head difference $\Delta h$. The breakthrough time also marks the transition between non–linear and linear kinetics inside the conduit (see 2.1.3). This is exemplarily shown for the calcite conduit in Fig. 2.3c+d. In Fig. 2.3c the calcium saturation for three snapshots in time along the conduit is shown. Fig. 2.3d shows the corresponding diameter along the conduit. The dotted line represents the conduit at the year 2500. The colors correspond to the color scale in Fig. 2.2a and mark the kinetics regime. Black color represents the initial linear kinetics, green the low–order linear kinetics and red the high–order non–linear kinetics respectively. For the conduit at 2500 years both linear regimes are only active up to the first meter (note that the x–axis is in log–scale). In the remaining part of the conduit the non–linear kinetics are active and allow for small dissolution rates and little diameter growth. Note the funnel shape of the conduit diameter in Fig. 2.3d. The new effective diameter after the dissolution process for this time step is calculated with eq. 2.16. Shortly before breakthrough, at 3000 years (dashed line), the linear kinetics are active almost along the entire conduit. Here the dissolution rates are moderate and the funnel shape of the conduit is not that pronounced anymore. Right after

the breakthrough occurs at 3010 years (solid line) the low–order linear kinetics are active along the entire conduit. A lot of calcium is dissolved at high rates as the solution is highly undersaturated along the whole conduit and the diameter grows almost linearly at a constant pace. A similar behaviour can be observed for a conduit under gypsum dissolution kinetics. The only differences are the missing initial fast linear kinetics and the about one order of magnitude higher dissolution rates (see 2.1.3 and Fig. 2.2).

## 2.2 Modelling a 3D domain

The program KARSTAQUIFER, used in this work, is a development of the research group of Prof. Kaufmann from the Free University of Berlin. It applies the concept of a discrete fracture approach as described by e.g. Huyakorn et al. (1983); Kaufmann and Braun (2000). Therefore, the fractures / conduits are directly incorporated into the modelling domain which allows for a consistent modelling of flow inside the aquifer. The program has been so far applied to study different karst evolution scenarios presented in Kaufmann (2009); Kaufmann et al. (2010).

The flow of water through a fissured and fractured aquifer can be described by a transient continuity equation

$$\frac{\partial}{\partial x}\left(K(t)\frac{\partial h}{\partial x}\right)+\frac{\partial}{\partial y}\left(K(t)\frac{\partial h}{\partial y}\right)+\frac{\partial}{\partial z}\left(K(t)\frac{\partial h}{\partial z}\right)=S\frac{\partial h}{\partial t}, \tag{2.18}$$

where, $K(t)$ [m s$^{-1}$] is the time–dependent hydraulic conductivity, $S$ [m$^{-1}$] the specific storage and $h$ [m] the hydraulic head. Furthermore, $x$ [m], $y$ [m] and $z$ [m] denote the spatial coordinates, and $t$ [s] is time. In a three–dimensional domain eq. 2.18 gives a set of $N$ equations corresponding to $N$ nodes that needs to be solved for the unknown heads $h_{1,N}$. Therefore, the finite element method is applied with three–dimensional parallelepipedal elements that represent the rock matrix and two–dimensional bar elements that represent the conduit network respectively. Fig. 2.4 shows a idealized model of one matrix element. There, the conduits around the matrix element $E_1$ are defined along the edges of the element between the nodes $N_{1,8}$. The system of $N$ equations to calculate the heads is solved by a finite–element method as described e.g. in Istok (1989). The flow through the domain changes over times because the hydraulic conductivity of the domain changes. In eq. 2.18 $K(t)$ consists of

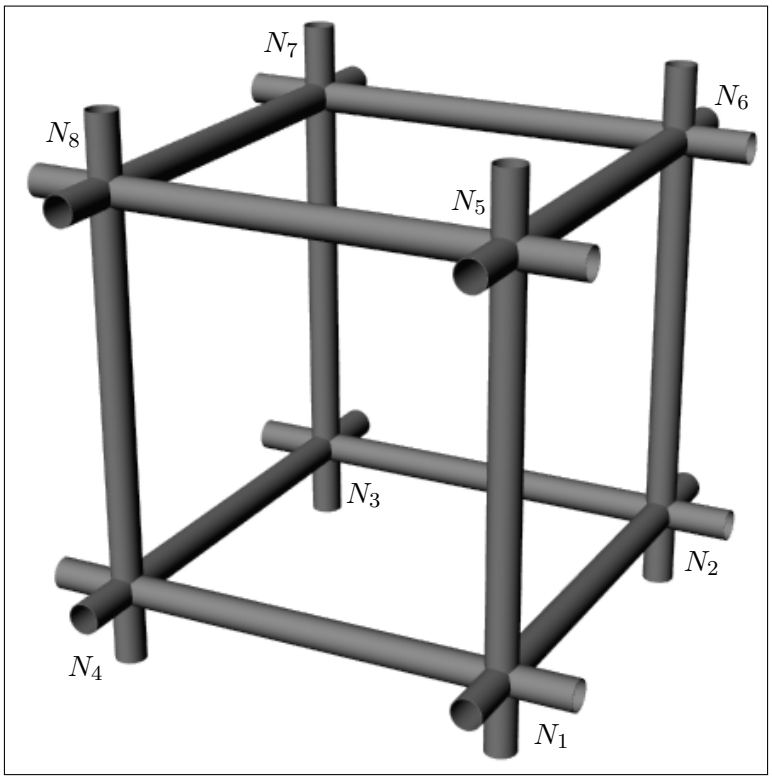


**Fig. 2.4:** Idealized geometrical model of an element inside the 3D domain; the element is created by 8 grid nodes and represents the rock matrix, the edges of the element (the connection between the nodes) represent the conduit network respectively.

$$K(t) = K_m + K_c(t), \tag{2.19}$$

where $K_m$ is the invariant hydraulic conductivity of the matrix and $K_c(t)$ the hydraulic conductivity of the conduits, respectively. $K_m$ is fixed to a constant value throughout the entire numerical simulation. From eqs. 2.4 and 2.6 follows, that the hydraulic conductivity of the conduits $K_c(t)$ changes over time due to their dissolutional widening. The general procedure when modelling the evolution of a three–dimensional karst aquifer is described below.

1. Assembling of the finite element grid with the 3D and 2D elements
2. Applying initial parameters to the elements ($K_m$,$d_0$,$c_0$ etc.)

3. Applying the boundary conditions (constant head, fixed flow, recharge, etc.)
4. Solving the system of equations to get the hydraulic heads $h$ at all nodes $N$ (when turbulence is active an iterative approach is used)
5. Sort the nodes according to the calculated hydraulic heads in descending order
6. Calculate the flow rate through each conduit (laminar or turbulent) and apply the corresponding flux rate law
7. Calculate the wall retreat, the new effective diameter $d_e$ and the calcium concentration $c$ for all conduits
8. Update $K_c(t)$ and start from 3. until the end of the model run

These are the basic steps when modelling karst evolution in three dimensions. For complex model setups it is possible to assign every element and every conduit different initial parameters. The model can either consist of a homogeneous / uniform initial conduit diameter network or a statistical one. If the latter is applied the initial conduit diameter distribution is created with a log–normal distribution with a mode of $\hat{d}_{ln}$ and a standard deviation $\sigma_n$ for the corresponding normal distribution. First, the mean of the normal distribution is calculated by

$$\mu_n = \ln(\hat{d}_{ln}) + \sigma_n^2. \tag{2.20}$$

Then the normal distribution is given by

$$\mathrm{N}_n(\mu_n, \sigma_n^2) = \mu_n + \sigma_n D_n, \tag{2.21}$$

where $D_n$ $[0, 1]$ is a standard normal distribution. The log–normal distribution finally is

$$\mathrm{N}_{ln} = exp(\mathrm{N}_n). \tag{2.22}$$

As an example two log–normal distributions are shown in Fig. 2.5. The black curve has parameters $\hat{d}_{ln} = 0.1$ [mm] and $\sigma_n = 0.5$ whereas the red curve has parameters $\hat{d}_{ln} = 0.3$ [mm] and $\sigma_n = 1$ respectively. The influence of the statistical conduit network parameters on the evolution of a three–dimensional karst aquifer has been shown by Kaufmann et al. (2010). The wider the distribution the more

enlarged conduits are initially present to create a preferential flow path. In this way a wide distribution acts similar to a model setup that has been used e.g. by Gabrovšek and Dreybrodt (2001); Gabrovšek et al. (2004). There, a secondary percolation network of larger fractures is superimposed on a finer network of small fissures.

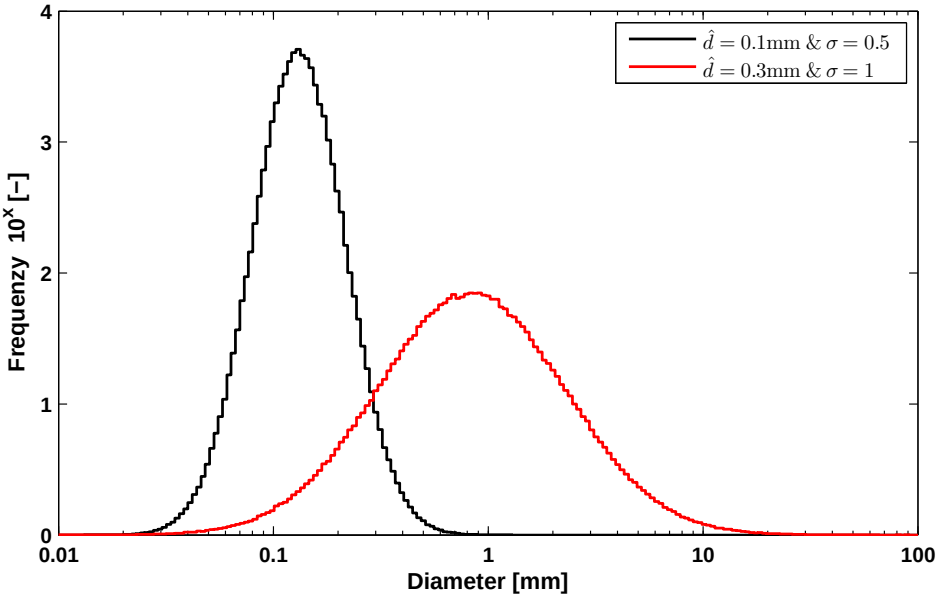


**Fig. 2.5:** Two log-normal distributions with different statistical parameters

This chapter has presented the theoretical principles and modelling basics that are the theoretical framework of this thesis. To give an in–depth analysis of the individual parts would be way beyond the scope of this work. The interested reader is therefore referred to the given references.

| **Parameters** | **Symbol** | **Unit** | **Value(s)** |
|---|---|---|---|
| *Gypsum chemistry:* | | | |
| Molar mass | $M$ | $\mathrm{kg\,mol^{-1}}$ | 0.1722 |
| Density | $\rho$ | $\mathrm{kg\,m^{-3}}$ | 2320 |
| Linear kinetic exponent | $n_1$ | | 1 |
| High-order kinetic exponent | $n_2$ | | 4.5 |
| Linear rate constant | $k_1$ | $\mathrm{mol\,m^{-2}\,s^{-1}}$ | $1.1 \times 10^{-5}$ |
| Calcium concentration | c | $\mathrm{mol\,m^{-3}}$ | $c_{in} < c < c_{eq}$ |
| Calcium equilibrium concentration | $c_{eq}$ | $\mathrm{mol\,m^{-3}}$ | 15.4 |
| Initial calcium concentration | $c_{in}$ | $\mathrm{mol\,m^{-3}}$ | 0 |
| Calcium switch concentration | $c_s$ | $\mathrm{mol\,m^{-3}}$ | $0.95c_{eq}$ |
| | | | |
| *Limestone chemistry:* | | | |
| Molar mass | $M$ | $\mathrm{kg\,mol^{-1}}$ | 0.1001 |
| Density | $\rho$ | $\mathrm{kg\,m^{-3}}$ | 2700 |
| Linear kinetic exponents | $n_0 = n_1$ | | 1 |
| High-order kinetic exponent | $n_2$ | | 4 |
| Intercept constant | $m_0$ | | 0.3 |
| Intercept constants | $m_1 = m_2$ | | 1 |
| Initial rate constant | $k_0$ | $\mathrm{mol\,m^{-2}\,s^{-1}}$ | $4 \times 10^{-6}$ |
| Linear rate constant | $k_1^{'}$ | $\mathrm{mol\,m^{-2}\,s^{-1}}$ | $4 \times 10^{-7}$ |
| Diffusion coefficient | $D$ | $\mathrm{m^2\,s^{-1}}$ | $10^{-9}$ |
| Calcium concentration | c | $\mathrm{mol\,m^{-3}}$ | $c_{in} < c < c_{eq}$ |
| Initial calcium concentration | $c_{in}$ | $\mathrm{mol\,m^{-3}}$ | 0 |
| Calcium switch concentration | $c_s$ | $\mathrm{mol\,m^{-3}}$ | $0.9c_{eq}$ |
| Temperature | $T$ | °C | 10 |
| Partial pressure of carbon dioxide | $pCO_2$ | atm | 0.05 |
| | | | |
| Ion activity | $I$ | $\mathrm{mol\,l^{-1}}$ | 3c |
| Debye–Hückel coefficient | $A$ | | $0.4883 + 8.074 \times 10^{-4}T$ |
| Debye–Hückel coefficient | $B$ | | $0.3241 + 1.600 \times 10^{-4}T$ |
| Activity coefficient | $log\,\gamma_{Ca^{2+}}$ | | $\frac{-4A\sqrt{I}}{1+5.0B\sqrt{I}}$ |
| Activity coefficient | $log\,\gamma_{HCO_3^-}$ | | $\frac{-1A\sqrt{I}}{1+5.4B\sqrt{I}}$ |
| Equilibrium constant | $log\,K_0$ | | $K_5/K_1$ |
| Equilibrium constant | $log\,K_1$ | $\mathrm{mol\,l^{-1}}$ | $-356.3094 - 0.06091964T + 21834.37/T + 126.8339\,log\,T - 1684915/T$ |
| Equilibrium constant | $log\,K_2$ | $\mathrm{mol\,l^{-1}}$ | $-107.8871 - 0.03252849T + 5151.79/T + 38.92561\,logT - 563713.9/T$ |
| Equilibrium constant | $log\,K_5$ | $\mathrm{mol\,l^{-1}}$ | $1.707 \times 10^{-4}$ |
| Equilibrium constant | $log\,K_C$ | $\mathrm{mol^2\,l^{-2}}$ | $-171.9065 - 0.077993T + 2839.319/T + 71.595\,log\,T$ |
| Equilibrium constant | $log\,K_H$ | $\mathrm{mol\,l^{-1}\,atm^{-1}}$ | $108.3865 + 0.01985076T - 6919.53/T - 40.45154\,logT + 669365/T$ |

**Table 2.1:** Dissolution kinetics parameters for gypsum and limestone used in this work.

# Chapter 3

# The development of 3D karst evolution dam–site models

Often, large water reservoirs and dam–sites are built in karst areas to provide people with drinking water, water for agriculture and / or to produce hydroelectric power. While natural karstification normally proceeds on time scales of several 100 000 years, close to dam–sites or other man–made structures this can change considerably. The water that is impounded by the reservoir increases the hydraulic gradients and thereby the local hydraulic boundary conditions significantly. Sometimes, depending on the size of the dam–site and the local geology, this change can be by several orders of magnitude compared to the natural pre–dam situation. Then, this high hydraulic gradients accelerate the karstification considerably, thus reducing the time scales of enlargement of fractures and fissures to only $10 - 100$ years.

The impounded water poses several threats to the structure of the dam–site:

1. sediment–filled channels can be opened and result in increased leakage of the reservoir,

2. small fissures are rapidly enlarged by dissolution and can bypass the dam structure through the reservoir bottom or the valley flanks to provide alternative flow paths,

3. enlarged voids underneath or aside of the dam can become structurally weak enough to result in collapses, possibly damaging the dam structure itself.

These processes not only put the economic functionality of the dam–site at risk due to the critical leakage, they also increase the threat of a structural failure of the dam–site. Examples of catastrophic failures can be found throughout the literature, see e.g. Milanović (2000, 2004) for a comprehensive summary. DeWaele (2008); Johnson (2008); Malkawi and Al-Sheriadeh (2000); Unal et al. (2007) give examples on the problems arising from increased leakage around dam–sites.

Because of the high risks accompanied by dam–sites in karst regions, numerous scientifical and technological efforts are needed to investigate areas of interest, preferably before the dam is build. This pre–construction phase should contain e.g. geological, hydrological, geophysical and geotechnical observations. Of course the aforementioned tasks are not limited to the pre–construction phase and are generally also considered during the lifetime of a dam. If a mature karst system is already present, intensive technical measures, often associated with high costs, have to be

carried out to stabilize and support the dam–site and its surroundings (Malkawi and Al-Sheriadeh, 2000; Karimi et al., 2007; Mohammadi and Raeisi, 2007; Unal et al., 2007). Here, the most common leakage prevention technique is the construction of a grout curtain around the dam to seal the surrounding bedrock. Unfortunately, the construction of grout curtains poses new threats to the sensitive karst environment. Examples for the ecological and environmental impact of grouting measures especially in the Dinaric karst region are given e.g. by Bonacci et al. (2009); Bonacci and Josip (2009). The authors state that even when a lot of grouting has been done, it is not guaranteed that the reservoir is sealed. Furthermore, the grouting material itself can have a long lasting negative effect on the sensitive ecosystem that is found in karst regions.

Understanding the complex interrelations and interactions of hydrogeological processes in karst areas, was and still is a challenging task for the science community. The objective of the next two chapters is to show the advantages of the ability to simulate the evolution of complex karst aquifer systems close to dam–sites. As an entry point, this chapter presents the development of simple 3D dam–site models. After the conceptual model setup is explained, pseudo–3D models are used to test the 3D program against earlier 2D dam–site models. Then, the evolution of a 3D dam–site model is shown and a sensitivity analysis is carried out to estimate the dependency of the breakthrough time $T_B$ on the model parameters. Finally, the model complexity is increased by using a non–uniform (statistical) conduit network and topography.

The essential results of this chapter have been presented in Hiller et al. (2011). The figures here are redrawn to comply with the color scale layout of this work.

## 3.1 The model setup

### 3.1.1 Conceptual model

The simplified dam–site models used in this work are based on the conceptual model shown in Fig. 3.1. The basic setting consists of a dam–site **A** that impounds a reservoir **D** in a narrow valley. The bedrock **F** in the valley flanks and below the reservoir is assumed to be a karst bedrock such as limestone or gypsum. This bedrock is already interspersed by a fine network of fissures and voids. The river **E** that was blocked by the dam continues on the bottom of the downstream part. Especially

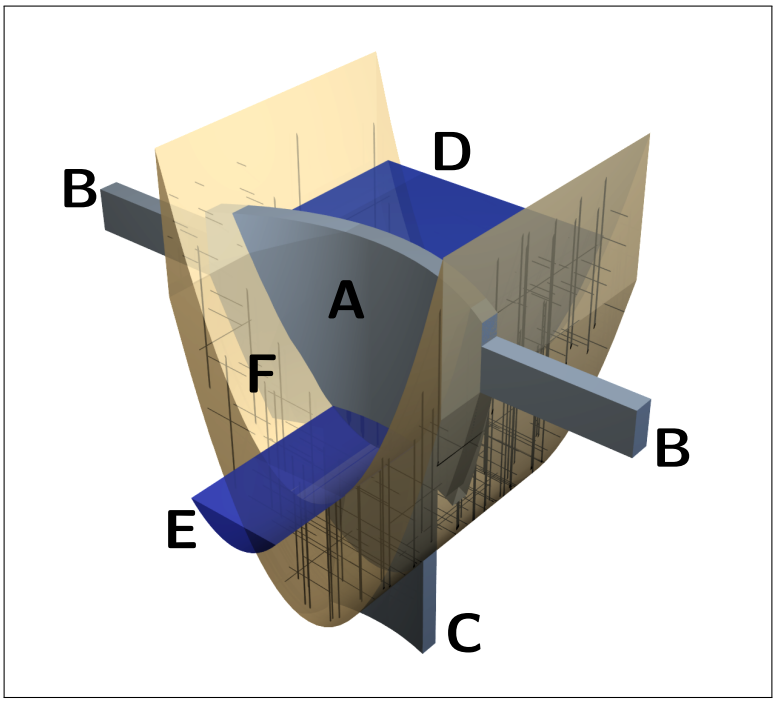


**Fig. 3.1:** Conceptual model of a 3D dam-site; **A** dam wall; **B** horizontal grout curtains; **C** vertical grout curtain; **D** reservoir; **E** river; **F** karst bedrock.

when built in a karst region, it is sometimes necessary to extent a dam horizontally and vertically by so called grout curtains (**B** and **C**) into the bedrock. This is done to prevent water to flow from the reservoir through the network of fissures or a preexisting fault system into deeper parts of the bedrock and consequently around the dam. If such flow paths are established, leakage rates can increase dramatically and engineering measures need to be carried out to ensure the structural safety of the dam–site.

Based on the conceptual model in Fig. 3.1 a 3D model domain was created to simulate the karstification process around a dam–site. The model domain as shown in Fig. 3.2 consists of limestone bedrock and is discretized by parallelepipedal finite elements. The dam–site itself is assumed impermeable and is characterized by its width $W$ (the width across the river channel), length $L$ (the length along the river channel) and height $H$. As it will be shown later the dam height $H$ also corresponds to the reservoir depth $H$. For simplicity the dam is of rectangular shape. The dam width $W$ accounts for the horizontal grout curtains and the dam length $L$

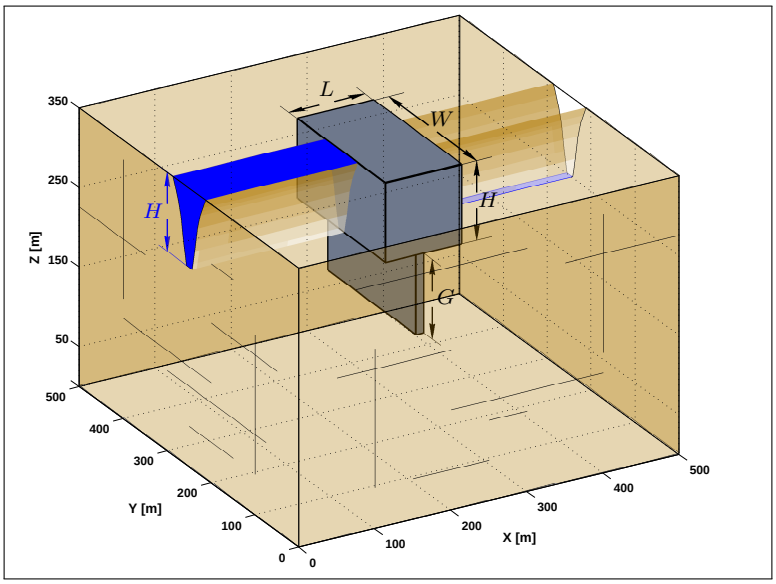


**Fig. 3.2:** Model domain developed on the basis of the conceptual model shown in Fig. 3.1; $W$ dam width; $L$ dam length; $G$ grout depth; $H$ reservoir depth / dam height.

for a sealing apron at the valley bottom respectively. The vertical grout curtain is implemented by an impermeable wall centered below the dam-site with a certain extent in depth $G$. If not stated differently the grout curtain has the same width as the dam–site. The standard domain parameters can be found in Tab. 3.1. The largest model used in this chapter has an extent of 500 m × 500 m × 350 m and a grid resolution of $dx = dy = dz = 6.25$ m. This gives a total of 373,977 grid nodes, 358,400 matrix elements and 1,093,176 conduit elements.

The chemical parameters for the limestone dissolution are according to Tab. 2.1. For the sensitivity analysis in 3.2.2 geometrical and chemical parameters may vary, but this will be stated there.

### 3.1.2 From 2D to 3D – the pseudo–3D model

Before starting with a real 3D model the results of earlier 2D dam–site models shall be reproduced with KARSTAQUIFER. This is done to test the 3D implementation of the program. For this evaluation, models generated with the 2D code shown in e.g. Kaufmann and Braun (1999, 2000); Kaufmann (2003c); Kaufmann and Romanov (2008) are used.

| Parameters | Symbol | Unit | Value(s) |
|---|---|---|---|
| *Model domain:* | | | |
| Length | X | m | 500 |
| Width | Y | m | 500 |
| Height | Z | m | $250, 350$ |
| Discretization | dx, dy, dz | m | $6.25, 12.5$ |
| Matrix conductivity | $K_m$ | $\mathrm{m\,s^{-1}}$ | $1 \times 10^{-6}$ |
| Matrix specific storage | $S_m$ | $\mathrm{m^{-1}}$ | $1 \times 10^{-5}$ |
| Initial conduit diameter | $d_0$ | m | $3 \times 10^{-4}$ |
| | | | |
| *Dam-site:* | | | |
| Length | $L$ | m | $25 - 175$ |
| Width | $W$ | m | $25 - 500$ |
| Grout depth | $G$ | m | $37.5 - 150$ |
| Reservoir depth – hydraulic head | $H$,$\Delta H$ | m | $25 - 250$ |
| Matrix and conduit conductivity | $K_m, K_c$ | $\mathrm{m\,s^{-1}}$ | $1 \times 10^{-15}$ |

**Table 3.1:** Standard domain parameters for the 3D dam–site models.

To compare a 2D program with 3D program one needs to "blank out" the additional third dimension. This is generally achieved by so-called pseudo–3D models which are basically 2D models in a 3D domain. The implementation of such a pseudo–3D model is shown in Fig. 3.3. The difference to the conceptual model in 3.2 is obvious. The dam and the vertical grout curtain are extended across the whole domain in y–direction. This is also done for the reservoir (blue face) in the upstream part of the dam, where a constant head boundary condition $H = z_{max} + \Delta H$ is imposed. Consequently also the river or resurgence (red face) in the downstream part of the dam is extended across the whole domain. There, also a constant head boundary condition $H = z_{max}$ is imposed to achieve a head difference $\Delta H$ between the upstream and downstream part of the dam. All other domain boundaries are no flow boundaries.

Technically, there is now difference in whether to create a *thin* or *wide* pseudo–3D model. Every possible x–z–plane (as shown e.g. in Fig. 3.3b) taken along the y–direction could serve as a 2D model, as well as the whole block serves as a *wide* 2D model. The arrows in Fig. 3.3a+b indicate that for this comparison several different grout depths $G$ were simulated for the 2D model and the pseudo–3D model respectively.

Fig. 3.4 exemplary shows the evolution of one pseudo–3D model with a grout depth of $G = 50\,\mathrm{m}$. The dam length is $L = 100\,\mathrm{m}$ and the hydraulic head difference between upstream and downstream part is $\Delta H = 100\mathrm{m}$. The hydraulic conductivity

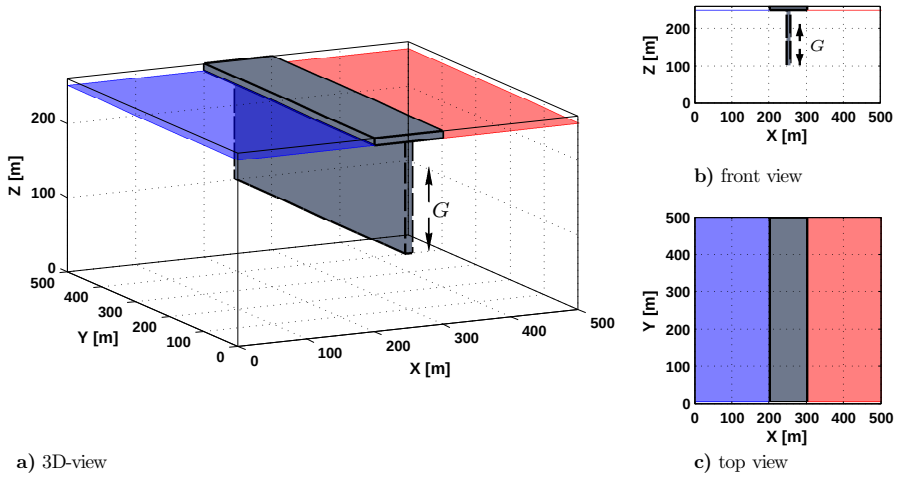


**Fig. 3.3:** Pseudo–3D dam–site model setup with varying grout depth $G$; blue face represents area of constant head BC with $H = z_{max} + \Delta H$ [m] (reservoir), red face represents area of constant head BC $H = z_{max}$ [m] (river / resurgence); **a)** 3D–view; **b)** front view; **c)** top view.

of each matrix element is $K_m = 1 \times 10^{-6}\,\mathrm{m\,s^{-1}}$ and in the uniform conduit network the initial diameter is $d_0 = 0.3\,\mathrm{mm}$. For all elements inside the dam $K_m$ and $d_0$ are several orders of magnitude smaller to achieve impermeability.

The four snapshots in time in Fig. 3.4 show the evolution of the karst aquifer beneath the dam–site. In Fig. 3.4a the initial situation is shown. for better visibility only the outlines of the dam are plotted. The grey faces are isosurfaces of constant head colored from light grey (low head) to dark grey (high head). Initially, they are radially aligned around the dam. Fig. 3.4b shows the evolution after 70 years shortly before breakthrough. The colored conduits correspond to an increase of the initial conduit diameter from a factor of 5 (blue) to a factor of $\geq 100$ (orange) respectively.

It can be seen that several competing horizontal pathways have developed from the vertical enlarged conduits close to the dam. Due to the high hydraulic gradients the upper of this horizontal paths is further enlarged while the lower ones are so far abandoned. The “winning” horizontal pathway develops close to the lower end of the grout curtain. The tips of the foremost conduits (blue color) of this horizontal path, follow the strong gradients and grow towards the downstream part of the dam. The increase of the gradient can also be seen by the shift of the isosurfaces of constant head from the upstream part to the downstream part of the dam (dark surfaces

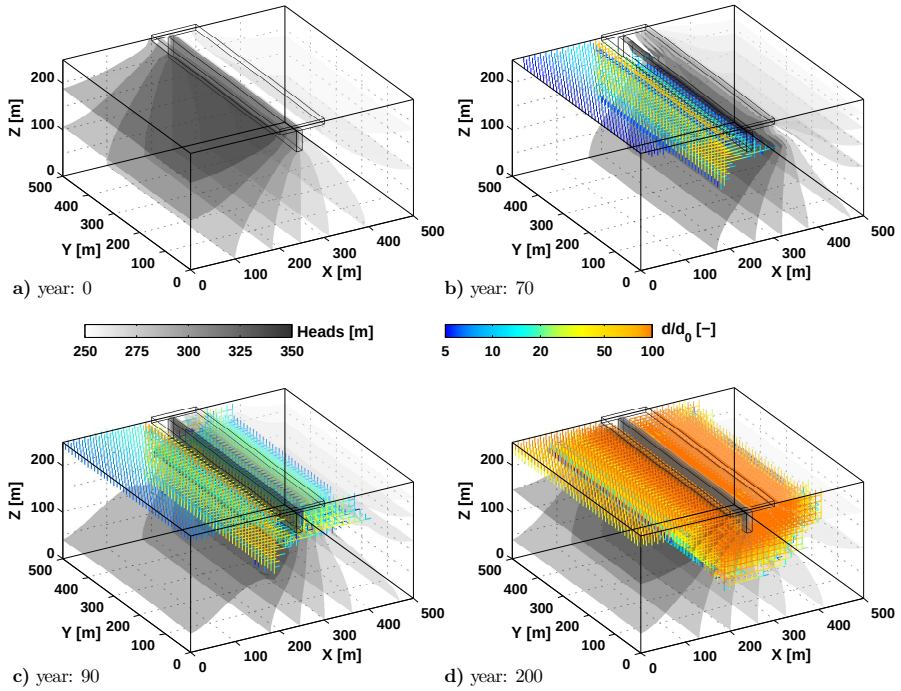


**Fig. 3.4:** Evolution of the pseudo–3D model; Plotted are the isosurfaces of constant head from 250 m (light grey) to 350 m (dark grey) values and the relative increase of the conduit diameter compared to the initial diameter on a log–scale from 5 (blue) to $\geq$ 100 (orange); **a)** initial situation – isosurfaces of constant head are radially spread around the dam; **b)** at t = 70 yr: conduits started to enlarge close to the dam–site and grow below the dam towards the downstream part; **c)** at t = 90 yr: conduits have reached the downstream part, flow is now turbulent in the connecting pathways; **d)** at t = 200 yr: evolved network of widened conduits, high flux rates and rapid enlargement of conduit diameters.

beneath the downstream apron of the dam). 20 years later (Fig. 3.4c) breakthrough has already occurred. The upstream part is connected to the downstream part by a continuous path of enlarged conduits (grown by a factor of $\approx$ 30). The isosurfaces of constant head started to *rebound* to their initial position. For simplicity it is assumed that the reservoir provides enough water to fulfill the constant head boundary condition. In reality however, at this point the leakage rates would be so high that the dam could no longer impound the reservoir. Because after the breakthrough the linear kinetics are established along the whole enlarged conduit pathway, large amounts of bedrock are removed at a constant pace. The situation after 200 years

is shown in Fig. 3.4d. The karstification has created a dense network of enlarged conduits around the dam–site with a growth factor of $\geq 100$. The head isosurfaces are now almost back in their initial position. If the calculation would not be stopped this process would continue until the whole bedrock is removed.

The fact that this pseudo–3D model behaves almost like a perfect 2D model can be seen in Fig. 3.4 by the symmetrical distribution of head isosurfaces and enlarged conduits around the dam-site for all snapshots in time. Only at the domain boundaries at $Y = 0$ m and $Y = 500$ m little deviations can be recognized which may be caused by numerical instabilities.

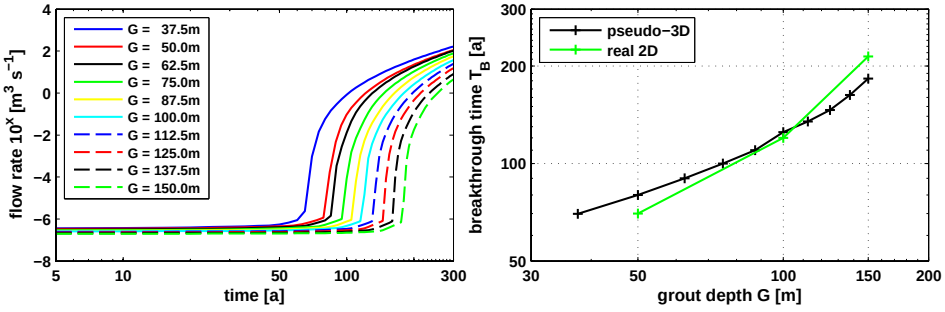


**a)** flow rates **b)** breakthrough time $T_B$

**Fig. 3.5:** **a)** flow curves for the pseudo–3D models with varying grout depths $G$ ($37.5 - 150$m) with typical breakthrough behaviour; **b)** breakthrough time $T_B$ as a function of grout depth for real 2D models (green curve) and pseudo–3D models (black curve).

This simulation is now repeated for different grout depths $G$. Fig. 3.5a shows the flow rates for the different pseudo–3D models with grout depths ranging from $G = 37.5$m to $G = 150$m. The flow rate is calculated by the amount of discharge through all resurgence nodes in the downstream part (red face in Fig.3.3). Like for the single conduit in 2.1.4 (Fig. 2.3b) the evolution of flow rates can be divided in three phases. In the initial phase the flow rates only slightly increase and stay almost at a constant base level. Then, depending on the grout depth $G$ and therewith the length of the breakthrough path, the flow rates start to increase rapidly over several orders of magnitude (breakthrough). Finally the increase in flow is again slowed down. In literature one may find different ways of determining the breakthrough time $T_B$, e.g. onset of turbulent flow inside the conduit or calculating the average head in the model domain for every time step and choosing the time where the

average head is maximum as breakthrough time (Kaufmann et al., 2010). All of these approaches have in common to exploit the typical shape of the flow curve with its rapid increase in rates. Therefore, the breakthrough time $T_B$ is determined here at the steepest point of the flow curve by using the first order derivative. In Fig. 3.5a can be seen that for a grout depth of $G = 37.5$m breakthrough occurs at $\approx 65$ years. If the grout depth is doubled to $G = 75$m (green solid line) breakthrough occurs at $\approx 100$ years and for the deepest grout ($G = 150$m, green dashed line) $T_B \approx 190$ years respectively.

Fig. 3.5b shows the breakthrough time as a function of grout depth for the real 2D models (green curve) and the pseudo–3D models (black curve) respectively. For the real 2D models only three different grout depths were available. Nevertheless, it can be seen that the results a comparable and the curves differ only between 2% and 15%. For a rough evaluation these results are sufficient enough. The 3D program produces generally the same results as the 2D program if the model setup is as close to 2D as possible. This was also shown by Kaufmann et al. (2010) where pseudo–3D models of a standardized *benchmark model* have been evaluated. It shows that the extension of the original program into the third dimension was successful and that KARSTAQUIFER can now be used for comprehensive 3D karst evolution modelling.

## 3.2 The 3D evolution models

### 3.2.1 The standard model

Now real 3D model setups are considered. Fig. 3.6 shows the standard dam–site layout which from now is referred to as the *standard model*. The standard model is a simplification of the model domain shown in Fig. 3.2 where the topography (valley) is cut off. This layout is simple enough to study the behaviour of a 3D dam–site model.

For the standard model the dam width $W$ and length $L$ as well as the grout depth $G$ are set to $W = L = G = 100$ m. As the topography is missing the dam is always located on top of the model domain at $Z = 250$ m. The model domain is represented by a grid of $41 \times 41 \times 21$ nodes to achieve a grid discretization of $dx = dy = dz = 12.5$m. This gives a total of 35301 nodes, 32000 matrix elements and 99 220 conduit elements respectively. The sealing apron of the dam is a $100 \times 100\,\mathrm{m}^2$ block in the center of the model domain (see Fig. 3.6c). Due to the discretization the

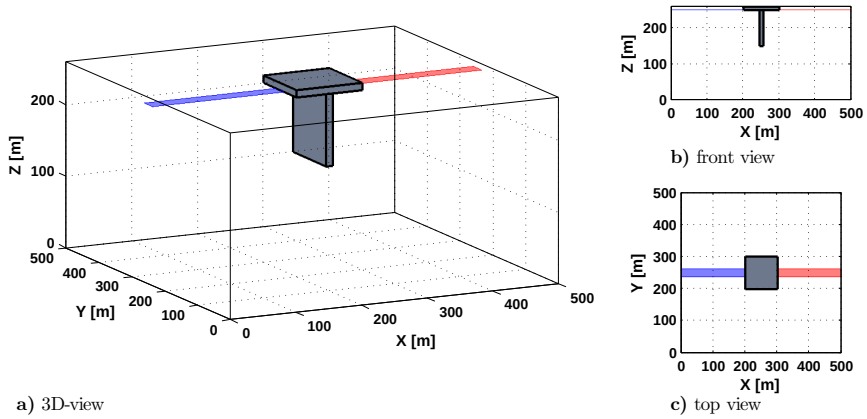


**a)** 3D-view **b)** front view **c)** top view

**Fig. 3.6:** Standard 3D dam–site model setup; blue face represents location of constant head BC with $H = z_{max} + \Delta H$ [m] (reservoir), red face represents location of constant head BC $H = z_{max}$ [m] (river / resurgence); **a)** 3D–view; **b)** front view; **c)** top view.

grout curtain is slightly shifted from the dam center to $X = [250\,\text{m}, 262.5\,\text{m}]$. The grout has the same width $W$[m] as the dam. The impounded reservoir extends from $X = 0\,\text{m}$ to the dam border and is two blocks (25 m) wide (Fig. 3.6 blue face). For the standard model the depth of the reservoir is 100 m which consequently yields a head difference to the downstream part of the dam of $\Delta H = 100\,\text{m}$. The resurgence area (river – red face in Fig. 3.6) has the same width as the reservoir, and extends from the dam border to $X = 500\,\text{m}$. The water in the reservoir is under saturated with respect to calcium ($c_{in} = 0\,\text{mol}\,\text{m}^{-3}$), its temperature is $T = 10\,^{\circ}\text{C}$, and it has a carbon–dioxide partial pressure of $pCO_2 = 0.01$ atm. All remaining domain boundaries are again no flow boundaries. The hydraulic conductivity of the matrix $K_m$ and the initial conduit diameter $d_0$ are again uniform throughout the entire model domain. For their values see Tab. 3.1.

Fig. 3.7 shows four snapshots in time in the evolution of the standard model. The initial situation is shown in Fig. 3.7a. For better visibility, only the outlines of the dam–site are plotted. From now on, when describing the model figures, we refer to the domain between $Y = 0\,\text{m}$ and $Y = 200\,\text{m}$ as right side of the dam–site and between $Y = 300\,\text{m}$ and $Y = 500\,\text{m}$ as left side of the dam–site respectively. Colors for the isosurfaces of constant head range from light grey (250 m) to dark grey (350 m). Like for the pseudo–3D models one can see that the hydraulic heads are initially radially aligned around the dam center.

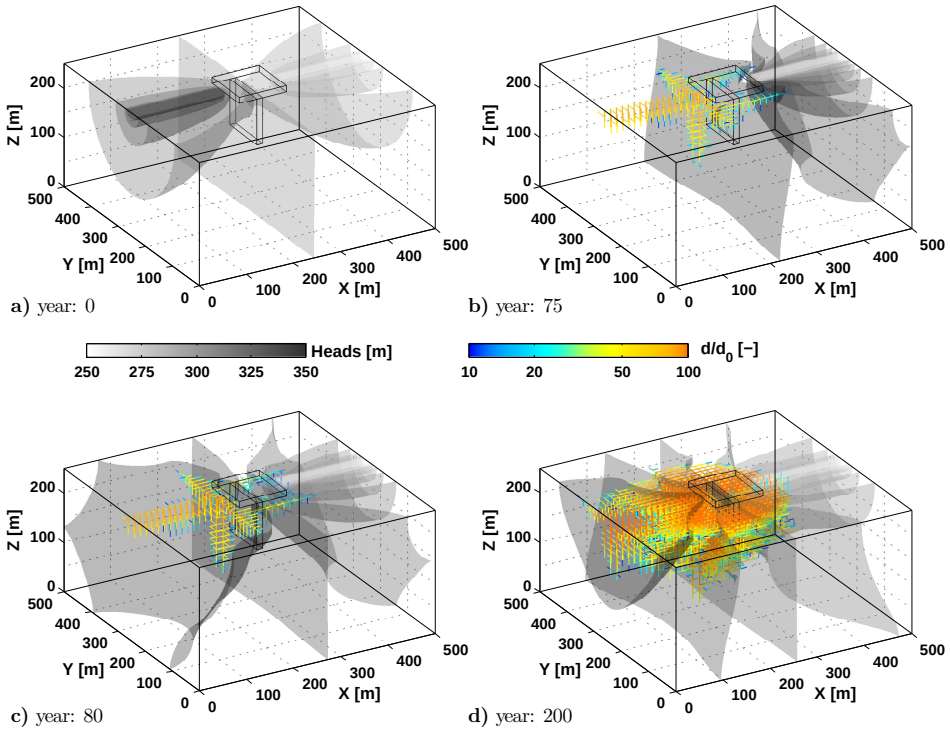


**Fig. 3.7:** Evolution of the standard model; Plotted are the isosurfaces of constant head from 250 m (light grey) to 350 m (dark grey) and the relative increase of the conduit diameter compared to the initial diameter on a log–scale from 10 (blue) to $\geq 100$ (orange); **a)** initial situation – isosurfaces of constant head are symmetrically spread around the dam; **b)** at t = 75 yr: conduit enlargement evolved vertically in front of the dam grout and horizontally around the dam flanks; **c)** at t = 80 yr: breakthrough has occurred at the downstream part directly behind the dam; head distribution starts to return to initial stage; **d)** at t = 200 yr: evolved network of widened conduits, high flux rates and rapid enlargement of conduit diameters – end of model run.

Fig. 3.7b depicts the evolution of the aquifer shortly before breakthrough at 75 years. Several conduits have enlarged symmetrically around the dam. The color code of the conduits ranges from blue (increase by a factor of 10) to orange (increase by a factor of $\geq 100$). Initially, the conduits enlarge equally below the reservoir. Because of the high hydraulic gradients close to the dam the foremost conduits are enlarging faster. Until $\approx 50$ years the vertical and horizontal conduits close to the dam–site are equally enlarged. Due to the much shorter horizontal paths

($L^c_{xy} = W + L = 200\,\text{m} < L^c_z = 2G + L = 300\,\text{m}$), the first breakthrough is likely to take place along the horizontal pathways on the right and left side of the dam–site.

The evolution of the aquifer after 80 years is shown in Fig. 3.7c. Breakthrough has occurred on both sides of the dam and the enlarged conduits reach the downstream part. The main flow through the domain is now through the horizontal conduits, which establish the breakthrough path. The head contours start to *rebound* to their initial position. This rebounding is clearly visible when looking on the dark grey isosurfaces for heads between 325 m and 350 m in Figs. 3.7b and 3.7c respectively. Like it was done before for the pseudo–3D model, it is assumed that there is enough water in the reservoir to keep the constant head boundary condition until the end of the model run at 200 years (Fig. 3.7d). Since the flow through the conduits increases after breakthrough, consequently also the flux rates increase and a dense network of enlarged conduits (orange) is established around the dam.

The general evolution of the aquifer beneath the dam seems at a first glance not much different from the pseudo–3D model shown above. But the inherent difference and obviously also the main advantage of a 3D model over the classical 1D and 2D models is the possibility that breakthrough paths can establish in any spatial direction around the dam. Depending on the 2D model, breakthrough path evolution is limited to either vertical or horizontal direction whereas this limitation does not exist in 3D.

### 3.2.2 Parameter Study

From the basic principles in 2.1 and the standard model shown in 3.2.1 the main parameters that drive the karstification process can be distinguished. The hydraulic head is strongly affected by the dam–site structure and reservoir depth, which leads to a set of different possible geometries to be investigated. Also the effect of the initial carbon–dioxide partial pressure on the karst aquifer evolution as part of the chemical parameters can be examined. In the 3D model setup the hydraulic conductivity of the domain depends strongly on the diameters of the conduit network. So the effect of different initial conduit diameters and / or their distribution is of considerable interest and can also be investigated. This is done by a sensitivity analysis or parameter study respectively. A similar parameter study has been carried out for 2D dam–site models by Romanov et al. (2003b) to evaluate the influence of the several parameters on the evolution of the karst aquifer.

#### 3.2.2.1 Varying grout depth $G$

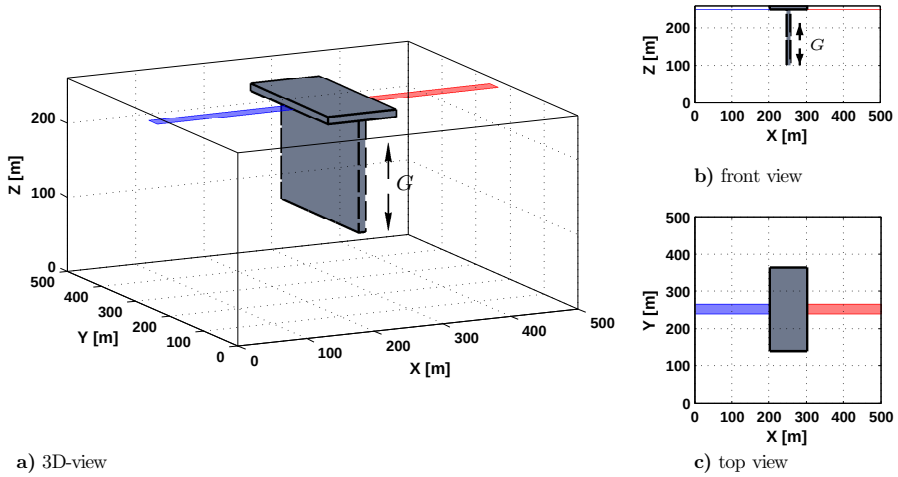


**Fig. 3.8:** 3D dam–site model setup with varying grout depth $G$; blue face represents location of constant head BC with $H = z_{max} + \Delta H$[m] (reservoir), red face represents location of constant head BC $H = z_{max}$ [m] (river); **a)** 3D–view; **b)** front view; **c)** top view.

To study the dependence of the breakthrough time $T_B$ on the grout depth $G$, the dam width $W$ of the standard model is extended to 225 m (see Fig. 3.8 – the arrows indicate which parameter is varied). Therefore, the vertical pathway $L_z^c = 2G + L$ of conduit enlargement around the grout curtain is always shorter than the horizontal one $L_{xy}^c = W + L$. This ensures that breakthrough will always occur along the vertical path.

The flow curves in Fig. 3.9a show the typical behaviour of the flow rates as already known from pseudo–3D models (3.1.2). The initial flow rates are almost constant for all different models and then increase rapidly over several orders of magnitude. After breakthrough the increase slows down significantly, but does not reach a constant level, due to fact that always a constant head boundary condition is kept, even after breakthrough. To save computational time the calculations were again stopped several time steps after the breakthrough occurred. That is why the upper level is not shown in the plots. Fig. 3.9b is a double logarithmic plot and shows the breakthrough time $T_B$ as a function of grout depth $G$. As expected the breakthrough time increases with increasing grout depth due to the extended pathway length.

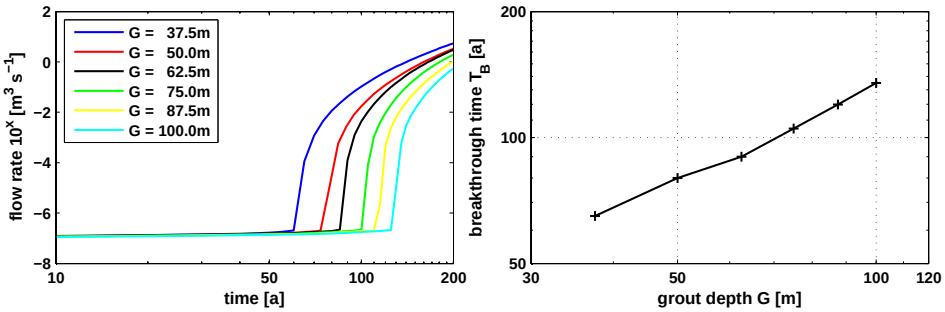


**a)** flow rates **b)** breakthrough time $T_B$

**Fig. 3.9:** **a)** flow curves for the 3D models with varying grout depths $G$ (37.5 – 100m) with the typical breakthrough behaviour; **b)** breakthrough time $T_B$ as a function of grout depth $G$ follows a power–law with $T_B \propto G^{0.75}$.

Comparing this result with the parameter study of Romanov et al. (2003b) it can be seen that a symmetric 3D model with a uniform conduit network (as used here) shows almost the same breakthrough behavior as a 2D model. The curve in Fig. 3.9b and therewith the dependence of the breakthrough time on the grout depth can be well approximated by a power–law with $T_B \propto G^{0.75}$.

#### 3.2.2.2 Varying dam width / length $W + L$

Now the effect of the horizontal dimensions of the dam on the breakthrough time is examined. If the 3D model has a uniform conduit network the influence of dam width $W$ and dam length $L$ should be similar to the one of the grout depth. To test this the grout depth was fixed to $G = 100$ m and the dam length was varied (see Fig. 3.10 – the arrows indicate that $L$ is varied). Because the conduit network is uniform and the dam–site layout is symmetric the horizontal directions can be treated together as horizontal pathway $W + L$.

The effect of the length of the horizontal path on which breakthrough occurs is shown in Figs. 3.11a+b. In Fig. 3.11a, the flow curves for the different models are plotted, and in Fig. 3.11b the corresponding breakthrough time as a function of the horizontal path length $W+L$. The first model in this set, with a path length of 100m ($W = L = 50$m) is quite unrealistic within the coarse discretization, but is shown for completeness. The breakthrough times increase from $T_B \approx 40$ years for a path length of 125m to $T_B \approx 160$ years for a path length of 300m. This relationship again obeys a power–law but this time with an exponent of 1.6 so that $T_B \propto [W + L]^{1.6}$

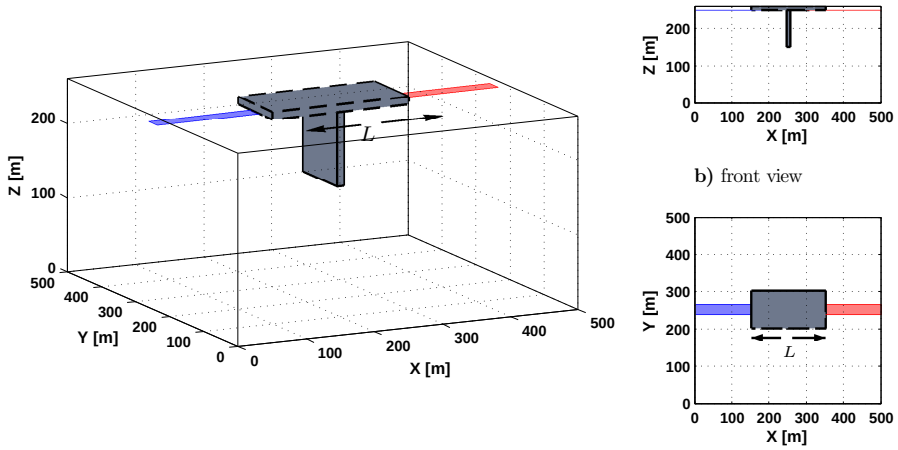


**a)** 3D-view **b)** front view **c)** top view

**Fig. 3.10:** 3D dam–site model setup with varying dam width / length $W + L$; blue face represents location of constant head BC with $H = z_{max} + \Delta H$ [m] (reservoir), red face represents location of constant head BC $H = z_{max}$ [m] (river); **a)** 3D–view; **b)** front view; **c)** top view.

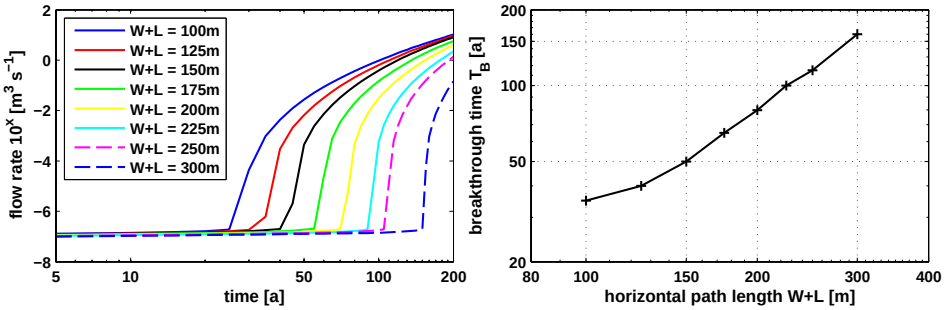


**a)** flow rates **b)** breakthrough time $T_B$

**Fig. 3.11:** **a)** flow curves for the 3D models with varying horizontal pathway $W + L$ $(50 - 300\text{m})$ with the typical breakthrough behaviour; **b)** breakthrough time $T_B$ as a function of horizontal pathway length $W + L$ follows a power–law with $T_B \propto [W + L]^{1.6}$.

#### 3.2.2.3 Varying reservoir depth $\Delta H$

Another crucial parameter is the depth of the impounded reservoir and therewith the hydraulic head. The dam–site geometry parameters $W, L, G$ are fixed for this test. In Fig. 3.12 the blue face and the arrows indicate the change of reservoir depth. The model domain is not extended in z–direction only the head boundary

condition at the nodes on top of the domain $Z = 250$m is adjusted.

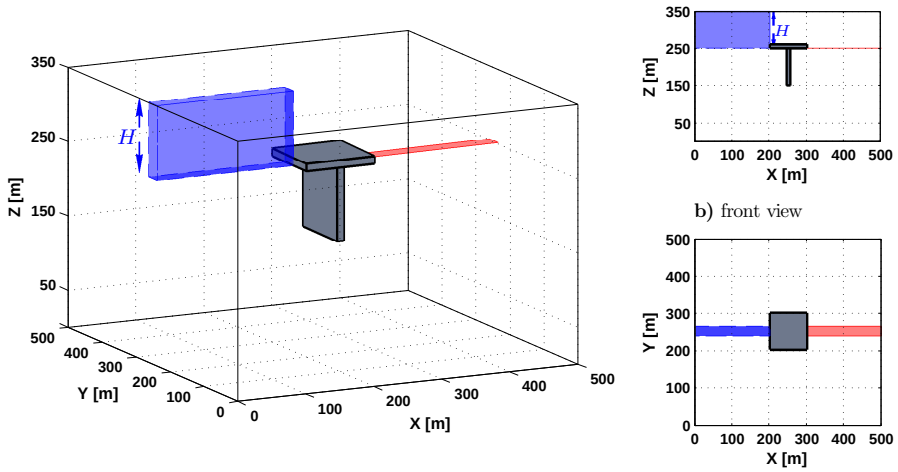


**a)** 3D-view **b)** front view **c)** top view

**Fig. 3.12:** 3D dam–site model setup with varying reservoir depth $\Delta H$; bottom of blue face represents location of constant head BC with $H = z_{max} + \Delta H$ [m] (reservoir), red face represents location of constant head BC $H = z_{max}$ [m] (river); **a)** 3D–view; **b)** front view; **c)** top view.

The results of this test are shown in Figs. 3.13a+b. Because of the different constant head boundary conditions, the base–flow component (the initial flow) of the flow curves in Fig. 3.13a differs from each other. With increasing head, of course the base–flow component increases and the breakthrough time therefore decreases proportionally. For a reservoir depth of 25m, breakthrough happens at $T_B \approx 350$ years. If the reservoir depth increases to 250m the breakthrough time decreases to $T_B \approx 40$ years. From Fig. 3.13b, one can see that the head dependency can almost be perfectly approximated by a power–law $T_B \propto H^{-1}$.

#### 3.2.2.4 Varying carbon-dioxide partial pressure $pCO_2$

Figs. 3.14a+b show the influence of the carbon–dioxide partial pressure in the water on the evolution of the karst aquifer system for the standard model. Kaufmann (2003c) has also shown the influence of carbon–dioxide partial pressure on the evolution of leakages rates beneath dam–sites. There the author used a 2D model and varied the partial pressures of $CO_2$ within the reservoir to drive the karstification by mixing corrosion. One of the models presented there had comparable properties

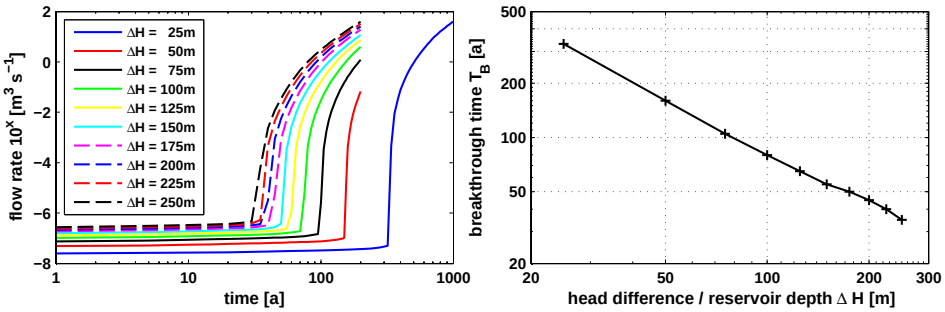


**a)** flow rates **b)** breakthrough time $T_B$

**Fig. 3.13:** **a)** flow curves for the 3D models with varying reservoir depth / hydraulic head difference $\Delta H$ $(25 - 250\text{m})$ with the typical breakthrough behaviour; **b)** breakthrough time $T_B$ as a function of hydraulic head difference $\Delta H$ follows a power–law with $T_B \propto H^{-1}$.

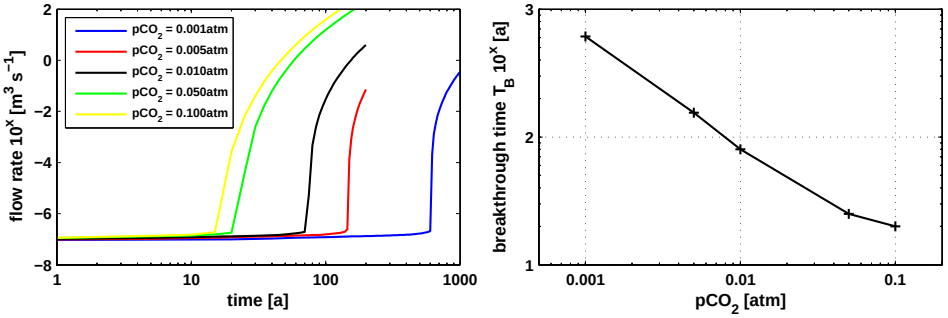


**a)** flow rates **b)** breakthrough time $T_B$

**Fig. 3.14:** **a)** flow curves for the 3D models with varying carbon–dioxide partial pressure $pCO_2$ $(0.001 - 0.1\text{atm})$ with the typical breakthrough behaviour; **b)** breakthrough time $T_B$ as a function of carbon–dioxide partial pressure $pCO_2$ follows a power–law with $T_B \propto pCO_2^{-0.8}$.

(dam width, grout depth, calcium input concentration and $pCO_2$) and showed a similar breakthrough behaviour as the model tested here (red curve in Fig. 3.14a).

Here, the input concentration was always set to $c_{in} = 0$ and the carbon–dioxide partial pressure was varied over two orders magnitude from 0.001atm to 0.1atm. For lower values of $pCO_2$, the calculation time had to be extended to 1000 years to fully cover the breakthrough event. The breakthrough time for $pCO_2 = 0.1\text{atm}$ (yellow curve) is slightly shifted from the ideal $T_B \propto pCO_2^{-0.8}$ approximation in Fig. 3.14b. This appears to be a numerical artifact due the very fast breakthrough within a few

time steps in combination with the coarse discretization.

#### 3.2.2.5 Varying initial conduit diameter $d_0$

As stated by the authors who investigated the breakthrough behaviour of 1D, 2D or 3D karst models, the conductivity affected by the conduit diameters inside the modelling domain is a crucial criterion for determining the breakthrough time. Fig. 3.15b shows the breakthrough time as a function of the initial conduit diameter $d_0$ on a double logarithmic scale. Decreasing $d_0$ from 0.3mm in the standard model to $d_0 = 0.1$ mm increases the breakthrough time by more than one order of magnitude to $\approx 2500$ a. This dependence can be quite well approximated by a power–law with $T_B \propto d_0^{-3}$, which corresponds also to the 1D and 2D results shown e.g. by Dreybrodt (1996); Siemers and Dreybrodt (1998); Dreybrodt and Gabrovšek (2000) (1D), and Romanov et al. (2003b) (2D). In Fig. 3.15a, one can see how the initial conduit diameter of the network directly controls the conductivity of the whole modeling domain. Due to the higher conductivity, the base–flow component of the flow curves increases by almost three orders of magnitude.

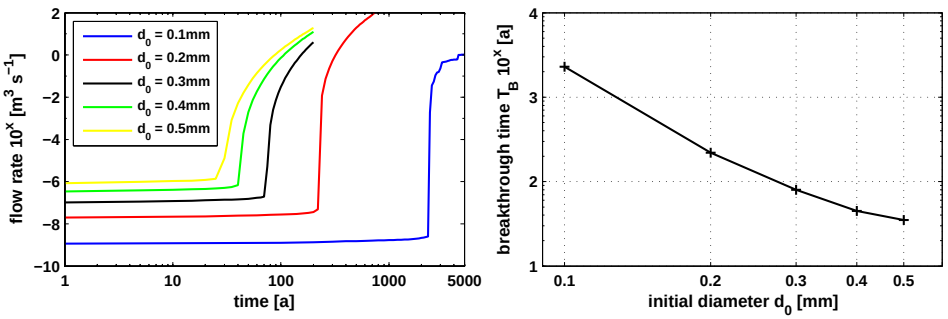


**a)** flow rates **b)** breakthrough time $T_B$

**Fig. 3.15:** **a)** flow curves for the 3D models with varying initial conduit diameter $d_0$ $(0.1 - 0.5\text{mm})$ with the typical breakthrough behaviour; **b)** breakthrough time $T_B$ as a function of initial conduit diameter $d_0$ follows a power–law with $T_B \propto d_0^{-3}$.

With the proportionality parameters derived from the simulations described above, it is now possible to compare the results with the 1D breakthrough equation 2.17. Incorporating all power–law approximations one gets

$$T_B^{3D} \propto \underbrace{\left[\frac{(W+L)^{1.6}G^{0.75}}{H}\right]}_{1} \cdot \underbrace{d_0^{-3}}_{2} \cdot \underbrace{pCO_2{}^{-0.8}}_{3}. \tag{3.1}$$

The first part of this relation applies to the geometric parameters of the 3D model, the second part to the conduit network, and the third part to the partial pressure of carbon–dioxide respectively. This relation can of course not be taken as a universal formula to determine the breakthrough time of an arbitrary 3D dam–site model. It is given here to show that for simple setups the 3D models behave in a similar way as the 2D and 1D models presented in the past. Actually the conclusion should be reversed. The parameter study accomplished here shows, that the 1D and 2D models used in the past, even with the lack of the spatial dimensions have been a good approximation for simple (symmetrical) 3D models.

### 3.2.3 Non–uniform / statistical network

The next step in approaching realistic scenarios is to implement a statistical or non–uniform distribution of the initial conduit diameters $d_0$ of the network. An example of such a distribution has already been given in 2.2 (Fig. 2.5).

When using a statistical network, the model is now a real 3D model because there is no symmetry in any dimension and the three spatial dimensions are therefore completely independent from each other. A statistical 3D model can no longer be compared directly to 2D and 1D models. When using a statistical network, the preferential breakthrough path or the breakthrough time, even for simple dam–site models cannot be predicted by the shape of the dam–site. It depends strongly on the spatial distribution of conduit diameters inside the network. This was already shown for 2D networks, e.g. by Hanna and Rajaram (1998); Romanov et al. (2003b), and Siemers and Dreybrodt (1998). Of course in regimes close to equilibrium (high order kinetics) and / or small hydraulic gradients the evolution is more dominated and controlled by the dissolution chemistry i.e. by the saturation of the subsurface water. For instance, if two solutions with different equilibrium concentrations and saturated with respect to calcite are mixed, the solution becomes again undersaturated and aggressive and can therefore dissolve calcite. This mechanism is called *mixing corrosion* and described e.g. in Bögli (1980); Gabrovšek and Dreybrodt (2000, 2010).

In most cases described in literature concerned with karst evolution modelling, a log–normal distribution is chosen. This is also done here. To show the influence of a statistical network a log–normal distribution is added to the standard model from 3.2.1. The assignment of the initial conduit diameter is random within the model domain and therewith the diameters do not correlate spatially. The log–normal distribution in the example shown here has parameters $\hat{d}_0 = 0.3$ mm and $\sigma_n = 0.2$ mm and is created as described in 2.2.

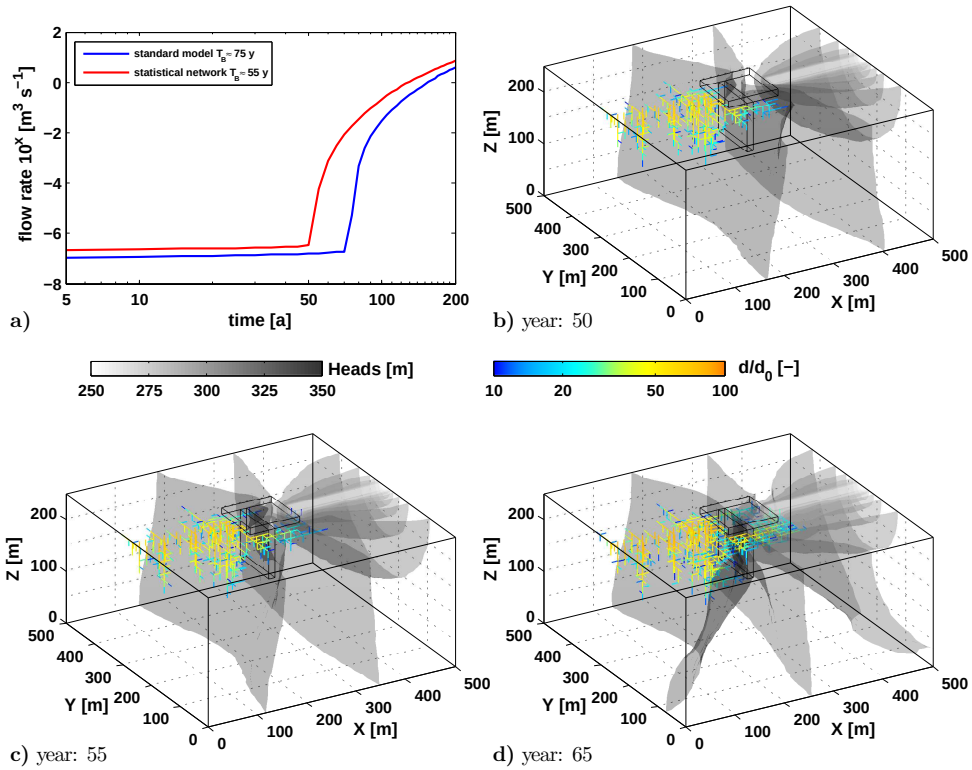


**Fig. 3.16:** Evolution of the standard model with a statistical conduit diameter distribution ($\hat{d}_0 = 0.3$ mm, $\sigma_n = 0.2$ mm); **a)** flow curves of the standard model (blue) and statistical model (red), for the statistical model the breakthrough time is decreased by $\approx 20$ years; **b)** after 50 years asymmetrical conduit enlargement at the upstream part of the dam, preferential pathway due to larger initial conduit diameters on the right side of the dam will be taken for breakthrough; **c)** after 55 years breakthrough has occurred only on the right side of the dam, the head distribution has already started to return to its initial stage; **d)** after 65 years the enlarged conduits on the left side of the dam have also reached the downstream part.

Analyzing the flow rates in Fig. 3.16a, it is obvious that due to the influence of the statistical network the breakthrough time is significantly decreased from $\approx 75$ years to $\approx 55$ years, compared to the standard model. Furthermore, the flow of the statistical network model has a slightly higher base component, due to the preexisting larger conduits and therefore higher hydraulic conductivity. In Fig. 3.16b, the evolution after 50 years is shown. One difference from the standard model plot in Fig. 3.7 is that the isosurfaces of constant head are no longer smooth planes. Because of the non–uniform network they are slightly distorted. Clearly visible now is the asymmetric enlargement of the conduits due to their statistical distribution. The initially wider conduits started to evolve at three main locations, irregularly spread along the reservoir. Furthermore, one can see the evolving pathway on the right side of the dam–site which in this model is the breakthrough pathway. Fig. 3.16c shows the evolution of the aquifer at 55 years right after breakthrough. Breakthrough has now occurred on the right side of the dam, and the isosurfaces of the head distribution have already started to rebound, whereas the path on the left side of the dam is still evolving. In Fig. 3.16d, the situation at 65 years is shown. The conduit enlargement on the left side of the dam has now also reached the downstream part, as indicated by the rebounding isosurfaces. The evolution continues from now on similar to the standard model, enlarging all conduits around the dam, so that the picture after 200 years of evolution would be comparable to Fig. 3.7d.

### 3.2.4 Model with topography

In the last part of this chapter topography is implemented into the 3D model, which is a necessary step when modeling real case scenarios. For this reason, the standard model is extended to 350 m height and a simple valley structure is added (Fig. 3.17a). This layout is close to the conceptual model domain shown in 3.1.1. Note that the different brown colors of the valley in Fig. 3.17 represent different topographic heights and not a layering of the bedrock structure. The valley itself is 100 m deep with a bottom width of the reservoir of 12.5 m and increasing upwards to a top width of 75 m. The dam as a simple rectangular structure with a sealing apron of $100 \times 100\,\mathrm{m}^2$ and a total height of 100 m to be comparable to the standard model. The grout has a depth of 100 m and is centered below the dam block. For this topographic setup the resolution of the grid is doubled compared to the standard model to $81 \times 81 \times 57$ nodes, yielding a discretization of $dx = dy = dz = 6.25$ m.

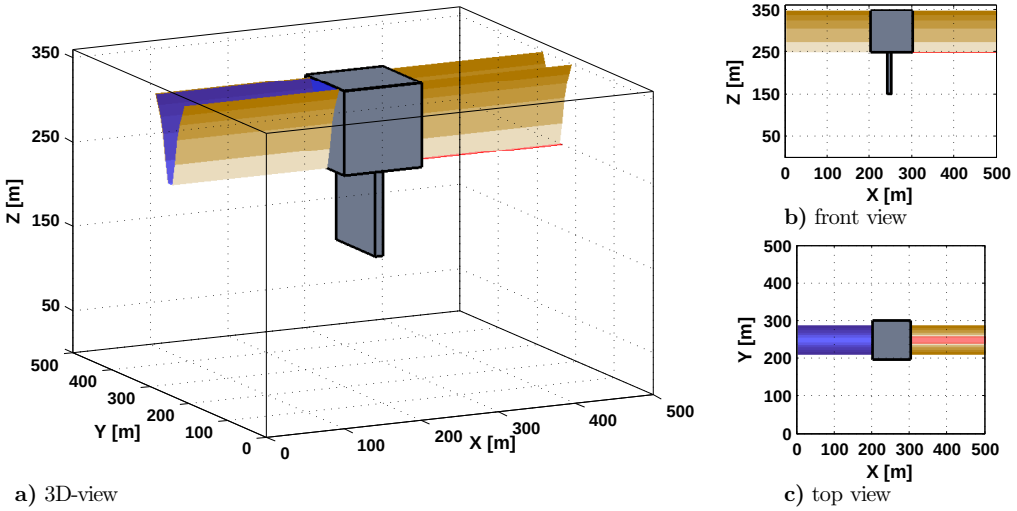


**a)** 3D-view **b)** front view **c)** top view

**Fig. 3.17:** 3D dam–site model setup with topography; blue face represents location of constant head BC with $H = z_{max} + \Delta H$[m] (reservoir), red face represents location of constant head BC $H = z_{max}$ [m] (river); **a)** 3D–view; **b)** front view; **c)** top view.

With this high resolution the model now consists of 373 977 nodes, 358 400 matrix elements and almost 1.1 million conduits. Such high resolution models make high demands on the applied software for the numerical simulation as well as on the applicable hardware. The fast computer development in the last 30 years has laid the foundation of simulating complex physical systems by numerical means. The influence of the chosen model size on the computation time and storage requirements was also investigated during this work. For a summary on the performance of KARSTAQUIFER see appendix A.

The boundary conditions for the topography model are the following. At the upstream part, the reservoir (blue – constant head boundary) has a depth of 100 m in the center of the valley. At the downstream part the river is a constant head boundary of 1 m above the valley bottom. Under real conditions construction measures would be carried out to prevent the water from discharging through the valley flanks. This could either be sealing the valley flanks close to the dam–site or horizontally grouting in addition to the vertical grout. For simplicity the valley flanks in the downstream part are assumed to be no flow boundaries. All domain parameters are identical to the standard model. The initial conduit diameters $d_0$ of the network are again log–normally distributed without any spatial correlation with $\hat{d}_0 = 0.3\,\text{mm}$

and $\sigma_n = 0.2$ mm.

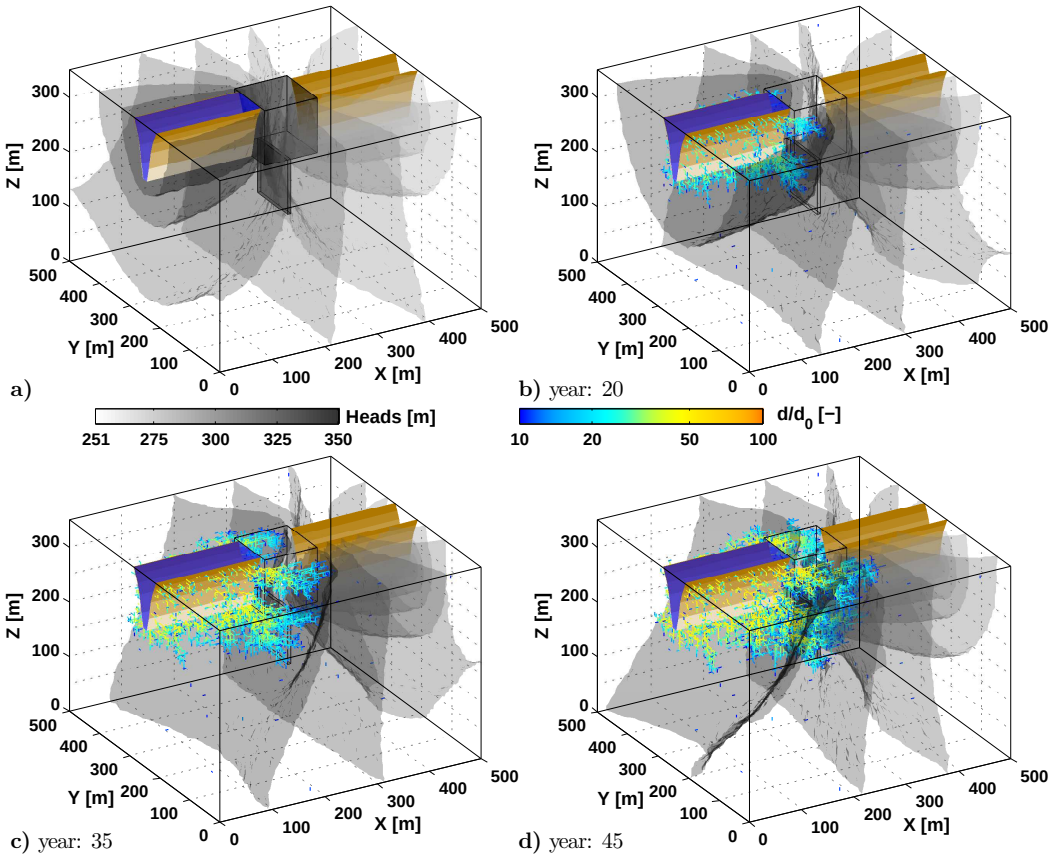


**Fig. 3.18:** Evolution of the standard model with topography and a statistical conduit diameter distribution ($\hat{d}_0 = 0.3$mm, $\sigma_n = 0.2$mm); **a)** initial situation, heads are symmetrically distributed around the dam–site **b)** after 20 years of evolution initial channels have started to grow horizontally from the valley flanks and vertically in front of the grout; **c)** after 35 years the horizontal paths have almost reached the downstream part of the dam–site **d)** after 45 years breakthrough has occurred and the upper and deeper conduit paths have connected.

Fig. 3.18a shows the initial head distribution. The heads are almost symmetrically distributed around the dam-site but again slightly distorted due to the statistical network, as it can be seen from the grey shaded isosurfaces. The color code for the head isosurfaces is the same as for the previous models. Fig. 3.18b shows the evolution after 20 years. Clearly visible are several irregular pathways of enlarged conduits. Two main horizontal paths at $\approx$ 325m height on both sides of the dam–

site, one horizontal path at ≈ 250m height, evolving from the valley bottom around the right side of the dam, and a bigger cluster of enlarged conduits at the upstream part of the dam–site in front of the dam grout. These four pathways are competing, where probably one of the first three will be the initial breakthrough path. The evolution of the aquifer after 35 years is shown in Fig. 3.18c. The conduit paths continued to evolve and have now almost reached the downstream part of the dam. What is hardly visible due to the 3D view is, that the downstream ends of the enlarged horizontal pathways on the right side of the dam–site are at $X \approx 300$m. Fig. 3.18d shows the evolution of the aquifer after 45 years. From the rebounding of the head isosurfaces (dark grey colors) one can see that breakthrough has already occurred. The breakthrough short–circuit was closed first at the lower horizontal pathway on the right side of the dam–site. After the breakthrough event, the conduits from the upper horizontal pathway have connected with the deeper conduits. Calculating the model further would lead to continuously evolving conduit network (like for the standard model before) inside the whole domain due to the fixed head boundary conditions.

## 3.3 Conclusions

In this chapter a 3D model of the evolution of a karst aquifer system beneath a dam–site was presented. It was demonstrated that the new program KARSTAQUIFER (Kaufmann, 2009; Kaufmann et al., 2010) is well suited for 3D karst evolution modeling of dam–sites and reservoirs. The model domain consists of a homogeneous limestone block. It contains a network of initially fine fractures / conduits which are widened during the evolution by dissolution of calcite from the bedrock. The diameters of the conduit network can be uniformly or statistically distributed. The insoluble dam–site was positioned in the center at the top of the domain with the inflow nodes (reservoir) in the upstream part and the outflow nodes (river) in the downstream part of the dam respectively. The possibility of incorporating topographic models into high resolution 3D model setups was shown also.

When using very simple and symmetrical 3D models, they can be compared to previous 2D or even 1D models. For these special cases all three setups show a common inherent evolutionary behavior, so that to a certain degree the effect of different model parameters on the evolution is also analogous. This effect could be

clearly shown with the pseudo–3D models.

So one of the main conclusions of this chapter refers to the 1D and 2D models for the evolution of karst aquifers beneath dam–sites. They have been proven and tested tools to simulate basic interactions of reservoir properties (geometry) and aquifer evolution. But they are of course limited to very simple layouts and model geometries. As real dam–sites and reservoirs can be arbitrarily complex, there is obviously a need for 3D karst evolution models that can cope with this complexity to a certain extent.

This chapter has shown that the program KARSTAQUIFER can be used to simulate karst evolution models in 3D. It is possible to create very complex models in terms of varying geological and hydrogeological parameters. That this is an important fact for considering real world examples will be shown in the next chapter, where the evolution of karst aquifer below a real dam–site is presented.

Chapter 4

# A 3D karst evolution model of a real dam–site – The Birs weir

After the conceptual models and simple 3D dam–site scenarios have been presented in the previous chapter, now a real dam–site is considered. Here, the 3D karst evolution model is applied to the Birs weir[1] in Switzerland. This location is chosen, because there is already a lot of experience gained with e.g. integrated hydrogeological modelling and 2D karst evolution modelling. The development of a 3D karst evolution model is the consequential extension of the previous works and the attempt to overcome some of their inherent limitations. For instance the 3D hydrogeological model (3DHGM) presented by Epting et al. (2009a,b) uses a standard porous flow model to simulate the groundwater flow through the aquifer. By this it lacks essential characteristics, like fractures and their temporal evolution, that are very important for understanding the hydraulics of karst aquifers. Also the 2D karst evolution models by Romanov et al. (2010, 2012) only give a fractional view of the Birs aquifer system. Though they account for the temporal evolution of the aquifer, they lack the influence of the third spatial dimension. It will be shown that the Birs weir aquifer is a heterogeneous 3D karst system. For the first time a 3D karst evolution model is used, to describe the temporal evolution of an aquifer beneath a real dam–site.

The Birs weir is a small dam–site built in the 1890's, which is still used to support a small power plant with water (Golder, 1984). Despite its small extent it had and still has a significant effect on the local aquifer system. In the 1960's a highway was constructed close to the eastern river bank. Starting with small subsidence events of the highway and the weir itself, the vertical movements increased and in the 1980's several sinkholes developed beneath the highway (Epting et al., 2009a). To stabilize the highway and to prevent further karstification, extensive construction measures have been carried out between 2006 and 2007. Alongside with these measures, several geological, hydrogeological and geophysical field studies provided a large amount of data and were therefore the foundation of the previous works and the current modelling approach. An integrated interpretation of 3D hydrogeological modelling, ERT geophysics and 2D karst evolution modelling can be found in Epting et al. (2009b).

This chapter presents the development of a 3D model for the evolution of the Birs aquifer after the construction of the Birs weir. This development includes the incorporation of available field data into the setup of the model and the calibra-

[1]For simplicity the location of interest is referred to as *Birs weir* throughout this work.

tion of the model parameters to the given boundary conditions. It is shown that roughly one hundred years are enough to alter the local aquifer system significantly. The combination of the local Gipskeuper bedrock and the increased hydraulic head caused by the weir are most likely the main source of the observed subsidence. At the end of this chapter it will be shown that a reasonable model is found that reproduces the evolution of the aquifer and its geometry. Finally, an outlook on the possible future evolution of the aquifer after the remedial measures is given also.

The essential findings of this chapter have been presented in Hiller et al. (2012b).

## 4.1 The model setup

### 4.1.1 Site description

**Location** The Birs weir is located $\approx$ 5km upstream the Birs river from the junction to the river Rhine, south of the Swiss city of Basel close to the German border (Fig. 4.1a). For a few hundred meters around the Birs weir the Birs river flows parallel to the four–lane highway H18 connecting Basel with Delemont (Fig. 4.1b). The height difference between the impounded water in the upstream part and the river in the downstream part is $\approx 7$ m. The water in the upstream part infiltrates through the quaternary riverbed ($5 - 10$ m thickness) into the bedrock and flows vertically and horizontally around the weir and exfiltrates back into the river in the downstream part (Epting et al., 2009a). The bedrock mainly consists of Triassic Gipskeuper which is composed of alternating thin layers of gypsum and marls (Fig. 4.2c; darker areas in the picture refer to marls, brighter areas to gypsum respectively).

**Weathered Zone – WZ** On its way through the bedrock the aggressive water dissolves the gypsum parts and has therewith created a weathered zone (WZ) with increased hydraulic conductivity. In Figs. 4.2a+b this WZ is schematically drawn with cyan color. Note that the WZ in Fig. 4.2a extents horizontally towards East below the highway and does not follow the topography (Because of the perspective of the figure the reader may misleadingly assume the latter.). The extent of the WZ, especially below the highway, is quite well known due to many observation wells and construction works around the Birs weir. The WZ reaches depths of $\approx 20 - 30$ m

[2] http://openstreetmap.de/karte.html?zoom=14&lat=47.52407&lon=7.62408&layers=B0000TT

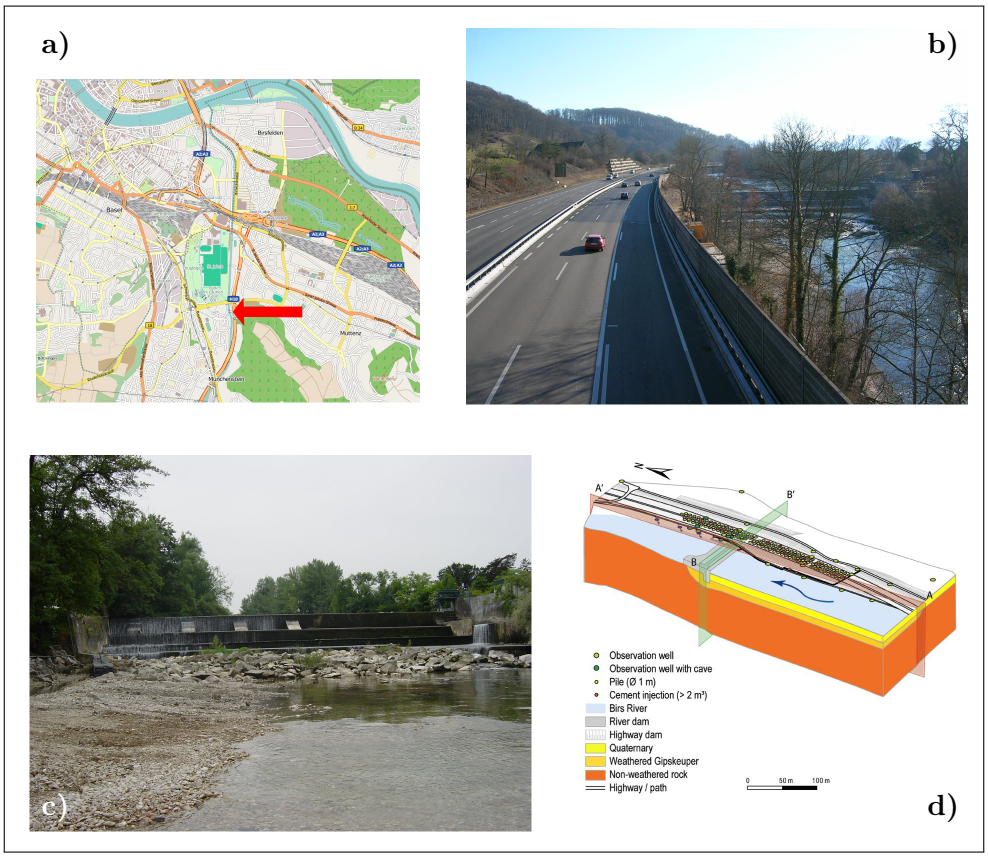


**Fig. 4.1:** The Birs weir site; **a)** map[2] showing the location of the Birs weir (red arrow); **b)** Photo showing the highway and the Birs weir from direction North; **c)** Photo showing the Birs weir from direction North; the water is overflowing the weir on the east part **d)** 3D hydrogeological model; **b,c+d** from Epting et al. (2009b).

and extends $\approx 250$ m parallel to the Birs river below the highway with maximum widths of $\approx 70 - 80$ m to the East. Below the river the extent of the WZ is rather speculative. ERT measurements parallel to the river close to the road, as well as underwater ERT measurements in the upstream part of the river have been carried out to gather more information about the site. The interpretation of the ERT measurements indicates karstified zones below the upstream part of the river as well as below the weir itself (Epting et al., 2009a, 2012). Nevertheless, the WZ can not be considered as a homogeneous block of higher hydraulic conductivity. It is rather a zone were field experiments and observations found an increased number of karst features such as voids, conduits and caves (Epting et al., 2009a).

While the gypsum content in the non-weathered bedrock reaches up to 50 %, the gypsum content of the WZ ranges between 5 % and 15 % (information derived from borehole descriptions). The 3DHGM presented by Epting et al. (2009b), used groundwater head data from observation wells to calibrate the hydraulic parameters of the aquifer. In situ hydraulic conductivity values for Gipskeuper range between $K \approx 1 \times 10^{-14}\,\mathrm{m\,s^{-1}}$ and $K \approx 1 \times 10^{-7}\,\mathrm{m\,s^{-1}}$ (NAGRA, 2002). If the Gipskeuper is weathered it becomes highly heterogeneous and the hydraulic conductivity of the aquifer can significantly change on a local scale. For the 3DHGM the calibrated hydraulic conductivities are $K \approx 1 \times 10^{-5}\,\mathrm{m\,s^{-1}}$ for the non–weathered bedrock, $K \approx 1 \times 10^{-4}\,\mathrm{m\,s^{-1}}$ for the WZ and $K \approx 1 \times 10^{-3}\,\mathrm{m\,s^{-1}}$ for the quaternary riverbed. These conductivity values give the rough framework for this study and will be used for the matrix conductivity $K_m$ and the conduit conductivity $K_c$ respectively. For a detailed description of the characteristics of the Birs site the reader is referred to Epting et al. (2009a,b) and the references therein.

### 4.1.2 Modelling domain

The model domain in this work is a 250 m × 350 m × 200 m Gipskeuper block. It is created by a grid of 51 × 71 × 41 nodes to achieve a grid discretization of $dx = dy = dz = 5\,\mathrm{m}$. This gives a total of 148,461 nodes, 140,000 matrix elements and 429,640 conduit elements. With this resolution the computational time for one single run is kept on an acceptable level. Every element (matrix and conduit) can be assigned with individual properties. As it can be seen from Fig. 4.2c the gypsum layers (lenses) are not uniformly distributed. It is assumed that this holds true for the whole domain and not all conduits inside the model may cross soluble layers. To account for this and the general gypsum content of 50 % for the Gipskeuper bedrock, only 50 % of all conduits are randomly marked soluble. The remaining conduits are insoluble and therefore their initial diameter $d_0$ will not change during the evolution. This concept was already used by Romanov et al. (2010, 2012) to consider the heterogeneity of the karst bedrock. The initial conduit diameters are created with a log-normal distribution (see 2.2).

For 2D models Romanov et al. (2010) showed, that for a heterogeneous bedrock like Gipskeuper, it is necessary to consider also the limited widths of the soluble layers when modelling the evolution of such an aquifer. They introduced a parameter $a_{lim}$ that assigned every single fracture inside the domain a maximum aperture

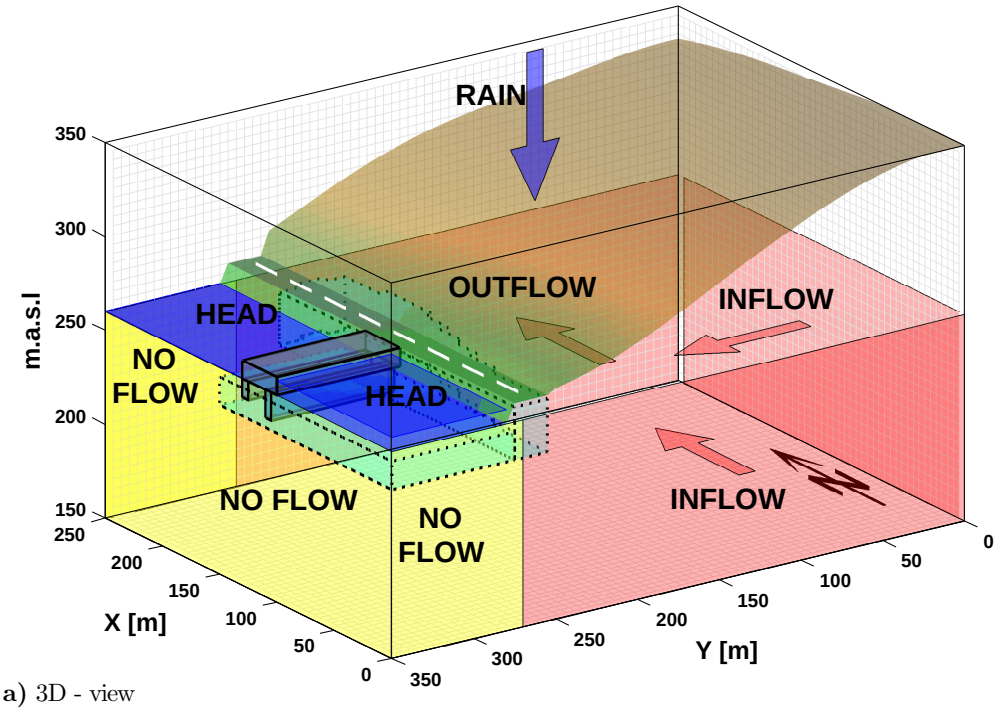


**a)** 3D - view

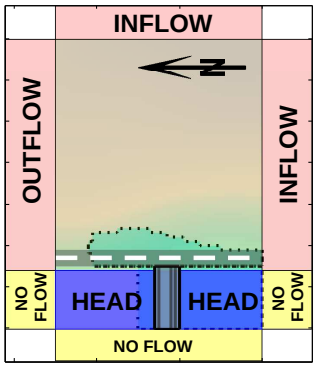


**b)** Top view

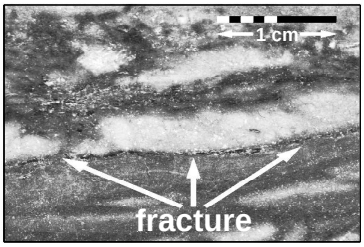


**c)** Rock sample

**Fig. 4.2: a)** Sketch of the model domain, setup and boundary conditions (BC); the discretization is indicated by thin grey lines; shown are topography (brown-green surface), river – constant head BC (dark blue faces), highway (grey with white dashed line), dam – weir (grey with black edges), assumed weathered zone WZ (cyan), flow BC (red faces and arrows), no flow BC (yellow); **b)** Top view of the model domain and the BC; **c)** Rock sample from the local Gipskeuper, with Gypsum (white) and marl (grey) layers visible; white arrows point to a fracture between the gypsum and marl layer.

width to which it could grow. When this maximum was reached the growth of the fracture was stopped. Thereby larger amounts of undersaturated solution were able to penetrate into the bedrock. The limited widening presented for their 2D models had a decisive effect on the evolution of a gypsum karst aquifer, especially close to a dam–site. With the *standard* unlimited widening scheme only the fractures close to the entrance were growing and no breakthrough occurred. In contrast, the limited widening scheme was able to create karstified zones and even preferential (breakthrough) pathways around the dam structure.

According to the current knowledge that most of the Gipskeuper around the Birs weir is composed as shown in Fig. 4.2c, the limited widening approach by Romanov et al. (2010) is also used here. Like for the initial conduit diameters, the maximum conduit diameters are also drawn from a log–normal distribution. Both distributions are then statistically spread to all conduits in the domain. If within one time step of a calculation a conduit diameter grows so that[3] $d^j(t_i) \geq d^j_{max}$, then $d^j(t_i) = d^j_{max}$ is set and the conduit is marked insoluble for the remaining calculations.

The model domain also accounts for the local topography (brown–green face in Figs. 4.2a+b). This may be of importance as close to the highway a small hill elevates (see Fig. 4.1b). Generally, using a topography is a great improvement compared to the 3DHGM and the 2D karst evolution models. The topography information is extracted from SRTM data and interpolated onto the grid discretization (Farr et al., 2007). Due to the $5\,\mathrm{m} \times 5\,\mathrm{m} \times 5\,\mathrm{m}$ element size the topography data for the riverbed and the highway had to be smoothed. In the model the riverbed has a constant elevation of 260 m.a.s.l. and the road a constant elevation of 270 m.a.s.l. respectively. The quaternary riverbed extends from $250 - 260$ m.a.s.l., all conduits there are insoluble and the initial diameter $d_0$ is increased to account for a hydraulic conductivity of $K \approx 1 \times 10^{-3}\,\mathrm{m\,s^{-1}}$.

Like for the dam–site models in 3 the flow through all weir elements and conduits is blocked to achieve impermeability.

### 4.1.3 Boundary conditions

With a 3D karst evolution model it is possible to account for the complex boundary conditions at the Birs weir location. As the processes that drive karstification are well understood, the objective is to find a model setup that can explain the present

[3] $j$ here denotes an individual conduit index

day situation around the Birs weir within reasonable boundary conditions.

**River and West boundary** From the field studies it is known that the western bank of the riverbed consists of Triassic Schilfsandstein and is therefore assumed impermeable and insoluble for all presented model setups. The western no flow boundary is marked with a yellow face in Figs. 4.2a+b. The upstream and downstream parts of the river are constant head boundary conditions (blue faces in Figs. 4.2a+b), where the downstream part has a constant head value of 0.4 m above the riverbed. The upstream part has a constant head value of 7.7 m to account for the average seasonal head difference of 7.3 m between up– and downstream part. The river water is assumed to be aggressive with respect to gypsum and therefore the calcium input concentrations at the river nodes is set to $c_{in} = 0\,\mathrm{mol\,m^{-3}}$.

**Local flow regime** The regional groundwater flow is from South to North parallel to the river. Locally, the small hill in the east part of the domain elevates the water table. Therewith the hill induces a flow component towards the river in a way that the flow is from East to West. From field studies it is known that this westward flow does not hold true for the entire region around the Birs weir. Further downstream (outside of our model domain) there are also parts where the water infiltrates into the bedrock due to the local geology. In our model domain the impounded water in the upstream part creates a flow component from West to East opposed to the flow from the hill. Both waters then meet in a convergence somewhere in the center of the domain. This convergence is of course not locally fixed but moves eastwards and westwards due to seasonal changes of the river water table and the annual rainfall. This quite complex flow regime was successfully modelled with a 3DHGM in Epting et al. (2009b).

**Flow boundary conditions** To account for the local flow regime we use constant flow boundaries on the South, North and East parts of the domain. Red faces in Figs. 4.2a+b mark constant flow boundary conditions. The red arrows indicate the direction of flow. The South and East faces are constant inflow boundaries, the North face is a constant outflow boundary, respectively. To get comparable results the North and South flow boundaries are calibrated to the hydraulic heads of the 3DHGM presented by Epting et al. (2009b). This means that the flow values along these boundaries are kept small enough ($\ll 1\mathrm{ls}^{-1}$) to assure that the calculated heads

do not exceed the hydraulic heads from the 3DHGM and therewith are in agreement with the groundwater head data from the observation wells. The reader may notice the no flow boundary parts along the South and North boundary directly below the river (yellow faces in Figs. 4.2a+b). They are implemented for pure technical reasons. If constant flow conditions would be used there, the head gradient between the river and the boundary would have artificially increased and / or short cuts between the river and the boundary would have established. With the no flow boundary condition there, the constant head boundary condition of the river can be assured.

Calibration of the East flow boundary was done in a way that for all calculated model runs the convergence described above was established. The resulting flow values ($\geq$ 10 $\mathrm{ls}^{-1}$) are also comparable to the boundary conditions used in the 3DHGM. From the chosen flow values one can already speculate that the East boundary and its interaction with the flow from the river, may have a stronger effect on the evolution of the WZ compared to the North and South boundaries.

For all three flow boundaries it is assumed that water entering the domain through these boundaries is already saturated and therefore $c_{in} = c_{eq}$.

**Topography boundary conditions** Also the topography is a domain boundary. Here, the mean annual precipitation of 946 mm/a is distributed to all surface nodes. Because nothing is known about the unsaturated / vadose zone, it is assumed that there are already some enlarged fractures in the bedrock that provide flow paths to the water table. The rain water that enters the bedrock flows along these paths, dissolves the bedrock and its calcium concentration is increased. Because the crossing of the vadose zone is assumed to be rather fast, the water that finally reaches the water table is still slightly undersaturated with respect to calcium and therefore still able to dissolve gypsum. Considering this concept, the calcium input concentration of the rain (effectively the additional water at the water table) is set to $c_{in} = 0.99 c_{eq}$ mol $\mathrm{m}^{-3}$. 2D models presented e.g. by Gabrovšek and Dreybrodt (2001); Kaufmann (2003b) show the interaction between recharge (precipitation), the vadose zone and the phreatic zone. They show the evolution of karst features along the water table if the water that reaches the water table is not yet completely saturated with respect to calcium. The effect of the topography boundary and the precipitation for the Birs weir is shown in 4.2.1.4.

## 4.2 Results

First the model calibration is explained and then the model complexity is stepwise increased to show a reasonable present–day situation. Finally, this *optimal* present–day model is used to give a future outlook of the Birs site. Therefore, the remedial measures (sealing pile wall – see Epting et al. (2009b)) towards the highway are added to the model and their influence is studied.

### 4.2.1 Present

#### 4.2.1.1 Model calibration

In a first step the model is calibrated to the 3DHGM. So far the 3DHGM was only used to calibrate the boundary conditions.

The matrix conductivity for every element is set to $K_m = 1 \times 10^{-5}\,\mathrm{m\,s^{-1}}$, which is the value used in the 3DHGM for the non–weathered Gipskeuper (Epting et al., 2009b). As the global hydraulic conductivity is composed of matrix conductivity $K_m$ and conduit network conductivity $K_c$, an initial conduit diameter distribution needs to be found that represents the hydraulic conductivity of the non–weathered Gipskeuper. Therefore, a reference block is defined with the 3DHGM, that has a homogeneous conductivity of $K_m = 1 \times 10^{-5}\,\mathrm{m\,s^{-1}}$ and a fixed head gradient. Then the flow through this reference block is calculated. Because for this setup only the hydraulic conductivity is determining the flow, this flow can be used to calibrate the hydraulic conductivity of the 3D model to the hydraulic conductivity of the 3DHGM. Therefore, the same reference block with the same parameters and a uniform conduit network was created. Changing the conduit diameters of the network in the reference block of course changes the amount of flow through this block. By this *iterative* procedure the flow through the model is calibrated to the flow of the 3DHGM and consequently also to its hydraulic conductivity. The value found for the initial conduit diameter distribution is $\hat{d}_0 = 5 \times 10^{-5}\,\mathrm{m}$.

#### 4.2.1.2 Initial model

The initial model incorporates all previously mentioned standard domain properties and boundary conditions. The mode of the initial conduit diameter distribution and the maximum conduit diameter distribution is $\hat{d}_0 = 5 \times 10^{-5}\,\mathrm{m}$ (yellow curve in Fig. 4.5a) and $\hat{d}_{max} = 0.009\,\mathrm{m}$ (black curve in Fig. 4.5a), respectively. The

hydraulic conductivity of the matrix is set to $K_m = 1 \times 10^{-5}\,\mathrm{m\,s^{-1}}$. The head difference between up- and downstream part is $\Delta h = 7.3\,\mathrm{m}$. North, South and East boundaries are constant flow boundaries (N: $\ll 1\,\mathrm{ls^{-1}}$ out; S: $\ll 1\,\mathrm{ls^{-1}}$ in; E: $10\,\mathrm{ls^{-1}}$ in) as shown in Figs. 4.2a+b with red faces and arrows. The model run, as all other model runs for the present day scenario, is calculated for 110 years to cover the time between 1890 to 2000.

Fig. 4.3a shows the results for the initial model after 110 years of evolution. Plotted are the isosurfaces of constant head from dark (low head) to light grey (high head) and the increase of the conduit diameter compared to the initial conduit diameter $d/d_0$ on a log–scale. Dark blue colors represent no change $d/d_0 = 10^0 = 1$, red colors an increase by a factor of $d/d_0 \geq 10^3 = 1000$ or more. Furthermore, the current approximate extent of the WZ is plotted with a dotted line in all evolution plots. It is obvious that when plotting the final conduit network, it is not suitable to plot every single conduit. Especially in a 3D domain no information would be visible. Therefore, only conduits that have grown above a certain threshold are plotted. In Fig. 4.3 this threshold is $d/d_0 \geq 2$ as indicated by the color scale. It is pointed out here again that this threshold is used only for enhancing the visibility of the grown conduits. There are of course also active conduits that have increased by less than a factor of $d/d_0 = 2$. They are not shown in the plots as they would conceal the larger conduits which characterize the karstified WZ. Below Fig. 4.3a the anisotropy factor $F_a = 1$ is given. The anisotropy and the anisotropy factor $F_a$ are introduced and explained in 4.2.1.3. Here they are just given for completeness of Fig. 4.3. Actually, in the definition used here, an anisotropy factor of 1 means that there is effectively no anisotropy.

Fig. 4.3a shows that the conduit diameter distribution with the calibrated mode from the 3DHGM causes only little evolution. Just a few conduits close to the weir and horizontally along the river have significantly increased in diameter. But the enlarged (karstified) zone does not reach the extent of the real WZ. In a way this result is to be expected considering the drawbacks of the 3DHGM. As stated before the 3DHGM does not incorporate the temporal evolution of the aquifer. Because the 3DHGM is calibrated to the present–day state of the hydraulic heads in the observation wells, one would assume that the evolution should actually be much more pronounced in 3D karst evolution model. Obviously, this is not the case and therefore another approach has to be used to model the evolution of the Birs aquifer.

Nevertheless, the calibrated mode of the conduit diameter distribution will be used as a starting point for the following procedure.

#### 4.2.1.3 Initial model with anisotropy

To find an optimal initial conduit diameter distribution, the characteristic anisotropic properties of the Gipskeuper are now used. In the Gipskeuper sample in Fig. 4.2c a fracture between the gypsum and the marl layer which is $\approx 0.5$ mm wide can be seen and is marked with white arrows. It needs to be stated here that the sample shown in Fig. 4.2c is plotted in such a manner to illustrate the natural bedding of these layers. It is known from the field that the gypsum lenses are more or less horizontally oriented. Consequently, also fractures between gypsum and marl layers are horizontally oriented. To account for this geological characteristic, anisotropy information is introduced to the initial conduit diameter distribution. This is achieved by an anisotropy factor $F_a$. This factor $F_a$ scales all horizontal conduits (x– and y–direction) relative to the vertical conduits (z–direction) inside the model domain and makes them initially a little larger and therefore a little more conductive to horizontal flow. Consequently, this allows more aggressive solution to penetrate *horizontally* deeper into the bedrock.

Several arguments support this implementation of anisotropy. As mentioned before, the most obvious one is the rock sample in Fig. 4.2c with the horizontal fracture between the gypsum and the marl layer. Furthermore, the Birs weir location is tectonically characterized by the Eastern Rhinegraben Master fault and tectonic structures can be found in the immediate vicinity (Epting et al., 2009b). It is reasonable to assume that fissures grow along lithological, sedimentological and / or stratigraphical discontinuities as these are naturally weakened zones inside the bedrock. Therefore, the horizontal bedding of the sediments around the Birs weir provides a natural anisotropic fissure distribution inside the domain. It is also known from historical documents and investigations that the Birs river has been more or less in its current riverbed for more than 3000 years (Golder, 1984). It is not unlikely that the groundwater system changed periodically from effluent to influent conditions and by this triggered the evolution of small karstified zones or slight fissure enlargement close to the river (Romanov et al., 2012). Nevertheless, rather moderate values for $F_a$ were chosen.

Initially, at very early times, the flow regime is equal for all runs with or without

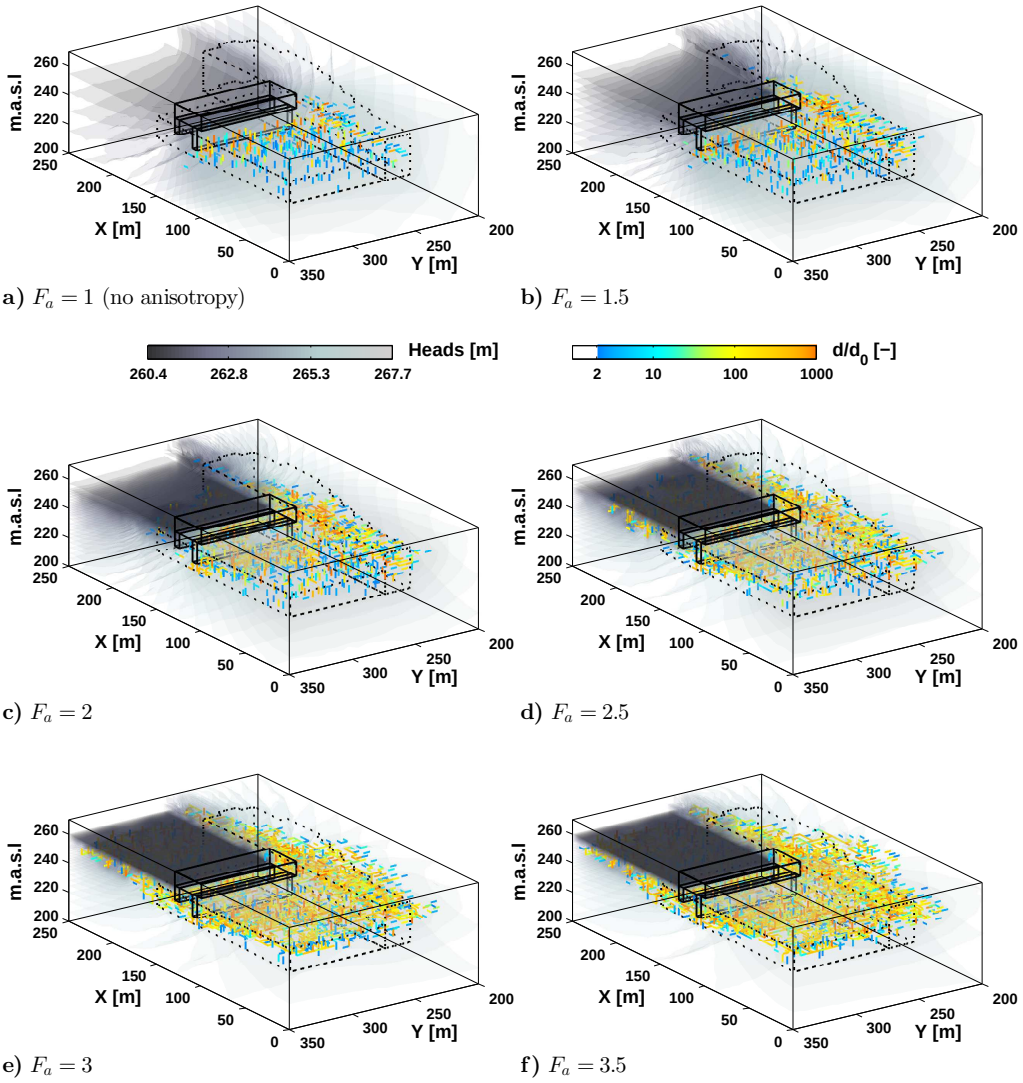


**a)** $F_a = 1$ (no anisotropy) **b)** $F_a = 1.5$

**c)** $F_a = 2$ **d)** $F_a = 2.5$

**e)** $F_a = 3$ **f)** $F_a = 3.5$

**Fig. 4.3:** Conduit network evolution for different anisotropy factors $F_a$; Below each subplot the anisotropy factor $F_a$ is given; Plotted are the isosurfaces of constant head from low (dark grey) to high (light grey) values and the relative increase of the conduit diameter compared to the initial diameter on a log–scale from 2 (blue) to $\geq 1000$ (orange).

anisotropy because of the dominating matrix conductivity. Only the impounded water in the upstream part of the river is determining the direction of flow, which is vertical into the quaternary riverbed and therefore perpendicular to the anisotropy. When the evolution sets in, the flow adapts according to the growing conduits (affected by the anisotropy) and the global hydraulic conductivity is becoming anisotropic which is thereby much closer to reality but by this also much more difficult to estimate.

Because the real anisotropy factor is of course not known, an *iterative* approach is used here. Different values of $F_a$ will be tested and the model that shows a karstified zone, that is in good agreement with the known extent of the real WZ will be chosen as the optimal model.

The effect of the anisotropy factor $F_a$ is shown in Fig. 4.3. From Fig. 4.3b to Fig. 4.3f the values for $F_a$ increase from 1.5 to 3.5. Because only the horizontal conduits are scaled the initial diameter distributions change from unimodal to bimodal. In Fig. 4.5a the different distributions are plotted. Whereas the distribution for a factor of $F_a = 1.5$ (blue curve) is still shaped unimodal with a mode of $d_0^{\hat{x}y} \approx 7.5 \times 10^{-5}\,\mathrm{m}$, the distribution for a factor of $F_a = 3.5$ (pink curve) is clearly bimodal with a mode for the horizontal conduits of $d_0^{\hat{x}y} \approx 1.8 \times 10^{-4}\,\mathrm{m}$. The anisotropy models in Figs. 4.3b–f have the same standard domain properties and boundary conditions as the initial model in Fig. 4.3a. Only the inflow from the East boundary is scaled to account for the increasing horizontal conduit diameters. Like for the initial model all subplots from Figs. 4.3b–f show the relative increase of the conduit diameters after 110 years of evolution.

For factors 1.5 (Fig. 4.3b) and 2 (Fig. 4.3c) the effect is rather small and larger conduits have only grown close to the weir. Both setups do not cover enough of the WZ in horizontal direction and also the increase inside the WZ is not too significant.

For factors 2.5 to 3.5 (Figs. 4.3d–f), the conduit evolution captures the whole WZ below the highway parallel to the river. In all three models the true maximum depth of the WZ (determined by observations) is reliably resolved. Increasing the factor $F_a$, more conduits grow towards the East, the North and below the upstream part of the river. Considering the resolution of the real WZ and especially the eastern boundary of the WZ, the model with an anisotropy factor of $F_a = 2.5$ (Fig. 4.3d) is chosen to be the optimal model. This model also shows sufficient features below the upstream part and close to the weir to support the geophysical ERT findings

(Epting et al., 2012).

Models with an anisotropy factor of $F_a = 3$ (Fig. 4.3e) and $F_a = 3.5$ (Fig. 4.3f) show a stronger evolution to the East but also to the North of the domain, especially below the downstream part of the river. This evolution is discussed later for the final model (see 4.2.1.5). The intention here, is so far only to show the general effect of anisotropy on the evolution of a WZ around the Birs weir. The choice of the model with $F_a = 2.5$ is a good trade–off between extent of the WZ, sufficiently large karst features below the highway and remaining gypsum content inside the WZ. The latter is shown and discussed when presenting the final model in 4.2.1.5 and the future model in 4.2.2.

It was shown that it is possible to implement the local rock anisotropy of the Gipskeuper around the Birs weir into the model. This is a major improvement over the 2D karst evolution models and allows for a much more realistic model setup. For the Birs weir model an anisotropy factor $F_a = 2.5$ was found which generates a WZ that is in a good agreement with field observations and the 3DHGM.

#### 4.2.1.4 Initial model with precipitation

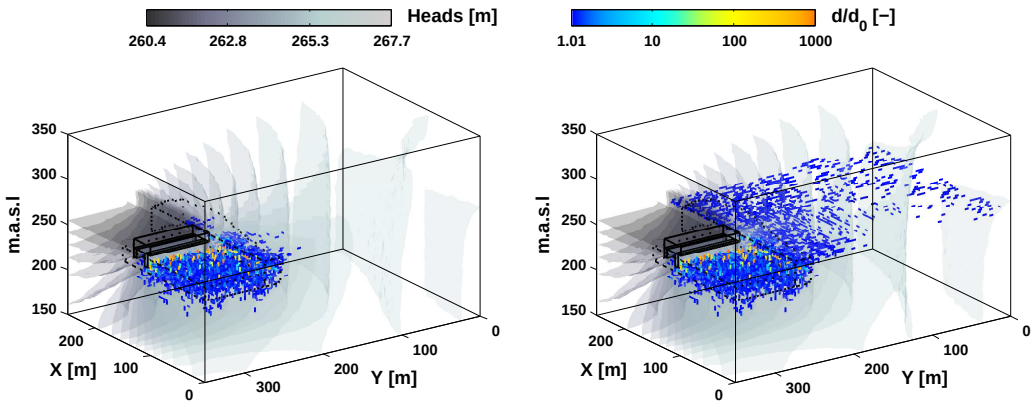


**a)** model without rainfall **b)** model with rainfall

**Fig. 4.4:** Conduit network evolution for a model without (a) and with (b) precipitation on the topography; Plotted are the isosurfaces of constant head from low (dark grey) to high (light grey) values and the relative increase of the conduit diameter compared to the initial diameter on a log–scale from 1.01 (blue) to $\geq 1000$ (orange).

Before discussing the final model, a short detour is made and another feature of

the 3D models is presented, the implementation of precipitation. For the presentation here, a model without anisotropy will be used.

In Fig. 4.4a the result for a model where the topographic boundary is deactivated (no rain) is shown. In Fig. 4.4b the same model is presented but with rain. Again the evolution after 110 years is shown. Note the different plot threshold indicated by the color scale in Fig. 4.4. Now all conduits that have at least grown by a factor of $d/d_0 = 1.01$ are plotted. Comparing Figs. 4.4a+b shows that if precipitation on the topographic boundary is activated, conduit enlargement is clearly visible along the water table. The evolution below the upstream part of the river in Fig. 4.4b is similar to the run without precipitation in Fig. 4.4a. This is due to the strong influence of the constant head boundary condition of the impounded river on this particular model. For the setup and time scale (only 110 years) used here, the effect of precipitation may be not that decisive for the evolution of karstified zone below the Birs weir, but it is nevertheless clearly visible along the water table.

From the engineering perspective it may be sufficient to note that the effect of the weir on the evolution of the weathered zone is much stronger than that of the rain. But only for the last 110 years after the construction of the weir. In fact, this result shows the potential for much more possible karst features further east from the river induced by the precipitation. Due to the inflow boundary condition the enlarged conduits in the east part of the domain grow towards the river. Because it can be assumed that the Birs river is in its current riverbed for $\approx 3000$ years (Epting et al., 2009b; Romanov et al., 2012) the aquifer has evolved under this quasi constant conditions until the weir was built. If the bedrock below the hill, east of the river also consists of soluble material it is not unlikely that one may find prominent karst features along or below the water table created by the natural karstification. This possible influence is so far not studied for the Birs weir location. To study this effect a 3D model with topography and precipitation as presented here in a rudimentary form is needed.

It is well known that in some karst regions precipitation is the major source of inflow to create karst features. Only with a 3D model it is possible to take into account the effect of the local topography on the evolution of a karst aquifer (hills, valleys, plateaus etc.) To include a topographic surface with realistic precipitation values together with the possibility to create complex model setups, are therefore necessary requirements for modelling real case scenarios in three dimensions.

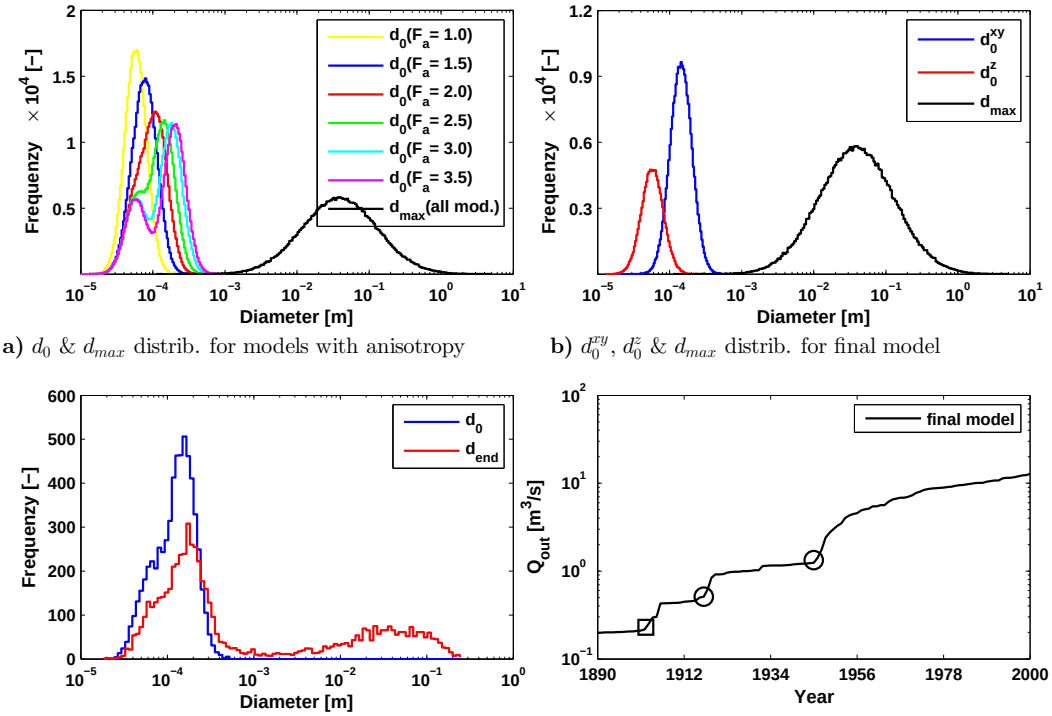


**a)** $d_0$ & $d_{max}$ distrib. for models with anisotropy

**b)** $d_0^{xy}$, $d_0^z$ & $d_{max}$ distrib. for final model

**c)** $d_0$ & $d_{end}$ distrib. for active conduits in final model

**d)** flow curve for final model

**Fig. 4.5: a)** Histograms of the initial conduit diameter distributions for the initial model (yellow) and models with varying anisotropy factor $F_a$ (blue to pink); the black line is the maximum conduit diameter distribution for all models; **b)** Histograms of the initial conduit diameter distributions for the final model; blue – horizontal conduits, red – vertical conduits, black – maximum conduit diameter distribution; **c)** Histograms of the initial (blue) and final (red) conduit diameter distributions for the final model; only active conduits are shown; **d)** flow curve of the final model showing the outflow in the downstream part of the river (see BC description); marked are local breakthrough events; square – probably due to initial connection caused by the statistical distribution; circles – horizontal and vertical breakthroughs due to dissolutional widening.

#### 4.2.1.5 Final model with anisotropy and precipitation

The final *optimal* model is now presented. It is only final in terms of marking the end of this modelling study for the Birs weir aquifer and is of course only one possible representation of reality.

For the final model an anisotropy factor of $F_a = 2.5$ for the conduit diameter distribution is chosen and rainfall is activated on the topographic boundary. The initial conduit diameter distributions are shown in Fig. 4.5b. The blue line represents all horizontal conduits, the red line all vertical conduits respectively. Both distributions are thinner and therefore more homogeneous than the distribution of the maximum diameters (black line). By this wider distribution of maximum diameters, karst features are allowed to develop that can be up to the meter scale.

The boundary conditions are the following: For the East inflow boundary the calibrated value from the 3DHGM of 10 $\mathrm{l\,s^{-1}}$ (Epting et al., 2009b) is used. The North and South flow boundaries are as described in 4.1.3 as well as the rainfall and the constant head boundary for the river. The evolution of the final model is shown in Fig. 4.6 and Fig. 4.7. Because it is very difficult to show all information in one plot, the presentation of the results is split into two figures. In Fig. 4.6 the head distribution and the relative increase of conduit diameters is shown like in the figures before. In Fig. 4.7 the calcium concentration and the calcium flux rate for the same snapshots in time as in Fig. 4.6 are shown. For Figs. 4.7b–f slices marked with A, B and C are used to show the calcium concentration instead of isosurfaces. This is done for a better visibility as it is sufficient enough to show the calcium concentration along these cut–out planes or slices.

The initial situation at 1890 is shown in Figs. 4.6a and 4.7a for the whole modelling domain. The isosurfaces of constant head in Fig. 4.6a are almost symmetrically distributed around the Birs weir and only show slight inner–surface distortions due the statistical conduit network. The calcium concentration in Fig. 4.7a is zero inside the river because of the boundary condition there and reaches equilibrium already very close to the river. For all other snapshots in time from Figs. 4.6b and 4.7b to Figs. 4.6f and 4.7f, it is closer zoomed into the domain to focus on the changes around the weir and within the WZ.

In Figs. 4.6b and 4.7b the evolution after 10 years is shown. From the flow curve in Fig. 4.5d one can see that at ≈1900 a first local breakthrough event occurred (indicated by the jump in the flow curve). When looking on Fig. 4.6b only a few

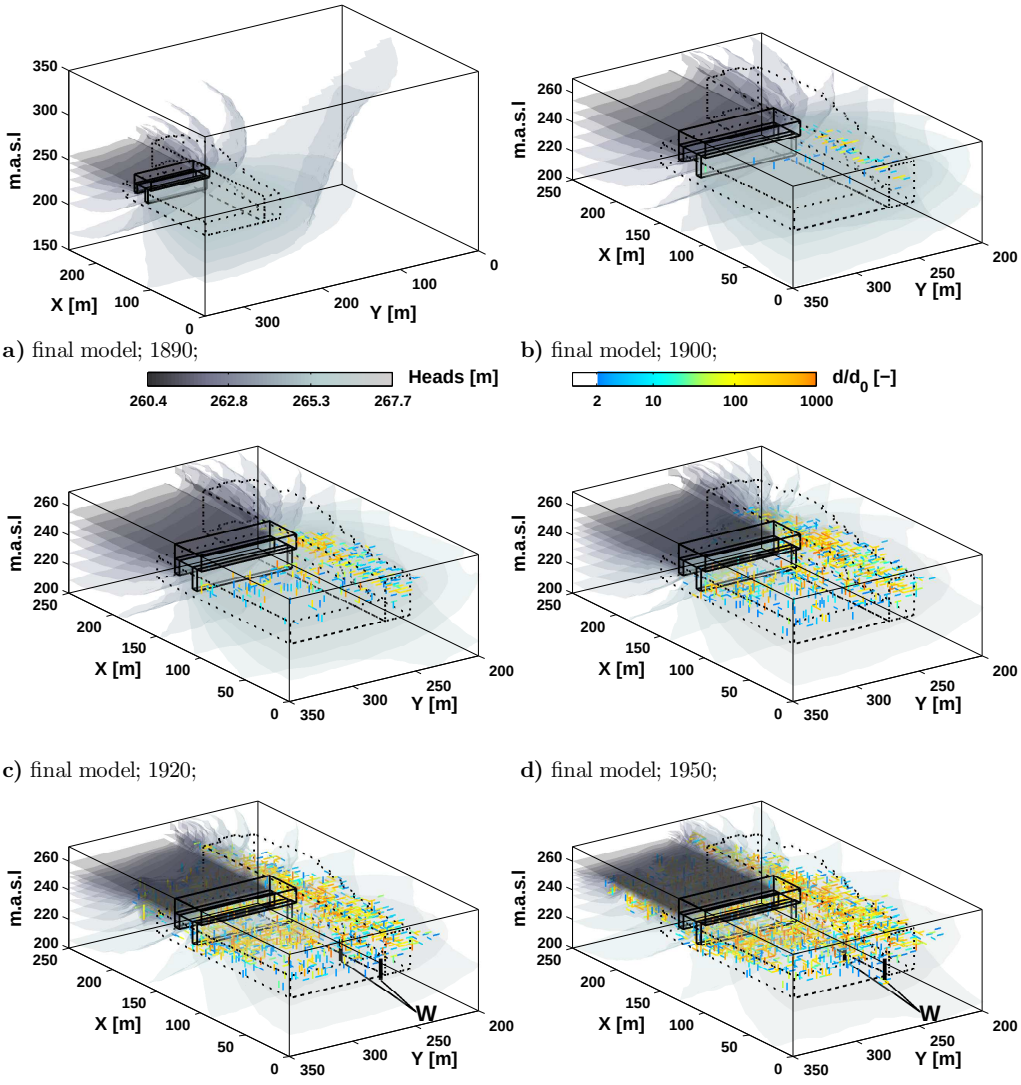


**a)** final model; 1890;

**b)** final model; 1900;

**c)** final model; 1920;

**d)** final model; 1950;

**e)** final model; 1980; with wells W

**f)** final model; 2000; with wells W

**Fig. 4.6:** Conduit network evolution for the final model for different snapshots in time; Below each subplot the year is given; Subplots b to f are zoomed in for better visibility; Plotted are the isosurfaces of constant head from low (dark grey) to high (light grey) values and the relative increase of the conduit diameter compared to the initial diameter on a log–scale from 2 (blue) to $\geq 1000$ (orange); In subplots e and f the location of two wells is indicated by thick black lines marked with **W**.

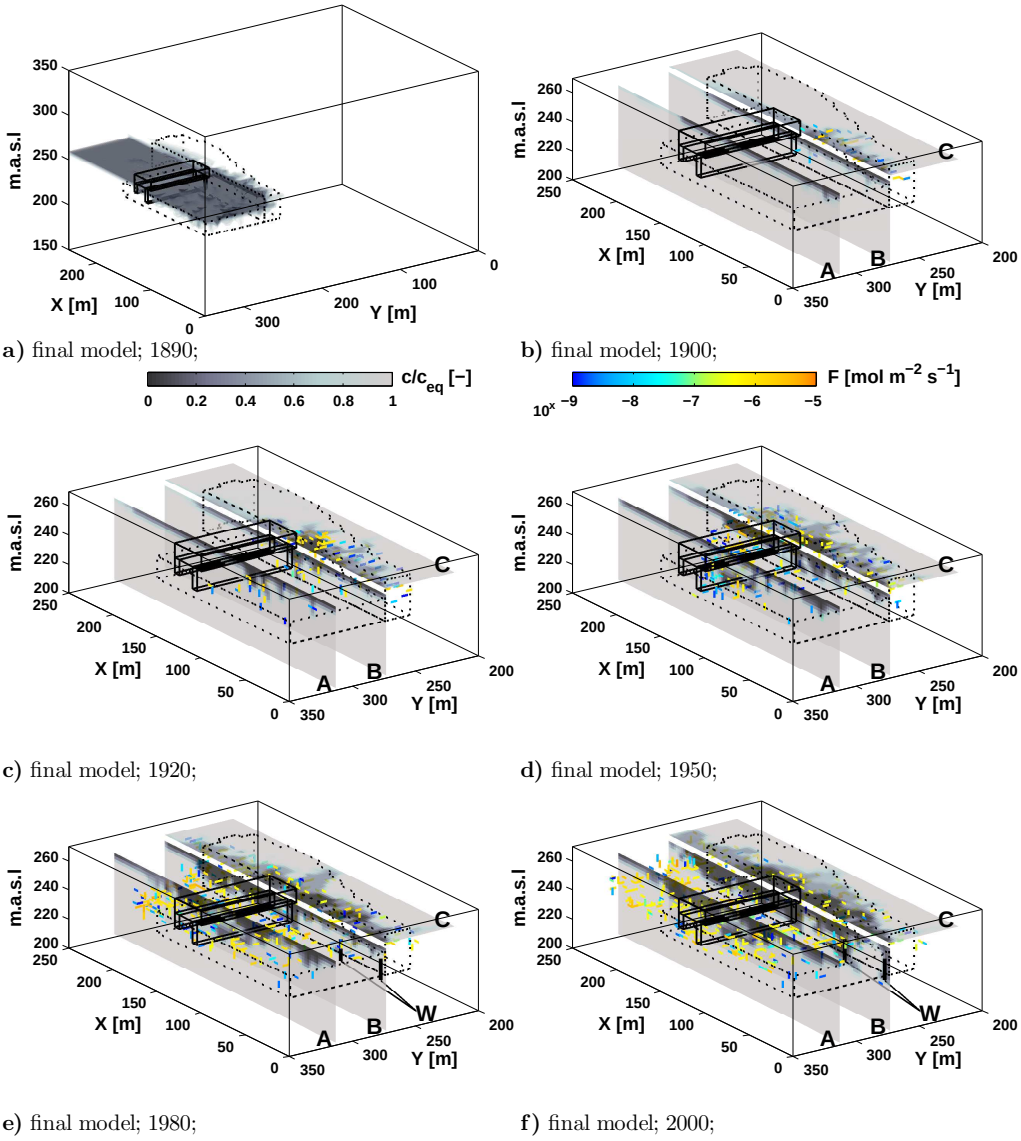


**a)** final model; 1890;

**b)** final model; 1900;

**c)** final model; 1920;

**d)** final model; 1950;

**e)** final model; 1980;

**f)** final model; 2000;

**Fig. 4.7:** Calcium concentration and flux rates for the final model for different snapshots in time; Below each subplot the year is given; Subplots b to f are zoomed in and show slices A, B, C of Calcium concentration instead of isosurfaces for better visibility; Plotted are the Calcium concentration from $c = 0c_{eq}$ (dark grey) to $c = c_{eq}$ (light grey) and the flux rates inside the conduit on a log–scale from $10^{-9}[\mathrm{mol\,m^{-2}\,s^{-1}}]$ (blue) to $10^{-5}[\mathrm{mol\,m^{-2}\,s^{-1}}]$ (orange); In subplots e and f the location of two wells is indicated by thick black lines marked with **W**.

conduits have grown horizontally and close to the weir. One gets a similar picture when looking at slices B+C in Fig. 4.7b. The calcium concentration and the flux rate also indicate that the evolution has just started horizontally along the river. But there is also a visible connection between the upstream and the downstream part of the river horizontally along the weir, indicated by low flux rates. It is possible that the statistical distribution of the initial conduit diameters has created a small pathway of connected conduits which can already capture enough flow to be regarded as a small breakthrough event. Therefore it is marked with a square in Fig. 4.5d to distinguish it from the two other *evolutional* events occurring later in time.

The next breakthrough event in the model is at ≈1920 (see Fig. 4.5d). In Fig. 4.6c a clearly visible horizontal pathway has established horizontally around the weir. One can see that the conduits creating this pathway have at least grown by a factor of $d/d_0 = 50$ and the hydraulic head gradients increased close to the weir. This pathway allows for more aggressive water to enter the bedrock (Fig. 4.7c slice C) and creates therefore the preferential pathway. But there is a significant difference in the breakthrough behaviour of this model and the dam–site models presented in 3. There, the models always used the *standard* unlimited widening scheme, implying that a conduit or fracture can grow up to a maximum diameter or aperture width defined only by the grid discretization. With this implementation it was assured that always enough soluble material was present to be dissolved and therefore the diameters and flow rates could constantly increase. These models were especially distinguished by the strong increase in flow rates indicating the breakthrough event (see e.g. the flow curves in 3.2.2). As already mentioned in 4.1.2, here for this setup, the limited widening approach presented by Romanov et al. (2010) is used. The artificial limiting of conduit diameters to a maximum value and therewith preventing the typical strong increase in flow rates causes the small *jumps* in the flow curve in Fig. 4.5d. So these small jumps can in a way be regarded as local breakthrough events.

The third breakthrough event visible in Fig. 4.5d occurs around 1950. Whereas the flow continuously increases between 1920 and 1945 due to the ongoing karstification horizontally around the weir, around 1950 also a vertical pathway has established. This can be seen by the increased conduits in Fig. 4.6d in the center of the river below the weir connecting the upstream and the downstream part. This connection is also visible in the calcium concentration slice A in Fig. 4.7d. The

dark colors show the low calcium concentration of the aggressive water flowing along this path. Ongoing from 1950 these two major pathways continuously develop and increase the permeability of the bedrock around and underneath the Birs weir.

With this final model we also want to study another interesting effect revealed by the field observations: Several karst features like large conduits and cavities have been found along the bottom of the WZ during the drilling campaign, which took place before and during the construction measures to stabilize and support the highway (Fig. 4.1d and/or Epting et al. (2009a)). It is assumed that several boreholes drilled in the 1980's have possibly established a shortcut between shallower and deeper layers of the Gipskeuper. To test the influence of these boreholes two wells are implemented on the eastern bank of the river. Their locations are taken from Epting et al. (2009a) and they are put to the model for the year 1980 (Figs. 4.6e and 4.7e). The wells are established by setting the constant head value from the river also at the nodes at the end of the wells. With these two artificially created wells it is tested if the model can represent some of the found features. The location of the wells is shown in Figs. 4.6e+f and 4.7e+f as thick black lines marked with **W**. When comparing the two snapshots in time in Figs. 4.6e+f and 4.7e+f, respectively, the effect of the wells becomes visible. Slice B in Fig. 4.7f shows that aggressive water is carried through the wells towards the bottom of the WZ and conduits close to the wells start enlarging due to the *injected* aggressive water. By taking into account the effect of such artificial shortcuts in the Gipskeuper, it can be shown that within just 20 years (1980-2000), the potential of these artificially created pathways on the gypsum karst evolution can be significant.

The results for the year 2000 of the final model are plotted in Figs. 4.6f and 4.7f. In addition, the initial and final conduit diameter distributions for all active conduits are plotted in Fig. 4.5c. The $d_{end}$ distribution (red curve) shows the evolution of conduit diameters and therefore the increase in conductivity over almost three orders of magnitude. The biggest conduits are up to 0.2 m.

Fig. 4.6f shows how the evolved conduits capture the WZ, especially below the upstream part of the river and horizontally below the highway. As mentioned earlier when discussing the implementation of anisotropy, there is also a karstified zone below the downstream part of the river. Because there are no field observations in this part of the river this finding of the model can so far not be verified. It needs to be emphasized here that the model runs may overestimate the total amount

of available gypsum in parts of the domain. Therefore, the results shown in the downstream part just indicate the potential for karst features. The model setup assumes Gipskeuper inside the whole domain and the geology is implemented by the distribution of soluble conduits only. From field observations further downstream (outside of the model domain) it is known that the geology there is quite complex and heterogeneous and shows changes from Gipskeuper to Schilfsandstein. Therefore, it is possible that there is much less karstified Gipskeuper further downstream than directly close to the weir.

The plausibility of the model is also supported by the distribution of calcium concentration inside the WZ (Fig. 4.7f). This plot shows that the calcium concentration is around $c \approx 0.4 c_{eq}$ inside the WZ, which is in good agreement with the chemical analysis of the subsurface water samples (Epting et al., 2009b). The flux rates in Fig. 4.7f also show that the karstification is still active especially below the river. The reader may notice that Figs. 4.6f and 4.3d are almost identical in terms of conduit evolution. This is of course expected as both runs have similar initial conduit diameter distributions and only differ in the Eastern flow boundary. But what this actually also shows is that for the creation of the WZ the effect of the weir is of much greater importance than the effect of the flow boundaries, especially the Eastern inflow boundary. Several test runs with different Eastern inflow values and even a no flow boundary were additionally calculated. The shape of the created karstified zone was almost identical in all cases. This underlines the importance of the anisotropy and the limited conduit widening for the Birs weir scenario.

The presented 3D model shows a reasonable evolution of the Birs weir aquifer. It pursued the findings of the 3D hydrogeological model (Epting et al., 2009b) and extends the 2D karst evolution models (Romanov et al., 2010, 2012) into the third dimension. By this it essentially helped to understand the complicated hydrology around the Birs weir.

### 4.2.2 Future

Now the temporal evolution of the Birs aquifer after the year 2000 is discussed, thus when construction of the grout curtain (sealing pile wall) has been conducted. Note that for simplicity and continuity reasons the construction measures are assigned to the year 2000 within this model study, whereas they have been carried out between 2006 and 2007 (Epting et al., 2009a).

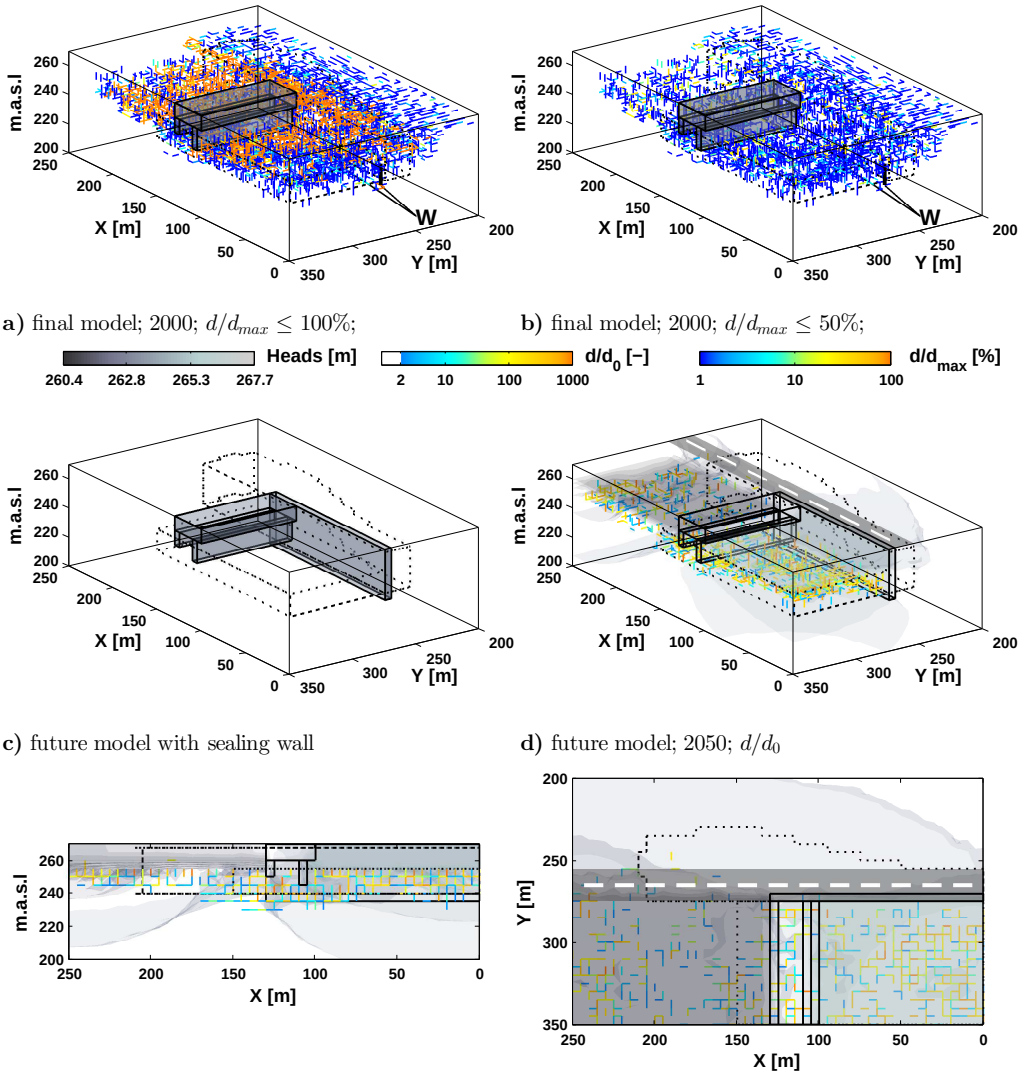


**a)** final model; 2000; $d/d_{max} \leq 100\%$;

**b)** final model; 2000; $d/d_{max} \leq 50\%$;

**c)** future model with sealing wall

**d)** future model; 2050; $d/d_0$

**e)** future model; 2050; $d/d_0$; front view

**f)** future model; 2050; $d/d_0$; top view

**Fig. 4.8: a+b)** Conduit network evolution for the final model; In subplots a and b the final diameter $d$ compared to the maximum diameter $d_{max}$ in [%] is plotted on a log–scale for all active conduits (at least grown by a factor of $d/d_0 \geq 1.1$); Plotting threshold $d/d_{max}$ in **a** is $\leq 100\%$ in **b** $\leq 50\%$; **c)** Implementation of sealing pile wall to the future model; **d** Final head distribution and conduit network after 50 years of evolution; **e)** front view of **d**; **f)** top view of **d**; Plotted are the isosurfaces of constant head from low (dark grey) to high (light grey) values and the relative increase of the conduit diameter compared to the diameter $d_0$ (at the year 2000) on a log–scale from 2 (blue) to $\geq 1000$ (orange).

It was already shown in Fig. 4.7f, that the calcium concentration in the WZ is around $c \approx 0.4 c_{eq}$ in the year 2000. This fact becomes interesting when looking on Figs. 4.8a+b: These two plots show for the year 2000, how close the active conduits (the ones at least grown by a factor of $d/d_0 \geq 1.1$) are to their maximum diameter allowed by the Gipskeuper layer thickness. Fig. 4.8a shows the percentage of all active conduits while in Fig. 4.8b a threshold of 50% is used (only active conduits that have grown up to 50% of its maximum diameter). Particularly the conduits close to the bottom of the river and below the highway have reached already their maximum. But there are still enough conduits in the deeper layers and in the East part of the WZ that can evolve. This is also in good agreement with the field observations as they have shown that the gypsum is not yet completely removed from the WZ (see 4.1.1). As indicated in 4.2.1.3, when using anisotropy factors of $F_a = 3$ or $F_a = 3.5$ too many conduits would have reached their maximum diameter in the year 2000 and there would not be enough soluble gypsum to comply with the field observations.

Fig. 4.8c shows the implementation of the grout curtain or the sealing pile wall respectively. It is achieved by adding an insoluble and impermeable layer vertically along the eastern bank of the upstream river. The sealing wall is vertically extended into the non–weathered bedrock to block any flow from the WZ towards East. The initial distribution of conduit diameters is taken from the final time step (year 2000) from the final model of the above section.

In Fig. 4.8d, the head distribution and the evolved conduits are shown after 50 years of evolution. Note that the relative increase of the conduit diameters is calculated by the initial conduit diameter distribution of the future model (year 2000) and not the final model (year 1890). Figs. 4.8e+f show the same picture as Fig. 4.8d in a front and top view respectively. The active conduits in the lower part of the WZ continued to evolve along the whole river as expected from Figs. 4.8a+b. In this idealized setup the sealing wall effectively prevents any further karstification below the highway close to the weir (Fig. 4.8f).

This future model shows that the highway may be protected by the sealing pile wall. But because of the active parts in deeper layers of the WZ the karstification continues below the weir. If the fact is considered that the whole weir structure is already tilted due to karstification processes below the structure (see Fig. 4.1c and Epting et al. (2009a)), it may be necessary to carry out more construction measures

to further stabilize it.

## 4.3 Conclusions

In this chapter a realistic 3D karst evolution model for the Gipskeuper aquifer of the Birs weir at the river Birs close to the city of Basel in Switzerland was presented. Here, in the 1980's a nearby highway as well as the weir itself showed strong subsidence and even the formation of sinkholes. These karst–related hazards raised the need for extensive investigation and construction measures, such as observation boreholes, geophysical measurements, 3D hydrogeological modelling, 2D karst evolution modelling, and finally the construction of a grout curtain. The results from these investigations identified the reason for the subsidence: a weathered zone of karstified Gipskeuper along the river below the highway.

The intensive monitoring and modelling results provided the boundary conditions for the 3D model setup presented here. According to the current knowledge, this is the first time that the evolution of a karst aquifer beneath a real dam–site is modelled in three dimensions. The implementation of the local Gipskeuper bedrock properties in terms of available gypsum and anisotropy was presented here. Furthermore, a topographic boundary with precipitation values based on field data was used. It could be shown that the anisotropy of the local bedrock had a decisive effect on the evolution of the Birs weir aquifer, whereas the effect of the rainfall is not so strong for the considered time scale. The use of precipitation and a realistic 3D topography revealed the potential for further karstified regions east of the Birs river. The basic scenario presented here can easily adopted for more complex setups.

The final *optimal* model was not only able to describe the evolution of the Birs weir aquifer over the last 110 years, it also could reproduce the weathered zone in terms of horizontal and vertical extent. Additionally, also the residual calcium concentration distribution is in good agreement with the chemical analysis of the aquifer water. The model showed a karstified zone below the river along the whole domain. The developed zone below the upstream part can be supported by underwater ERT measurements (Epting et al., 2012). For the downstream part, so far no such field data is available.

Also a prediction on the possible evolution of the aquifer after the construction of a sealing pile wall to support the highway was made. It was shown that under the

assumption that the sealing wall is impermeable and reaches deep enough into the non–weathered bedrock, it effectively prevents aggressive water to enter the bedrock horizontally below the highway. By this it suppresses further karstification below the highway. In agreement with the field observation that even in the weathered zone $\approx 15\%$ of the gypsum in the Gipskeuper is still available, the model showed that the potential for further karstification in deeper layers of the weathered zone is still present, and this might represent a future risk.

Of course the presented future scenario is only one of many possible realizations, therefore it is important to continue to observe the Birs aquifer and its vicinity carefully with a wide range of hydrogeological, geotechnical and geophysical methods. The 3D karst evolution model presented here can only give a rough idea (in terms of a future outlook) of the potential risks that may threaten the Birs weir structure.

Finally, this chapter has shown, that based on the conceptual models in the previous chapter, it is possible to create complex 3D karst evolution models. These models can be integrated into a wide range of available applied methods to study highly heterogeneous karstification processes close to man–made structures.

Chapter 5

# On the genesis of large collapse dolines: A 3D modelling approach

After in the previous chapter a practical application of karst evolution modeling was presented, the focus is now shifted to the investigation of one of the most impressive and significant surface karst features — large collapse dolines.

A doline is along with poljes and uvalas one of the characteristic karst depressions in the Dinaric karst (Kranjc, 2006). Like many terms used in karst science also the term doline has its roots in the Slavic language and originates from the words *dol* (down) and *dolina* (valley). The size and shape of dolines is as manifold as their origin and ranges from a few meters to hundreds of meters both in diameter and depth. Fig. 5.1 shows six major types of dolines after Waltham et al. (2005) which may occur in nature as a pure form or as a combination of them depending on the local geology. Here, the focus is put to large collapse dolines which are characterized by steep walls or cliffs, debris and breakdown material on the bottom and a cave or passage on the bottom or below the ground level. Generally, the topographic location of a collapse doline relates to underground water flow or more precisely a large underground river (Kranjc, 2006).

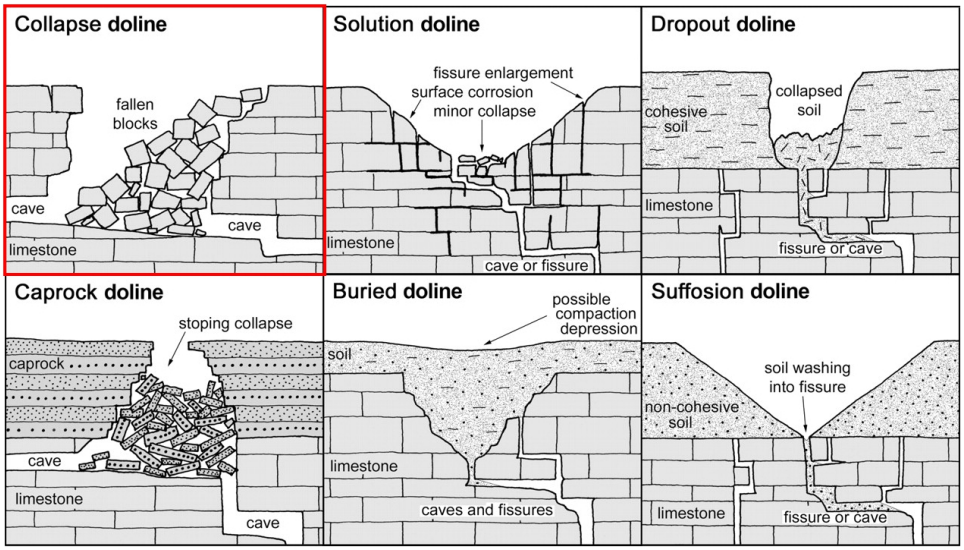


**Fig. 5.1:** The six different doline types, modified after Waltham et al. (2005).

A special subtype of very large collapse dolines are *Tiankengs* (heavenly pits) that can be found in the karst regions of China. In terms of genesis a Tiankeng is similar to a collapse doline but has become its own characteristic term in karst

science (Zhu and Waltham, 2006). The major distinction is made by its size because a Tiankeng has to be at least 100 m deep and wide. Fig. 5.2 shows four examples of large collapse dolines and Tiankengs respectively.

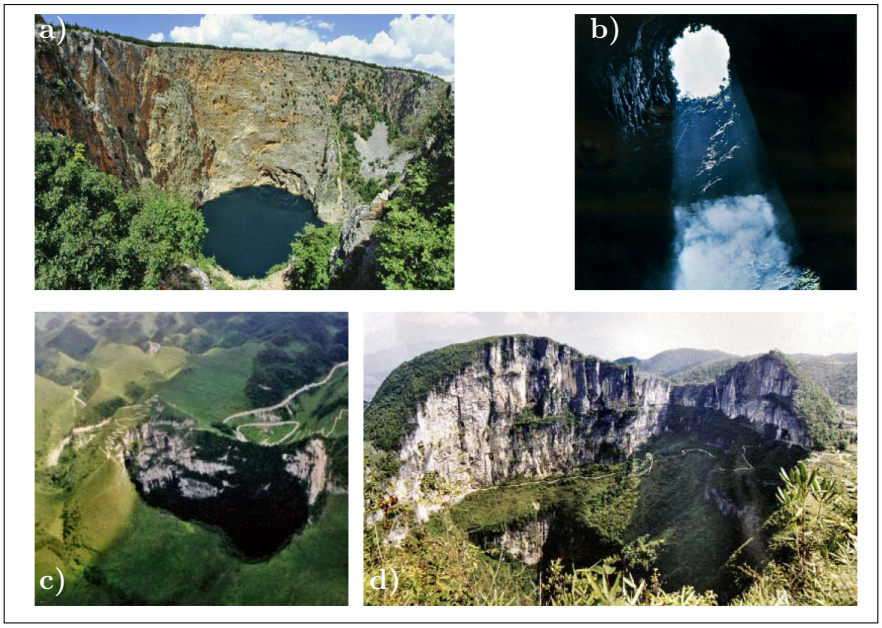


**Fig. 5.2:** Large collapse doline examples; **a)** *Crveno Jezero* (Red Lake) doline, Croatia from (Kranjc, 2006); **b)** *Sótano de las Golondrinas* (Cave of Swallows), Mexico from (Raines, 1967); **c)** *Dashiwei* Tiankeng, China; **d)** *Xiaozhai* Tiankeng, China, **c+d** from (Zhu and Chen, 2006).

Fig. 5.2a shows the collapse doline *Crveno Jezero* (Red Lake) in Croatia. It is 528 m deep and is filled with water up to 287 m. Large cave entrances have been found on the floor that allow water to flow through the doline. It's upper rim is $\approx 450\,\text{m} \times 400\,\text{m}$ and its volume is estimated between $25 \times 10^6\,\text{m}^3$ and $30 \times 10^6\,\text{m}^3$ (Kranjc, 2006). Fig. 5.2b shows *Sótano de las Golondrinas* (Cave of Swallows) a doline in the karst mountains of Sierra Madre Oriental, Mexico. It is considered to be an immature Tiankeng because of its overhanging walls that have not collapsed yet (Waltham, 2006; Zhu and Waltham, 2006). The surface opening is only $65\,\text{m} \times 50\,\text{m}$ whereas its floor dimensions are $130\,\text{m} \times 250\,\text{m}$. The depth is $\approx 400\,\text{m}$ with fissures ranging down to 512 m indicating a large amount of breakdown debris. Its volume is estimated with $\approx 5 \times 10^6\,\text{m}^3$. Unlike for other large collapse dolines there is no knowledge of a subsurface river or cave system so far (Waltham, 2006). Figs. 5.2c+d

show two typical Chinese Tiankengs, *Dashiwei* (c) and *Xiaozhai* (d), respectively. The Dashiwei Tiankeng is the largest Tiankeng in the Dashiwei group located in the Leye karst (Guangxi province). It is 600 m long and 420 m wide and its maximum depth is 613 m giving a total volume of $\approx 75 \times 10^6$ m$^3$. Its floor is covered by 100 m thick debris which itself is covered by a secondary forest. The cave river can be entered at the lowest point of the Tiankeng (Zhu and Chen, 2006). The largest Tiankeng discovered so far is the Xiaozhai Tiankeng near the city of Xinlong (Fengje county) with a diameter ranging from 537m to 626m and a maximum depth of 662m. It has a double nested structure with a plateau in 320 m depth and a total volume of $\approx 120 \times 10^6$ m$^3$. Across the floor of Xiaozhai the cave river has a maximum discharge of 175 m$^3$ s$^{-1}$ making it a strong source of erosion and material removal (Zhu and Chen, 2006).

These four examples are only a small portion of the known and discovered large collapse dolines of the world. A general overview can be found in Waltham et al. (2005) also with a focus on practical implications close to collapse features in karst. Kranjc (2006) gives an overview on large collapse dolines in the Dinaric karst whereas Waltham (2006) concentrates on large collapse dolines and / or Tiankengs throughout the world. Zhu and Chen (2006); Zhu and Waltham (2006) focus on Tiankengs especially in China. Summarizing the given references, there are a few characteristics typical for large collapse dolines. A large collapse doline is typically a few tens to a few hundreds of meters wide and deep. The walls are very steep or close to vertical and the floor of the doline can be covered with breakdown debris but don't necessarily has to. A large river is either flowing on the floor of the doline or below the ground but not too deep (tens of meters). Collapse dolines can appear in groups all belonging to the same active subsurface cave system (e.g the Dashiwei group or the dolines of the slovenian Škojcanske jama). The age of some Dinaric collapse dolines is assumed to be in the range of millions of years (Gabrovšek, 2011 – personal communication) whereas for Tiankengs less than 200 000 years are suggested (Zhu and Chen, 2006; Zhu and Waltham, 2006).

Small dolines can be created by a subsidence event or collapse of a cave ceiling. On the contrary the processes for the generation of large collapse dolines has to be more complex as large collapse dolines are generally two orders of magnitude bigger than the largest known cave chambers (Gabrovšek and Stepišnik, 2011). An explanation of the creation of large collapse dolines has been given by Palmer and Palmer

(2006). There, the authors suggested that the hydraulic processes in a collapse or crushing zone is responsible for the creation of large collapse dolines. Collapsing material blocks a subsurface river, increases therewith the hydraulic gradients and consequently increases the dissolution / flux rates and erosional forces. This concept was adapted by Gabrovšek and Stepišnik (2011) with a 2D karst evolution model to estimate the material removal in such a crushed zone. This approach is now taken one step further into the third dimension.

First, the 2D setup of the crushed zone from Gabrovšek and Stepišnik (2011) is rebuilt with the 3D program KARSTAQUIFER to compare the evolution of both models and to find a comparable basis. Then the model is extended into 3D and the crushed zone is embedded into a 3D domain. The evolution of the models is mainly investigated in terms of material removal. As so far erosional forces are not implemented into KARSTAQUIFER the creation of the collapse doline in terms of surface lowering is simulated by a collapsing mechanism. The major part of this chapter is to study the interaction of several spatially distributed crushed zones within one domain. Because in nature large collapse dolines often appear in groups, the investigation and understanding of their interaction (if any) is of high interest to the scientific community. To study these interactions, first the evolution of a single crushed zone is considered and then the amount of activated crushed zones is successively increased.

The essential findings of this chapter have been presented in Hiller et al. (2012a).

## 5.1 The model setup

The conceptual model of a collapse doline is shown in Fig. 5.3. **A** is the karst bedrock in which the collapse doline **B** is going to evolve. One of the necessities to create a collapse doline are fault zones inside the bedrock which somehow mark the *boundaries* of a mechanically unstable crushed zone. These fault planes are indicated by the dashed lines in Fig. 5.3. Another necessity in the presented concept is a subsurface passage or stream were water can enter (**D1**) and leave (**D2**) the domain. As this passage crosses the faulty bedrock it is intercepted and blocked by collapsed material inside the crushed zone **C**. Due to the crushed zone, the hydraulic gradient increases and allows for the creation of alternating widened channels through this highly fissured part of the domain. Then the dissolved material is transported out

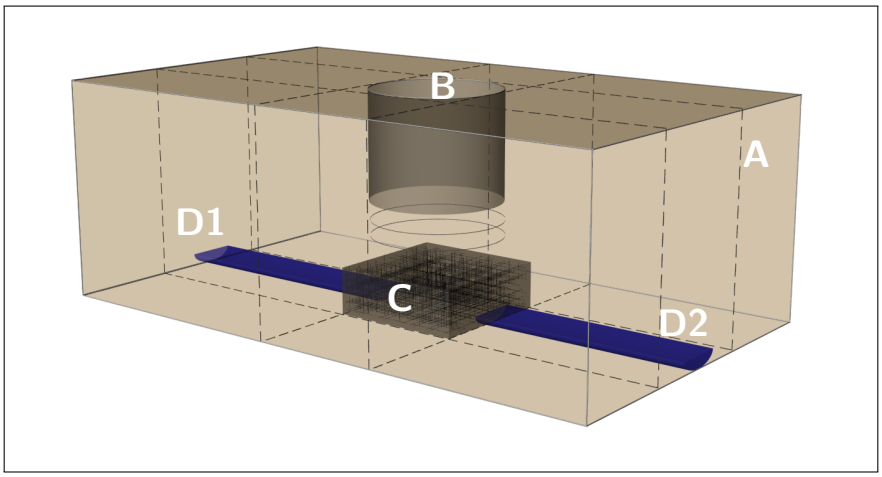


**Fig. 5.3:** Conceptual model of the doline model; **A** karst bedrock; **B** collapse doline; **C** crushed zone; **D1** subsurface passage / stream (input); **D2** subsurface passage / stream (output); the dashed lines represent fault planes inside the bedrock; modified after Gabrovšek and Stepišnik (2011).

of the crushed zone through the output passage. Because the crushed zone is a mechanically unstable zone the removal of the bedrock induces a lowering of the surface and therefore the creation of a collapse doline. This lowering is indicated by the thin lines below the doline *cylinder* in Fig. 5.3. Note, that in this approach the bedrock is only removed by dissolution so far. It does not account for the real mechanical properties of the bedrock as well as erosion processes that might remove collapsed material from the bottom of the crushed zone. The lowering of the surface is approximated with KARSTAQUIFER and explained later in more detail (see 5.2.4).

Because the model domain changes during this model study, the domain properties are explained in the corresponding sections.

## 5.2 Prerequisites

### 5.2.1 2D Model calibration

As this doline model is inspired by Gabrovšek and Stepišnik (2011) and is consequently a 3D expansion of their 2D approach, the first objective is to compare the 2D results with the 3D program used here. First, only the crushed zone itself is

considered, later this crushed zone is embedded into a 3D domain.

#### 5.2.1.1 Model domain and boundary conditions

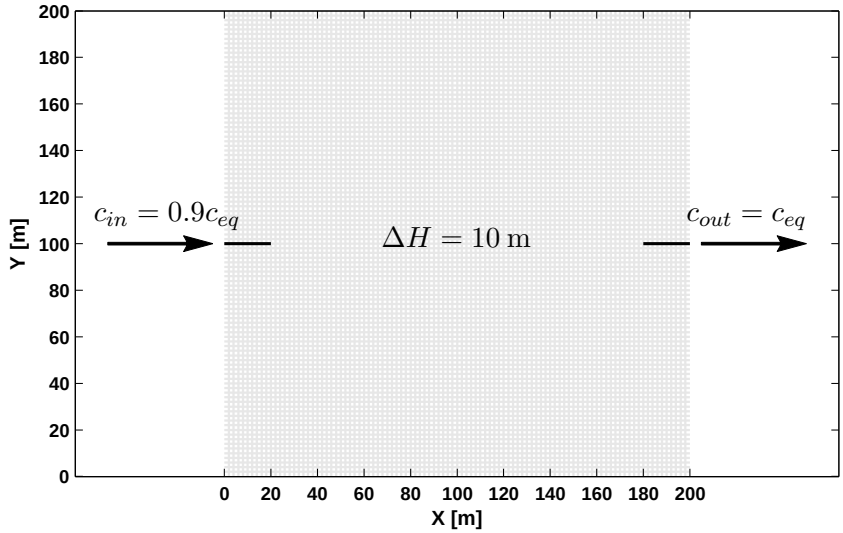


**Fig. 5.4:** Model domain and boundary condition of the calibration models; water enters the crushed zone from the left through the channel / passage with a calcium concentration of $c_{in} = 0.9c_{eq}$ and leaves the domain at the right side; the hydraulic head difference is $\Delta H = 10\,\mathrm{m}$; the conduit network is indicated by thin grey lines.

Gabrovšek and Stepišnik (2011) used a 2D fracture network with a size of $200 \times 200\,\mathrm{m}^2$ to simulate the evolution inside the crushed zone. The fracture spacing was 2 m and their height was 1 m respectively. They applied a dual fracture network which means that a dense network of 2 m long fractures is superimposed by a sparse randomly distributed network of 20 m long fractures. The fractures in the dense network have aperture widths ranging from 0.1mm to 0.4mm whereas the fractures in the coarser network have aperture widths ranging from 0.4mm to 0.8mm respectively. The water enters through a channel on one side of this crushed zone and leaves on the opposite side respectively. The head difference is $\Delta H = 10\,\mathrm{m}$ and the input concentration of the water is $c_{in} = 0.9c_{eq}$.

This setup is rebuild with KARSTAQUIFER in terms of geometry and boundary conditions as shown in Fig.5.4. There, a top view of the model domain is shown which has only one element (two nodes) in z–direction. Out of this one–element layer, only the lower of the two conduit layers is activated to get an almost perfect

2D setup. The objective of the calibration is to get a comparable evolution behaviour for the 2D and the 3D code and to find therewith the initial diameter distribution for this study. Therefore, only the breakthrough time $T_B$ will be considered as the flow rates will obviously be different due to the different implementation of the network (fractures in the 2D model – conduits in the 3D model). To mimic the dual fracture network of the 2D approach conduit diameter distributions with different statistical parameters will be used.

#### 5.2.1.2 Calibration results

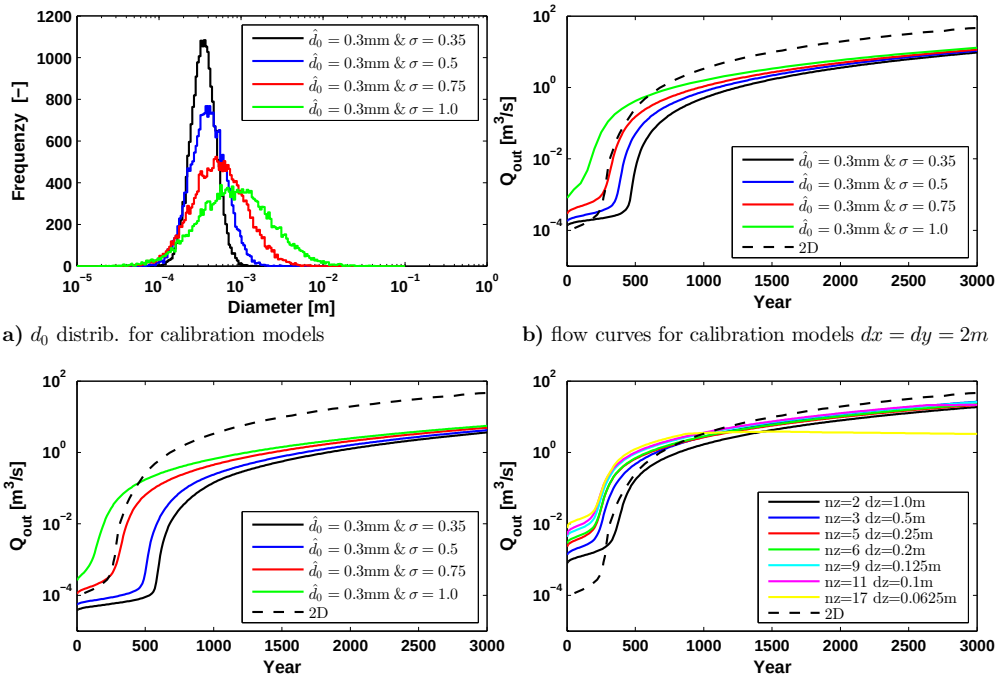


**a)** $d_0$ distrib. for calibration models

**b)** flow curves for calibration models $dx = dy = 2m$

**c)** flow curves for calibration models $dx = dy = 5m$

**d)** flow curves for 3D calibration models

**Fig. 5.5:** Doline model calibration; **a)** initial diameter distributions for different models to calibrate the 3D code to the 2D model; **b)** corresponding flow curves to **a** plus the 2D flow curve; **c)** flow curves for calibration models with a coarser network ($dx = dy = 5$ m); **d)** flow curves for the *extended* 3D calibration models.

Fig. 5.5a shows a set of the tested conduit diameter distributions. All distributions have a mode of $\hat{d}_0 = 0.3$ mm and a varying standard deviation $\sigma$. The wider the distribution gets the more non–uniform the conduit network will be. For

$\sigma = 0.35$ (black curve) the distribution spans about one order of magnitude, whereas for $\sigma = 1$ (green curve) it spans four orders of magnitude respectively. In Fig. 5.5b the corresponding flow curves are plotted for 3000 years of evolution together with the 2D flow curve (dashed black curve) from Gabrovšek and Stepišnik (2011). The breakthrough times of the red curve with $\sigma = 0.75$ and the 2D curve are almost identical. Also the amount of flow before and after breakthrough of these two curves does not differ much and is within one order of magnitude. Additionally, Fig. 5.6 shows the conduit evolution of the calibrated model. There, four snapshots in time are shown for the evolution of the calibrated model with $\hat{d}_0 = 0.3\,\text{mm}$ and $\sigma = 0.75$. The colors correspond to the relative increase of the initial diameter from a factor of 1.5 (blue) to a factor of $\geq 1000$ (orange) respectively. For a better visibility all conduits that have grown by less than a factor of 1.5 are not shown. The hydraulic heads are shown by colored contour lines from low head (blue) to high head (red) respectively. After 100 years (Fig. 5.6a) the enlarged conduits have captured one third of the crushed zone. After 200 years (Fig. 5.6b) the enlargement zone is further increased and after $\approx 300$ years (Fig. 5.6c) breakthrough has occurred (see also Fig. 5.5b). When the simulation is continued the enlargement zone also increases in the y- direction and would finally capture the whole domain (Fig. 5.6d). This behaviour is similar to a classical 2D model as e.g. presented by Bauer et al. (2003); Kaufmann (2003a); Romanov et al. (2003a) and corresponds almost perfectly to the evolution of the 2D model by Gabrovšek and Stepišnik (2011).

Because in this study the interaction of several crushed zones (dolines) is considered, it is not feasible to stick to the 2 m grid discretization for the whole domain. This would lead to model sizes in the range of $400 \times 400 \times 25$ nodes. From a technical point of view this means that the huge amount of data which these models create cannot be handled in a practicable way. Additionally, also the computational time would drastically increase. As it was also stated in 3.2.4 when dealing with a highly discretized dam–site model, the reader is referred to appendix A were several benchmark test have been carried out to find a practicable range of domain sizes. To cope with this limitation the resolution of the crushed zone is decreased to $dx = dy = 5\,\text{m}$. To check if this coarsening has an effect on the evolution of the model, it is also simulated with the same conduit diameter distributions and boundary conditions as the model with $dx = dy = 2\,\text{m}$ discretization from above. The resulting flow curves are shown in Fig. 5.5c. Also for the coarser network the

model with $\sigma = 0.75$ (red curve) fits the 2D curve as well as for the dense network and is therefore feasible to use.

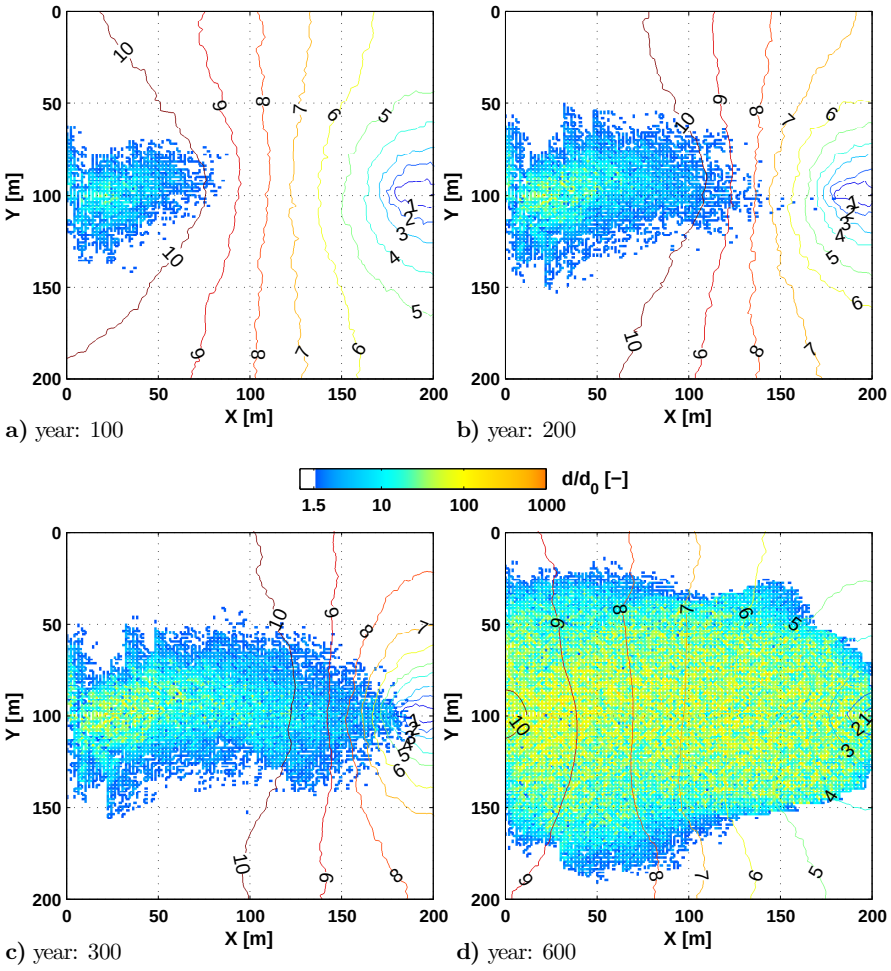


**Fig. 5.6:** Evolution of the doline calibration model with $\hat{d}_0 = 0.3\,\text{mm}$ and $\sigma = 0.75$ (red curve in Figs. 5.5a,b+c); **a)** evolution after 100 years; **b)** evolution after 200 years; **c)** evolution after 300 years - breakthrough has occurred; **d)** evolution after 600 years.

### 5.2.2 Extension into the third dimension

The next step in approaching a 3D doline model is to add the third dimension to the calibration model from the previous section. Therefore, the number of vertical layers is increased. Because in the 2D fracture network the fractures have a height

of 1 m, the crushed zone model is also only extended to 1 m in z–direction but with varying layer thicknesses or $dz$ values respectively. Fig. 5.5d shows the flow curves of these *extended* calibration models. The model with two nodes in z–direction and $dz = 1$ m is effectively the same model as in the calibration before but with the top conduit layer also activated. Due to the added layer the flow rates are higher also, but the breakthrough time is still comparable to the calibrated model. By adding more vertical layers, the global hydraulic conductivity of the crushed zone is increased and consequently also the flow through the domain. This can be seen from the increased flow rates in Fig. 5.5d. Because the main flow direction in this setup is along the x–direction, the breakthrough time is not that much effected by the increase of vertical layers (perpendicular to the flow direction).

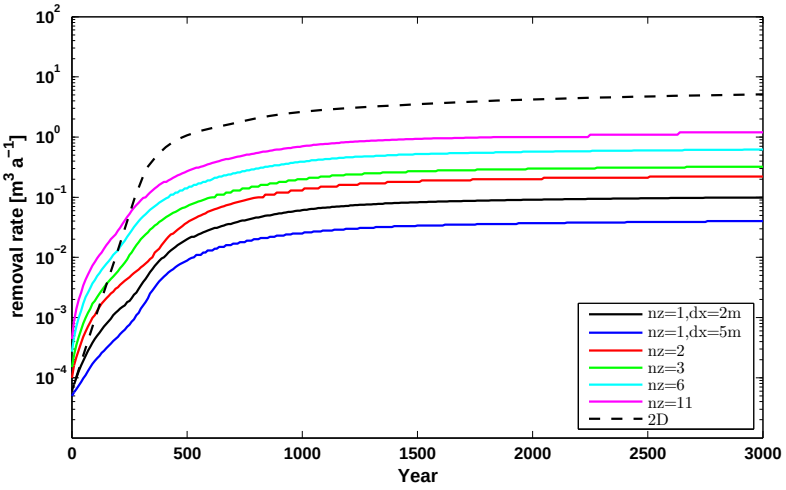


**Fig. 5.7:** Removal rates for the calibration models with $dx = 2$ m (black), $dx = 5$ m (blue) and the extended calibration models with 2 (red), 3 (green), 6 (cyan) and 11 (magenta) layers.

For the model with $nz = 17$ vertical layers the flow rate do not increase after the breakthrough at $\approx 1000$ years. This is a pure technical effect because the conduits have reached the maximum diameter, determined by the vertical discretization of $dz = 62.5$ mm. At this point the enlargement of the conduits has stopped and consequently the flow rates stay constant.

A three dimensional crushed zone with a certain amount of vertical layers allows for more flow and therewith has a higher potential for removing *collapsed* material from the crushed zone. This effect is shown in Fig. 5.7. There, the removal rates

are plotted for the calibrated models with $\hat{d}_0 = 0.3$ mm and $\sigma = 0.75$ for the finer network with $dx = dy = 2$ m (black curve) and the coarser network $dx = dy = 5$ m (blue curve) as well as for some extended models with more vertical layers. As more conduits and / or more layers come into play and therewith a larger surface for dissolution of course the removal rates increase. But even with more layers the extended 3D conduit model does not remove more material than the 2D fracture model. Obviously, this is due to the geometry of the fracture, that always captures the full *height* of 1 m and has therefore a bigger dissolution surface.

To effectively simulate the creation of a collapse doline and at the same time not to increase the model size to an impracticable extent, a mechanism has to be introduced that allows to remove material from the *surface* also with these quite low removal rates. Furthermore, this mechanism should not be a pure tuning parameter but somehow justified by the implementation of the conduit network in KARTSQUIFER itself. This mechanism is shown in 5.2.4.

### 5.2.3 3D model domain and boundary conditions

The general model domain that is used for the doline modelling is shown in Fig. 5.8. For a better comprehension the parameters are also summarized in Tab. 5.1.

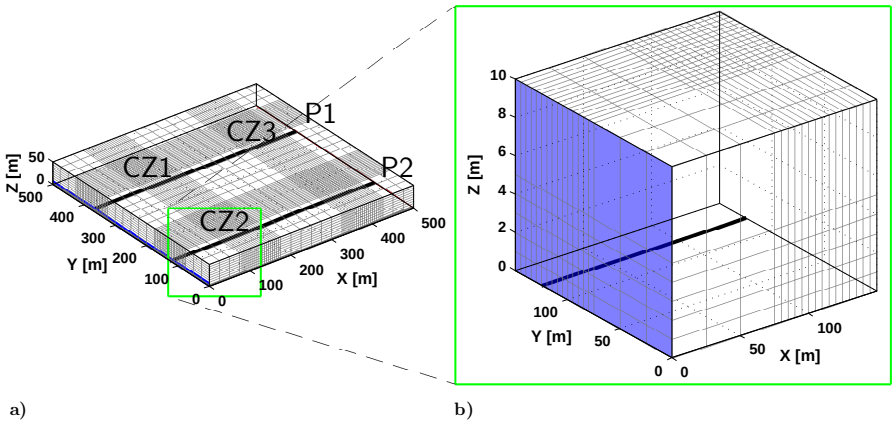


**Fig. 5.8:** 3D doline model setup; **a)** four zones with increased resolution are the crushed zones (CZ), two subsurface passages (black lines), see also Tab. 5.1, blue face marks const. head boundary condition of $H = 10$ m and red face const. head boundary condition of $H = 0$ m; **b)** green frame marks enlarged part from **a**, note that here the grid is out of scale.

The model domain for the 3D doline models is a $500 \times 500 \times 50\,\mathrm{m}^3$ limestone block. The discretization varies between $dx = dy = 5$ m inside the crushed zones and $dx = dy = 25$ m outside of the crushed zones. The vertical discretization varies between $dz = 1$m and $dz = 5$m respectively. Due to the use of a regular network and thus a constant amount of grid nodes in each spatial direction, the crushed zones are not implemented as pure local grid refinements (see Fig. 5.8). This leads of course to domain regions with a higher spatial resolution than necessary (e.g. between the crushed zones) and has to be considered in the interpretation of the results. The chemical parameters are according to the standard domain properties for limestone in Tab. 2.1. The hydraulic conductivity of the matrix is $K_m = 1 \times 10^{-5}\,\mathrm{m\,s^{-1}}$ and the conduit diameter distribution for the whole domain has parameters $\hat{d}_0 = 0.05$mm and $\sigma = 0.75$ which represents a quite intact (or immature) and only slightly fissured karst bedrock. The blue face in Fig. 5.8a marks the region where a constant head BC condition ($H = 10$ m) is applied. On the opposite domain boundary (not visible in Fig. 5.8a) a constant head BC of $H = 0$ m is applied to induce flow through the domain in x–direction.

| **Name** | **x-extent (dx)** | **y-extent (dy)** | **z-extent (dz)** | **network** |
|---|---|---|---|---|
| *Domain size* | 500 m<br>(5 − 25 m) | 500 m<br>(5 − 25 m) | 50 m<br>(1 − 5 m) | $\hat{d}_0 = 0.05$ mm, $\sigma = 0.75$ |
| *Crused zones* (CZ): | | | | |
| CZ1 | 75 − 175 m | 325 − 425 m | 0 − 5 m | $\hat{d}_0 = 0.3$ mm, $\sigma = 0.75$ |
| CZ2 | 75 − 175 m | 75 − 175 m | 0 − 5 m | $\hat{d}_0 = 0.3$ mm, $\sigma = 0.75$ |
| CZ3 | 325 − 425 m<br>(5 m) | 325 − 425 m<br>(5 m) | 0 − 5 m<br>(1 m) | $\hat{d}_0 = 0.3$ mm, $\sigma = 0.75$ |
| *Passages:* | | | | |
| P1 | 0 − 500 m | 375 m | 0 m | $d_0 = 0.13$ m |
| P2 | 0 − 500 m | 125 m | 0 m | $d_0 = 0.13$ m |

**Table 5.1:** Doline model parameters.

The domain is intersected by two subsurface streams / passages (black lines in Fig. 5.8a) passing through the model in x–direction at $z = 0$ m. The passages have an initial conduit diameter of $d_0 = 0.13$ m to establish flow rates between $1\,\mathrm{m^3\,s^{-1}}$ and $5\,\mathrm{m^3\,s^{-1}}$ depending on the chosen setup. These flow rates are in agreement with values reported from the field (e.g. Gabrovšek and Stepišnik (2011); Palmer and Palmer (2006)).

If a crushed zone is activated, its hydraulic conductivity is increased by assigning

the conduits inside the crushed zone new initial conduit diameters. Therewith, the mechanical weakening (enlarged fissures and fractures are already present) of the crushed zone is taken into account. The distribution parameters for these conduits are $\hat{d}_0 = 0.3\,\text{mm}$ and $\sigma = 0.75$ and are according to the calibration shown in 5.2.1.2.

### 5.2.4 Crushed zone – collapsing mechanisms

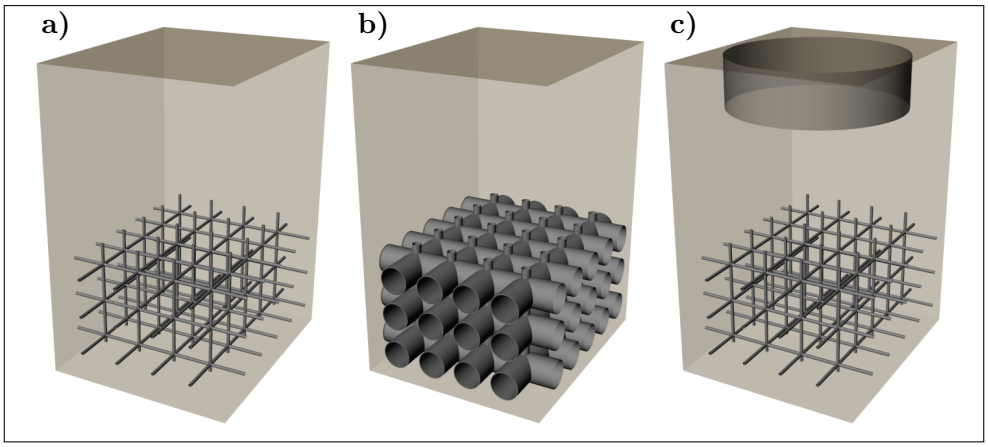


**Fig. 5.9:** Simulated mechanical *collapse* of the doline above the crushed zone; **a)** initial situation of the conduit network inside the crushed zone; **b)** horizontal conduits have reached a certain critical diameter; **c)** the horizontal conduits have *collapsed* and the topography is accordingly lowered.

Before investigating the evolution of the different 3D doline models the collapsing mechanisms that were applied are presented. Gabrovšek and Stepišnik (2011) used two mechanisms to mimic the processes in a crushed zone. The first one called *continuous infilling* is similar to the limited widening scheme shown in the previous chapter or e.g. by Romanov et al. (2010). If a fracture reaches a critical aperture width $A_{lim}$ then its enlargement is stopped but the dissolution is still active. Therefore, material is removed in a every time step but the fracture diameter is always reset to $A_{lim}$. Therewith, a continuous infilling by soluble material is assumed and a more or less constant flux rate (removal rate) is active. The second one called *discontinuous collapsing* resets the fracture aperture width to the initial or smaller aperture if a critical aperture is reached. After this reset the growth of the fracture starts again.

As collapsing is a more intuitive approach when considering collapse dolines,

three different collapsing mechanisms are applied in this work. The general implementation is exemplary shown in Fig. 5.9. Fig. 5.9a shows a portion of the model domain with the initially small conduits inside the crushed zone on the bottom of the limestone block. These conduits are enlarged over time by dissolution (Fig. 5.9b) and collapse back to a smaller conduit when a critical diameter $d_{crit}$ is reached. The smaller diameter is derived by the same statistical parameters $\hat{d}_0$ and $\sigma$ that are initially used for the conduits in the corresponding crushed zone. The difference between the critical and the small diameter after collapsing is used as the maximal possible value for surface lowering (Fig. 5.9c).

**Blocky collapsing** If the blocky collapsing is applied then four conduits that enclose one grid-element (see Fig. 2.4 - all conduits created by nodes $N_{1-4}$ or $N_{5-8}$) inside the crushed zone have to reach the critical diameter $d_{crit}$ before they are reset to a smaller conduit diameter. As in this model conduits represent fractures (see Fig. 2.1) it is more natural that a limestone block collapses (moves virtually downward) if all four bordering fractures (conduits) have reached a critical size.

**Layered collapsing** Layered collapsing is the extension of the *blocky* collapsing. Here, 75% of all conduits inside one depth layer have to reach the critical diameter $d_{crit}$ before the crushed zone collapses along this layer and all conduit diameters in that layer are reset.

**Total collapsing** Consequently, total collapsing is the extension of the *layered* collapsing and implies that 75% of all conduits inside the crushed zone have to reach the critical diameter $d_{crit}$ before the entire crushed zone collapses and all diameters in the crushed zone are reset.

## 5.3 3D Results

Now the results for the 3D doline models are presented. Four different layouts are tested where the complexity of the model increases from model 1 to model 4. Models 1 to 3 should be regarded as introduction to the domain layout, the evolution of a single doline and the test of the different collapse mechanisms. Whereas the final model 4 focuses on the interaction of a doline group.

### 5.3.1 Model 1 – one passage, one active crushed zone

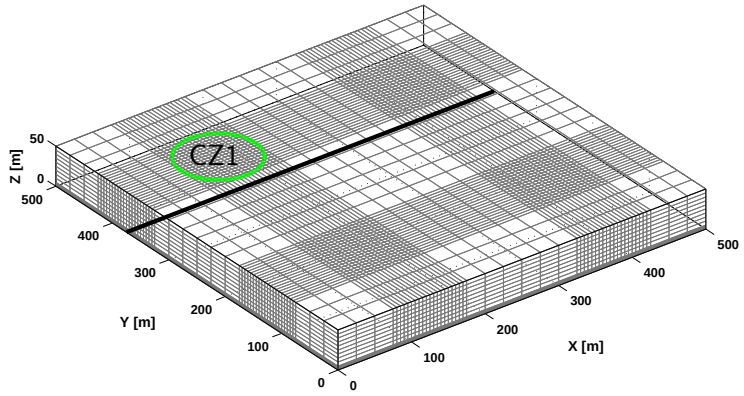


**Fig. 5.10:** Model setup for doline model 1; implemented are one subsurface passage (black line) and one active crushed zone CZ1 (green circle); the green circle also indicates that only conduits inside the circle are treated as crushed zone conduits; for the parameters used see Tab. 5.1.

The setup of the first doline model that is presented is shown in Fig. 5.10. One passage crosses the domain at $Y = 375$ m (black line) and one crushed zone CZ1 (green circle) is active that blocks this passage. Consequently, this model shows the "undisturbed" evolution of a 3D doline model. The domain and crushed zone parameters are summarized in Tab. 5.1 and the applied collapsing mechanism is the blocky collapsing (see 5.2.4). CZ1 initially blocks the passage, hence the simulation sets in after the first *collapsing* of CZ1 has already happened. Figs. 5.11 and 5.12 show the evolution of the conduit diameters and flux rates of model 1 for six snapshots in time. The simulation for model 1 and all following 3D doline models was done for 6000 years. For this first 3D doline model the evolution of conduit diameters will also be shown for introductory and continuity reasons. For all further 3D doline models only the flux rates are shown, because the main objective of this study is to investigate how much material is removed from the crushed zone and thereby estimating the possible surface lowering. Nevertheless, the conduit diameter evolution plots can be found in appendix B. In addition to Figs. 5.11 and 5.12, Fig. 5.13 shows the evolution of several relevant model parameters over time and will be simultaneously used for the interpretation.

The hydraulic heads in Figs. 5.11 and 5.12 are again shown as isosurfaces of constant head with a grey color scale from dark grey (low head) to light grey (high

head) respectively. The increase of the conduit diameter compared to the initial conduit diameter $d/d_0$ is plotted on a log–scale where dark blue colors represent no change $d/d_0 = 10^0 = 1$ and red colors an increase by a factor of $d/d_0 \geq 10^3 = 1000$ or more. Like for previous figures only conduits increased above a certain threshold are plotted as indicated by the color scale. The flux rates are plotted on a log–scale in the range from $10^{-12}$ [mol m$^{-2}$ s$^{-1}$] (dark blue) to $10^{-7}$ [mol m$^{-2}$ s$^{-1}$] (red). For better visibility conduits with smaller flux rates than given by the color scale are not shown.

Figs. 5.11a and 5.12a show the initial situation for model 1. From the head isosurfaces it can be seen that CZ1 initially blocks the passage and therefore increases the hydraulic gradient inside CZ1. Parallel to the flow direction up to $\approx$ 100 m in x-direction small flux rates around $10^{-12}$ [mol m$^{-2}$ s$^{-1}$] (blue) have established (Fig. 5.12a). Due to higher flow inside the passage, there the flux rates are around $10^{-10}$ [mol m$^{-2}$ s$^{-1}$] (cyan). These higher flux rates are also visible inside CZ1 because there the diameters are initially larger compared to the rest of the domain. In the entry part of CZ1 between 75 m and 100 m even higher flux rates of $10^{-9}$ [mol m$^{-2}$ s$^{-1}$] (yellow) are already visible.

In Fig. 5.11b after 300 years of evolution one can see that the conduits inside CZ1 have already grown by a factor of $\approx$ 10 (cyan), in the central part along the passage even more by a factor of $\approx$ 75 (green / yellow). In contrast to the initial setup in Fig. 5.11a, the head isosurfaces are now almost parallel inside the crushed zone. This indicates the connection of the entrance and the exit of the crushed zone by a an enlarged conduit path and can therefore be considered as a somewhat *local* breakthrough event. This can also be seen in Fig. 5.13a where the flow rate at the output node of passage 1 increases rapidly at $\approx$ 150 years also indicating the breakthrough similar to the dam–site models in 3 and 4. Fig. 5.12b shows that the highest flux rates have established inside the passage and inside CZ1 (orange). The flux rates up– and downstream are still low (blue colors) but capture a zone with the same width (along the y–direction) as CZ1 up to $x \approx 250$ m. However, the most material is mainly removed from inside the crushed zone.

Figs. 5.11c and 5.12c show the model after 1300 years. The conduits inside CZ1 have further increased in diameter up to a factor of $\geq$ 100 (yellow). But also the conduits along the domain boundary at $x = 0$ m as well as conduits downstream of CZ1 have enlarged. This is also visible in the flux rates in Fig. 5.12c. The flux rates

in the zone around CZ1 have slightly increased and this zone has penetrated deeper into the domain.

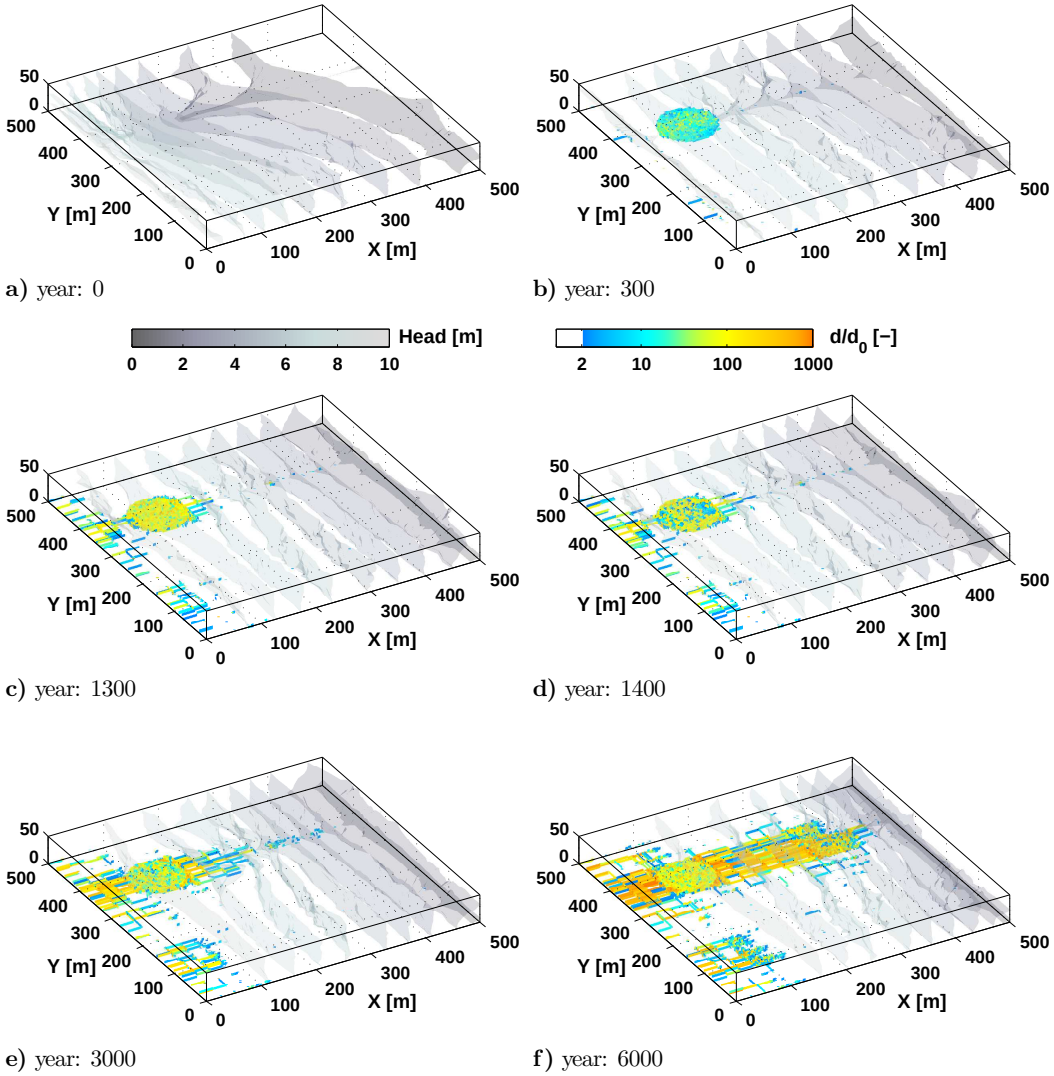


**a)** year: 0 **b)** year: 300

**c)** year: 1300 **d)** year: 1400

**e)** year: 3000 **f)** year: 6000

**Fig. 5.11:** Conduit diameter evolution of the 3D doline model 1 for different snapshots in time; Below each subplot the year is given; the isosurfaces of constant head from low (dark grey) to high (light grey) values and the relative increase of the conduit diameter compared to the initial diameter on a log–scale from 2 (blue) to $\geq 1000$ (orange).

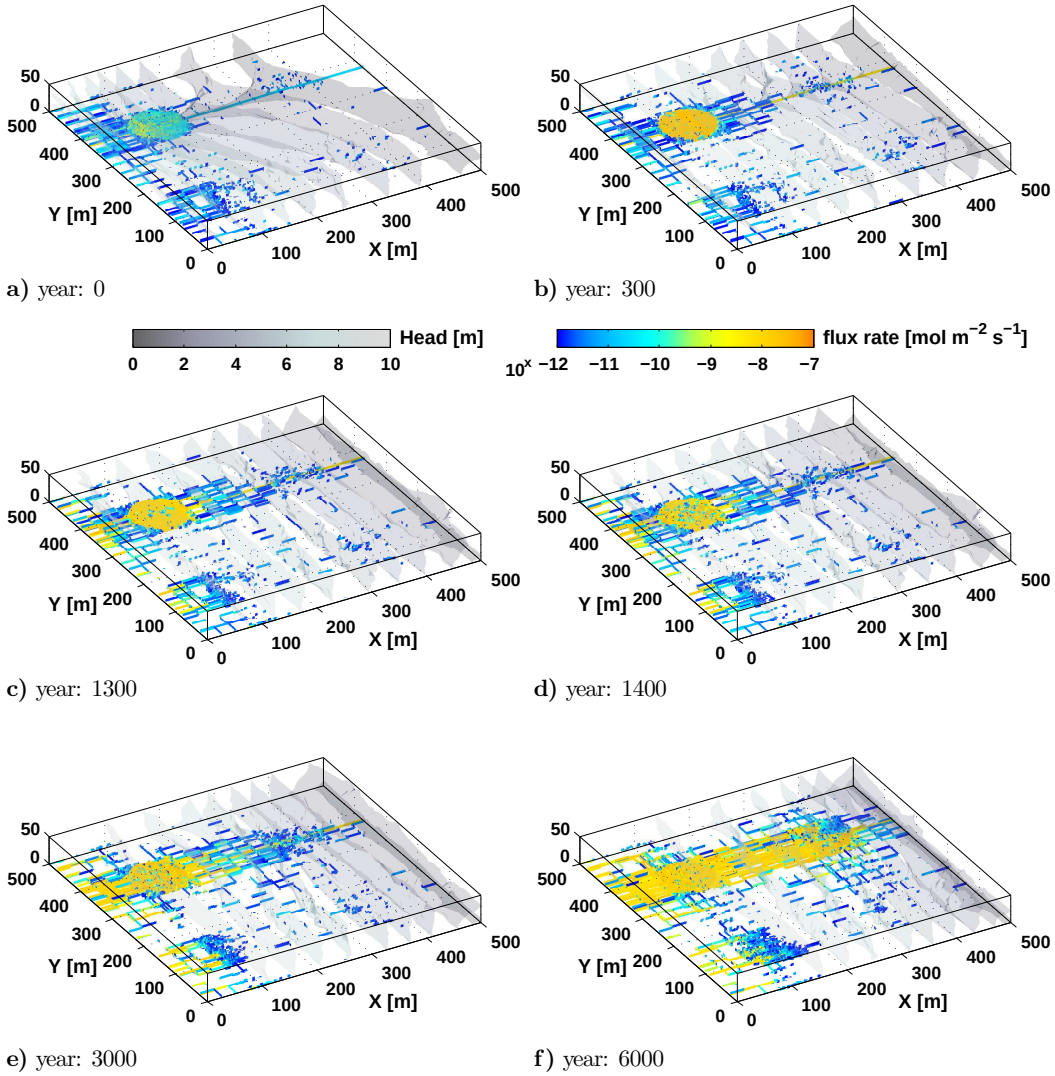


**Fig. 5.12:** Flux rate evolution of the 3D doline model 1 for different snapshots in time; Below each subplot the year is given; plotted are the isosurfaces of constant head from low (dark grey) to high (light grey) values and the flux rates inside the conduit on a log–scale from $10^{-12}$ [mol m$^{-2}$ s$^{-1}$] (blue) to $10^{-7}$ [mol m$^{-2}$ s$^{-1}$] (orange).

Furthermore, Fig 5.12c shows that the flux rates in the center of CZ1 have partially decreased (cyan). At these spots the conduits around one grid element have *collapsed* and a smaller diameter has been reset. The collapsing event is also visible in Fig. 5.13. In Fig. 5.13a the effect is not that much pronounced and only a small

kink at ≈ 1300 years is visible in the flow curve. In Fig. 5.13b the drop in removal rates due to the established smaller conduit diameters shows much better the effect of the beginning collapse. The simulated surface lowering induced by the collapsing of the conduits is visualized in Figs. 5.13c+d. Fig. 5.13c shows the evolution of the surface along a profile above passage 1 over time. The abscissa represents the length in x–direction at $y = 375$ m and the ordinate the time respectively. Color coded is the topography along this line from 50 m (orange) to 48 m (blue) respectively. In Fig. 5.13c it can also be seen that the first surface lowering starts at ≈ 1200 years. The direct indicator for the onset of collapsing is Fig. 5.13d. There, the estimated cumulative loss of surface volume above the crushed zone is shown. For the presented simulations always the maximal possible value of collapsing is assumed, so that the volume that is removed from the surface for each block $V_b$ is calculated by

$$V_b = ab\,(d_{crit} - \text{mean}(d_b))\,, \tag{5.1}$$

with $a = dx = 5$ m, $b = dy = 5$ m and $d_b$ [m] the new reset conduit diameters of the four conduits surrounding one single block. As explained in 5.2.4 this procedure accounts for the representation of fractures (discontinuity planes inside the bedrock) by conduits in the KARSTAQUIFER model. Thereby, a limestone *column* can only move $d_{crit} - \text{mean}(d_b)$ m virtually downward. Within the model the location of the nodes inside the crushed zone are not changed, the height difference is directly applied to the surface nodes. Of course the direct correlation of collapsing conduits (fractures) and surface lowering is not given in reality. But here it allows for good estimation of surface material removal especially considering the fact that no erosional or mechanical forces are implemented into the model. Note that the curve in Fig. 5.13d is a cumulative curve and not a rate per year. Like Fig. 5.13c also Fig. 5.13d indicates the onset of collapsing at ≈ 1200 years.

Figs. 5.11d and 5.12d show the model after 1400 years of evolution. Now the collapsing inside the crushed zone is also visible in the conduit evolution in Fig. 5.11d whereas the surrounding domain has not much changed. A similar picture can be seen in Fig. 5.12d where the decreased flux rates inside the crushed zone indicate the collapsing. Some more information can be gained from Fig. 5.13d where one can see that this first collapsing *era* ends at ≈ 1500 years as now almost every block inside the crushed zone has been affected. For the next 1000 years there is no significant surface lowering because the conduits inside CZ1 have not reached

their critical diameter yet. The next collapsing *era* starts at $\approx 2500$ years and ends at $\approx 2800$ years. Then there is again a plateau stage expanding over $\approx 900$ years. From $\approx 3700$ years on the collapsing is a rather continuous process than marked by clear collapsing events. This can be expected as the collapsing mechanism acts individually on a single block inside the crushed zone. Therewith, the effect of a single block on the lowering of the whole doline is leveled out during the evolution. A similar picture is drawn by Figs. 5.13a+b. The flow rates (Fig. 5.13a) increase steadily as the diameter of the passage is steadily increased. And due to the now continuous collapsing the flow rate shows no jumps or kinks because there is always a preferential path of enlarged conduits available that connects the entrance of CZ1 with its exit and so keeping a constant flow rate. After $\approx 3700$ years the removal rates inside the conduits of CZ1 is also rather constant at $\approx 10^{-2}\,\mathrm{m^3\,a^{-1}}$ (green curve in Fig. 5.13b) whereas the rates increase for the continuously enlarging conduits inside the domain (black curve).

Later stages in the evolution of model 1 are shown in Figs. 5.11e+f and 5.12e+f after 3000 and 6000 years respectively. After 3000 years the enlarged conduits have grown further downstream along the passage and also significantly increased along the input boundary. After 6000 years this increase is even more pronounced. The crushed zone more or less acted like a flow–distributor and has therewith created a wide zone of enlarged conduits parallel to the passage. Necessarily, this enlargement is also reflected by the increased flux rates. In Figs. 5.12e+f one can see that the highest flux rates correspond to the strongly increased conduit diameters and vice versa. Actually, if CZ3 downstream of passage 1 (see Fig. 5.8) would have been activated in this model, some blocks would have started to collapse already (this interaction is shown later in model 4).

Figs. 5.13b–d show that after 6000 years of evolution the yearly removal rate inside the crushed zone is $\approx 10^{-2}\,\mathrm{m^3\,a^{-1}}$. Due to the implementation of the collapsing mechanism it is possible to simulate a surface lowering to $\approx 48.7$ m above the crushed zone from these small removal rates. This surface lowering corresponds to a removal of material in the range of $\approx 10^4\,\mathrm{m^3}$ after 6000 years.

### 5.3.2 Model 2 – two passages, one active crushed zone

Now the effect of a second passage crossing the domain at $Y = 125$ m (Fig. 5.14) is investigated. All other domain parameters are identical to model 1. Furthermore,

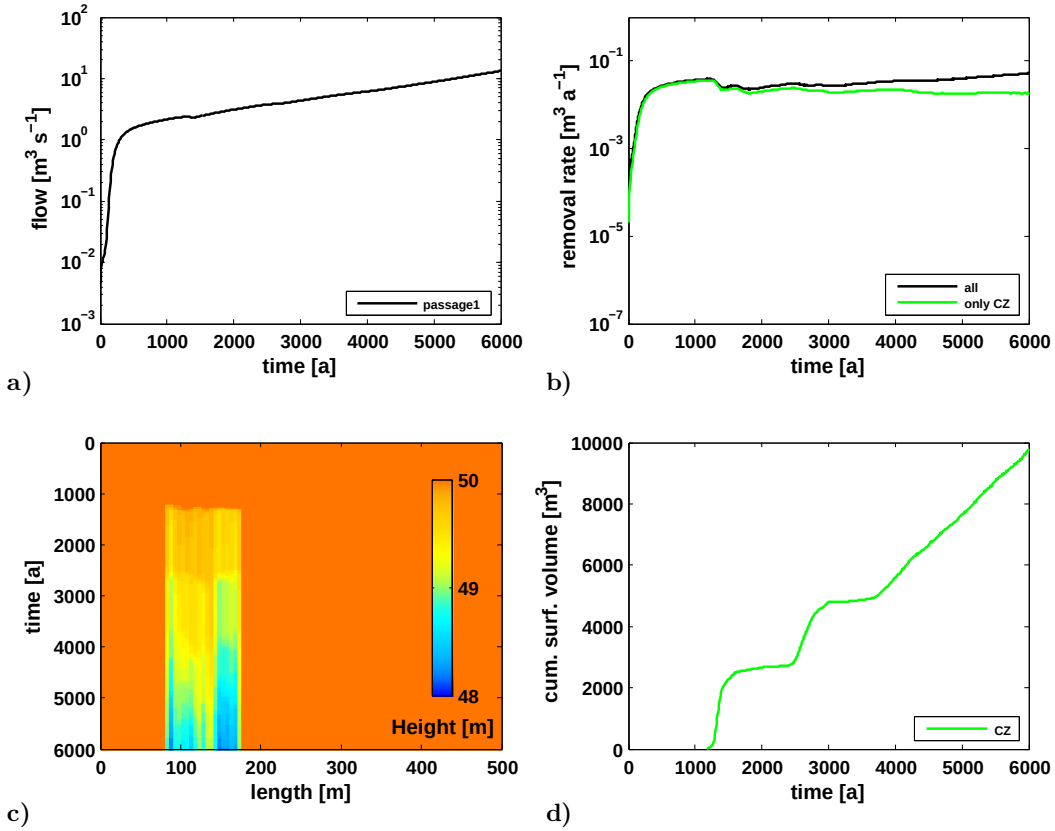


**Fig. 5.13:** Results for 3D doline model 1; **a)** flow rates at the output of passage 1; **b)** removed material per year for all conduits (black curve) and only conduits inside crushed zone CZ1 (green); **c)** height *spectra* along a surface profile above passage 1 showing the surface lowering over time; **d)** estimated cumulative loss of surface volume for CZ1.

also the effect of the different collapsing mechanisms as introduced in 5.2.4 is presented. For explaining the evolution of the different models only the flux rate is used now as the information in the conduit diameter evolution plots is somehow redundant. However, for completeness the figures showing the evolution of the conduit diameters can be found in appendix B.1.

#### 5.3.2.1 Model 2 with blocky collapsing mechanism

The effect of a second passage added to the doline model is shown in Figs. 5.15 (flux rates) and 5.16 (flow rates, surface loss etc.).

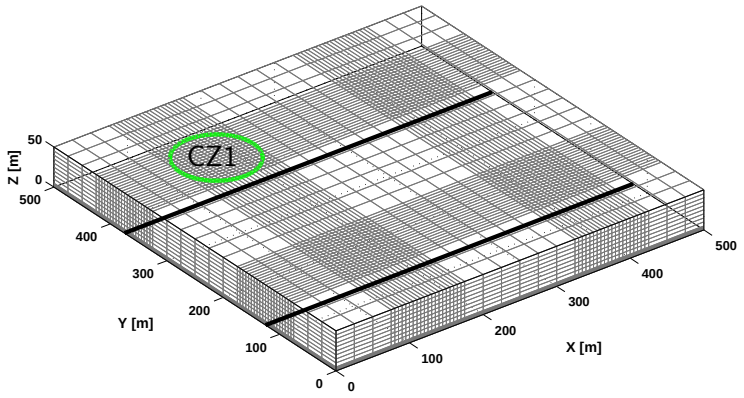


**Fig. 5.14:** Model setup for doline model 2; implemented are two subsurface passages (black lines) and one active crushed zone CZ1 (green circle); the green circle also indicates that only conduits inside the circle are treated as crushed zone conduits; for the parameters used see Tab. 5.1.

When comparing the subplots in Figs. 5.12 (model 1) and 5.15 no significant change is visible for the part containing the crushed zone. The highest rates are established along passage 1 and inside CZ1. The local breakthrough inside CZ1 happens again at $\approx$ 150 years (see Fig. 5.16a). The collapsing of single blocks inside CZ1 sets in at $\approx$ 1300 years which is identical to model 1. Furthermore, in Fig. 5.16d one can again clearly see the two collapsing *eras* marked by the two jumps in the curve showing the cumulative surface volume loss.

Obviously, model 2 only differs significantly from model 1 in regions where the second passage is crossing the domain. Already at the beginning, the highest rates are established inside passage 2 (Fig. 5.15a). Due to the unblocked passage 2 calcium aggressive water is transported deep into the domain and in contrast to passage 1 low flux rates are also established along the passage. At later time steps the influence of passage 2 becomes even more pronounced. After 6000 years of evolution high rates are established up to $x \approx 150$ m whereas for model 1 the flux rates always are orders of magnitude smaller. Also visible is the *connection* between the two passages at $x \approx 350$ m in terms of low flux rates. Note that in the figures this effect may be over–pronounced due the high grid resolution along the passages and inside the virtual crushed zone regions. But even if the grid would be completely regular, the second passage would still allow much more aggressive water to flow deeper into the domain and accelerate the evolution there.

Because passage 2 is already quite large from the beginning and not blocked by a crushed zone, the flow rate increases steadily over time (Fig. 5.16a – green curve). After 6000 years of evolution the flow rate inside passage 1, although it is temporarily blocked, is $\approx 10\,\%$ higher than in passage 2. The reason for this is that the enlarged zone along passage 1 with its high flux rates acts like a wide single channel on its way to a *global* breakthrough. More fresh water can be transported downstream and therewith more material can be removed. Like already stated for model 1, if CZ2 or CZ3 would have been *mechanically* activated, several collapsing events would be visible after 6000 years.

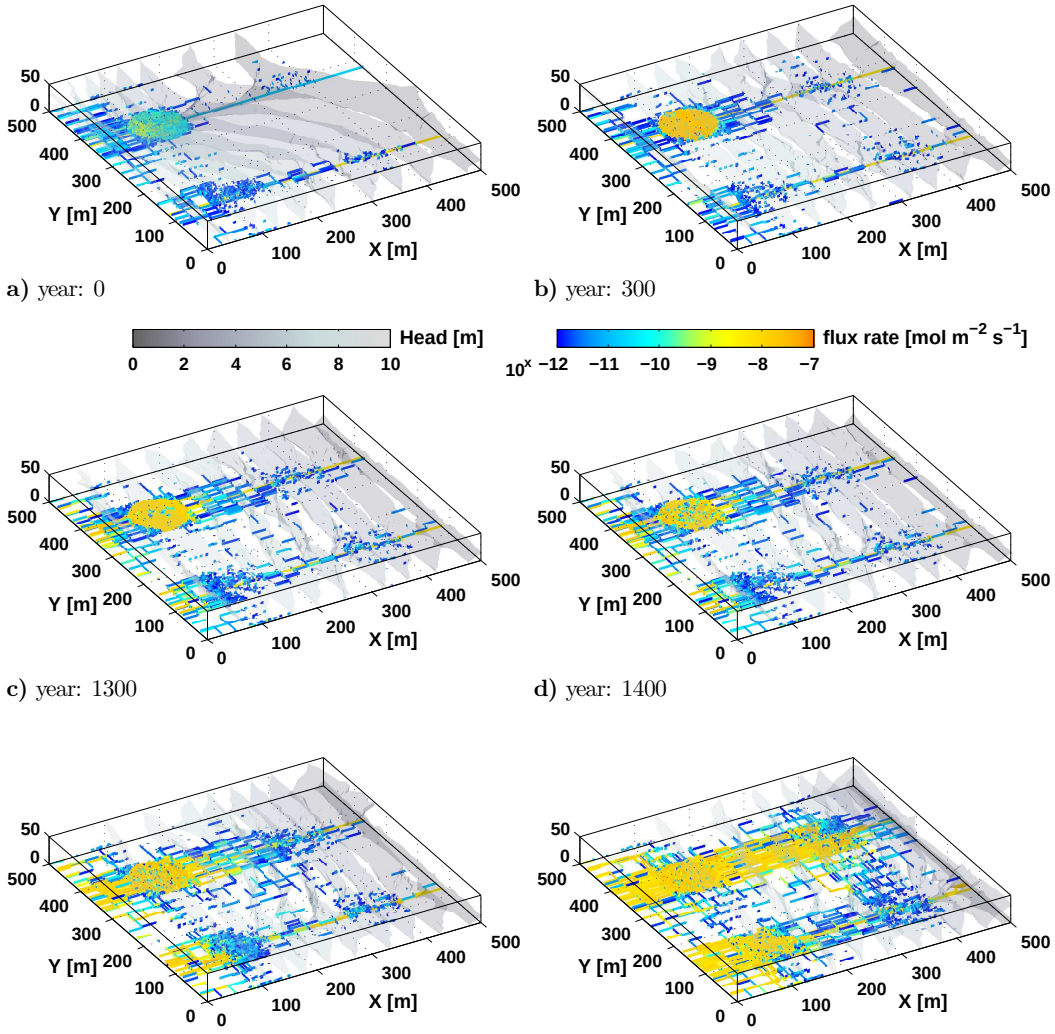


**a)** year: 0 **b)** year: 300

**c)** year: 1300 **d)** year: 1400

**e)** year: 3000 **f)** year: 6000

**Fig. 5.15:** Flux rate evolution of the 3D doline model 2 (blocky collapsing) for different snapshots in time; Below each subplot the year is given; plotted are the isosurfaces of constant head from low (dark grey) to high (light grey) values and the flux rates inside the conduit on a log-scale from $10^{-12}$ [mol m$^{-2}$ s$^{-1}$] (blue) to $10^{-7}$ [mol m$^{-2}$ s$^{-1}$] (orange).

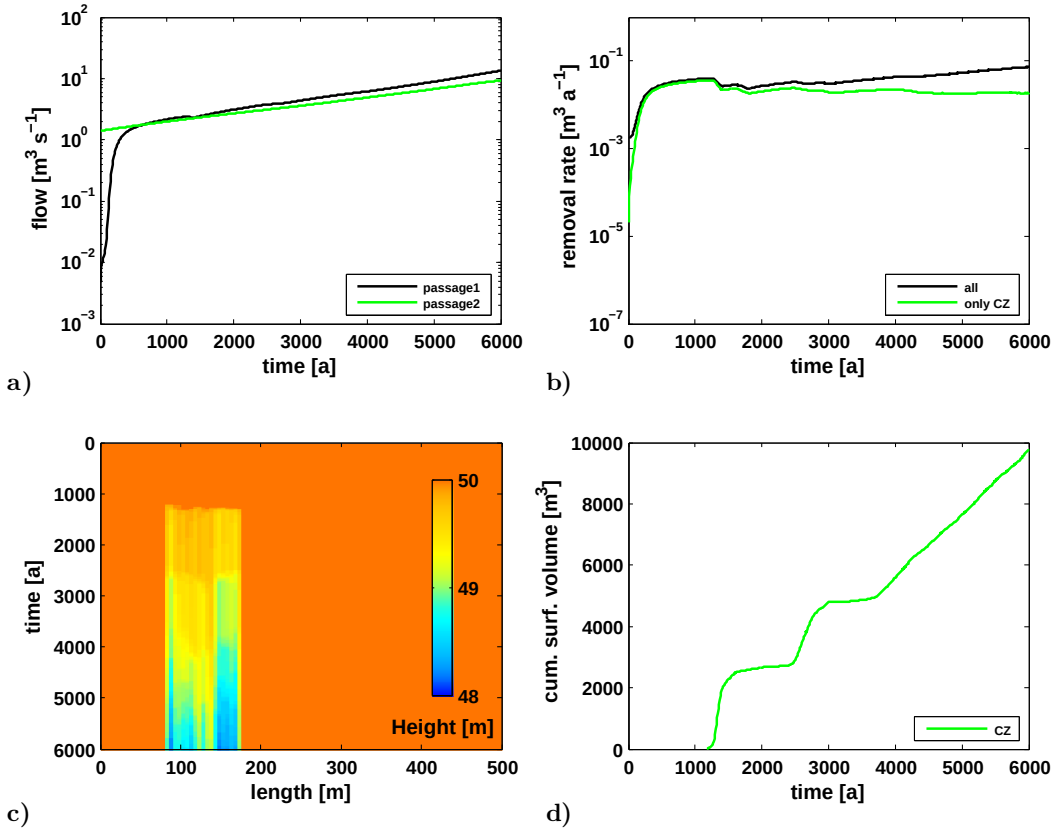


**Fig. 5.16:** Results for 3D doline model 2 (blocky collapsing); **a)** flow rates at the output of passage 1 (black) and passage 2 (green); **b)** removed material per year for all conduits (black curve) and only conduits inside crushed zone CZ1 (green); **c)** height *spectra* along a surface profile above passage 1 showing the surface lowering over time; **d)** estimated cumulative loss of surface volume for CZ1.

#### 5.3.2.2 Model 2 with layered collapsing mechanism

Now the effect of the different collapsing mechanism on the evolution of the doline model is investigated. All parameters are identical to model 2 with blocky collapsing but now the layered collapsing is applied (see 5.2.4). Initially the models are of course inherently the same and show the same evolution. Whereas for the model with blocky collapsing the onset of collapse is at $\approx$ 1300 years nothing has happened for the model with layered collapsing. This is of course to be expected because the criteria for a collapse event is that 75 % of all conduits inside one depth layer of the crushed zone have to reach the critical diameter $d_{crit}$. The collapsing starts at

$\approx$ 1400 years and happens for all layers within 10 years of evolution. Due to this quite abrupt collapsing the whole crushed zone is reset and the passage is blocked. Note the high head gradients inside the crushed zone in Fig. 5.17d after the collapse. Due to the blocking of CZ1, no material is removed from the region downstream of CZ1 right after the collapse (compare Figs. 5.15d and 5.17d).

The influence of the layered collapse mechanism can best be seen in Fig. 5.18. The collapse event is clearly visible by sharp cuts in the flow curve (Fig. 5.18a – black curve) and removal rate curve (Fig. 5.18b – green curve) respectively. After the first collapse at $\approx$ 1400 years the collapsing happens periodically every $\approx$ 1300 years. This periodicity is of course determined by the critical diameter $d_{crit}$ which is from a mechanical point of view rather small within this model but chosen for practical reasons. Here, $d_{crit} = 0.05$m and allows therefore for at least four collapsing events within the presented 6000 time steps. If a larger value for $d_{crit}$ would have been chosen the time until the first collapse and therefore the calculation time would have been unnecessarily increased. Due to the fact that always the maximal possible value for the surface lowering is used the effect of a larger $d_{crit}$ is similar to the smaller $d_{crit}$ and a shorter time scale.

The layered collapsing of course also changes the evolution of the topography. As now the collapsing happens along one depth layer simultaneously Fig. 5.18c shows the evolution of the topographic height over time for the whole crushed zone and not only along a profile like in Figs. 5.13c and 5.16c. After 6000 years the topography above CZ1 is lowered to $\approx$ 48.7 m and $\approx$ 9 500 m$^3$ of material are removed from the surface (Fig. 5.18d).

However, after 6000 years of evolution the two collapsing mechanisms differ only slightly from each other in terms of domain evolution. In Figs. 5.15f and 5.17f one can see slight differences in the flux rates in the region of the not activated CZ3 and between the two passages at $x \approx 350$ m but generally their evolution is identical. These small differences are also visible in the conduit evolution plots (Figs. B.1 and B.2). As in a way to be expected the different collapse mechanism has no influence whatsoever on the flow rate inside the second passage (see Fig. 5.18a).

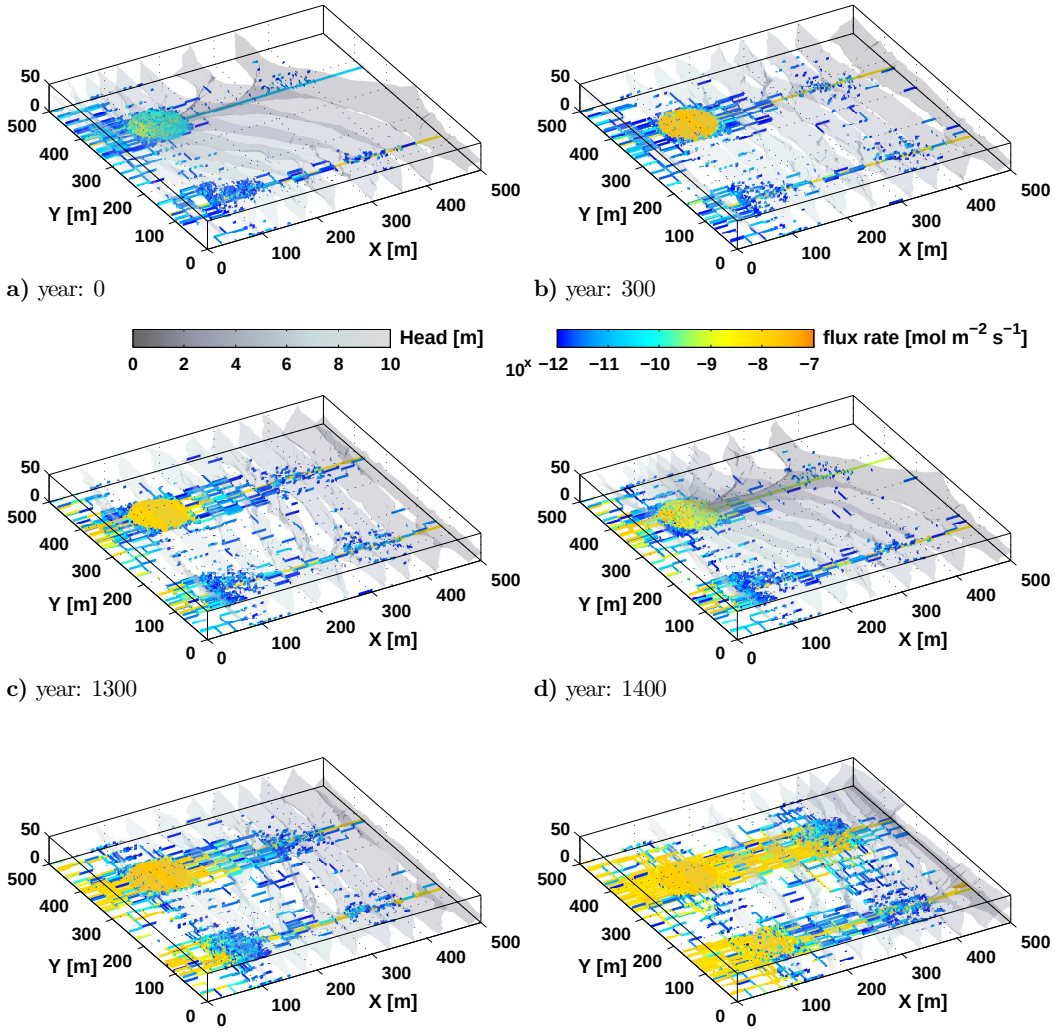


**a)** year: 0 **b)** year: 300

**c)** year: 1300 **d)** year: 1400

**e)** year: 3000 **f)** year: 6000

**Fig. 5.17:** Flux rate evolution of the 3D doline model 2 (layered collapsing) for different snapshots in time; Below each subplot the year is given; plotted are the isosurfaces of constant head from low (dark grey) to high (light grey) values and the flux rates inside the conduit on a log-scale from $10^{-12}$ [mol m$^{-2}$ s$^{-1}$] (blue) to $10^{-7}$ [mol m$^{-2}$ s$^{-1}$] (orange).

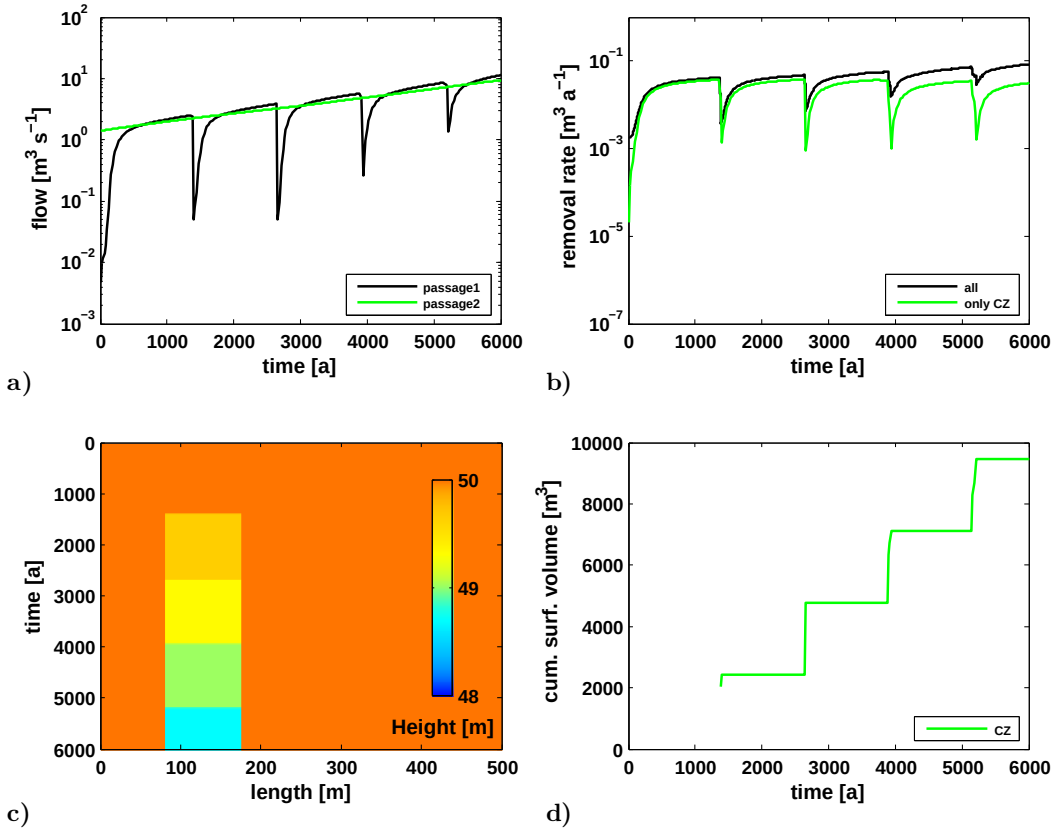


**Fig. 5.18:** Results for 3D doline model 2 (layered collapsing); **a)** flow rates at the output of passage 1 (black) and passage 2 (green); **b)** removed material per year for all conduits (black curve) and only conduits inside crushed zone CZ1 (green); **c)** height *spectra* along a surface profile above passage 1 showing the surface lowering over time; **d)** estimated cumulative loss of surface volume for CZ1.

#### 5.3.2.3 Model 2 with total collapsing mechanism

Because the total collapsing mechanism is basically nothing more than a combined layered collapse, the domain evolutions are nearly identical. Therefore, also Figs. 5.17 and 5.19 are almost identical. A slight difference is only visible in Figs. 5.18 and 5.20. Because the crushed zone is instantaneously blocked by the total collapsing mechanism the flow and removal rates decrease a little stronger. A similar fact holds for the evolution of the topography. There, the final surface lowering is a little smaller compared to the layered collapse due to lesser collapse events (the collapse criteria is yet not reached for the total collapsing mechanism). Effectively, the height

difference between both collapse mechanisms is ≈ 20 cm which means that in the time range considered only 4 layers more have collapsed with the layered collapse model.

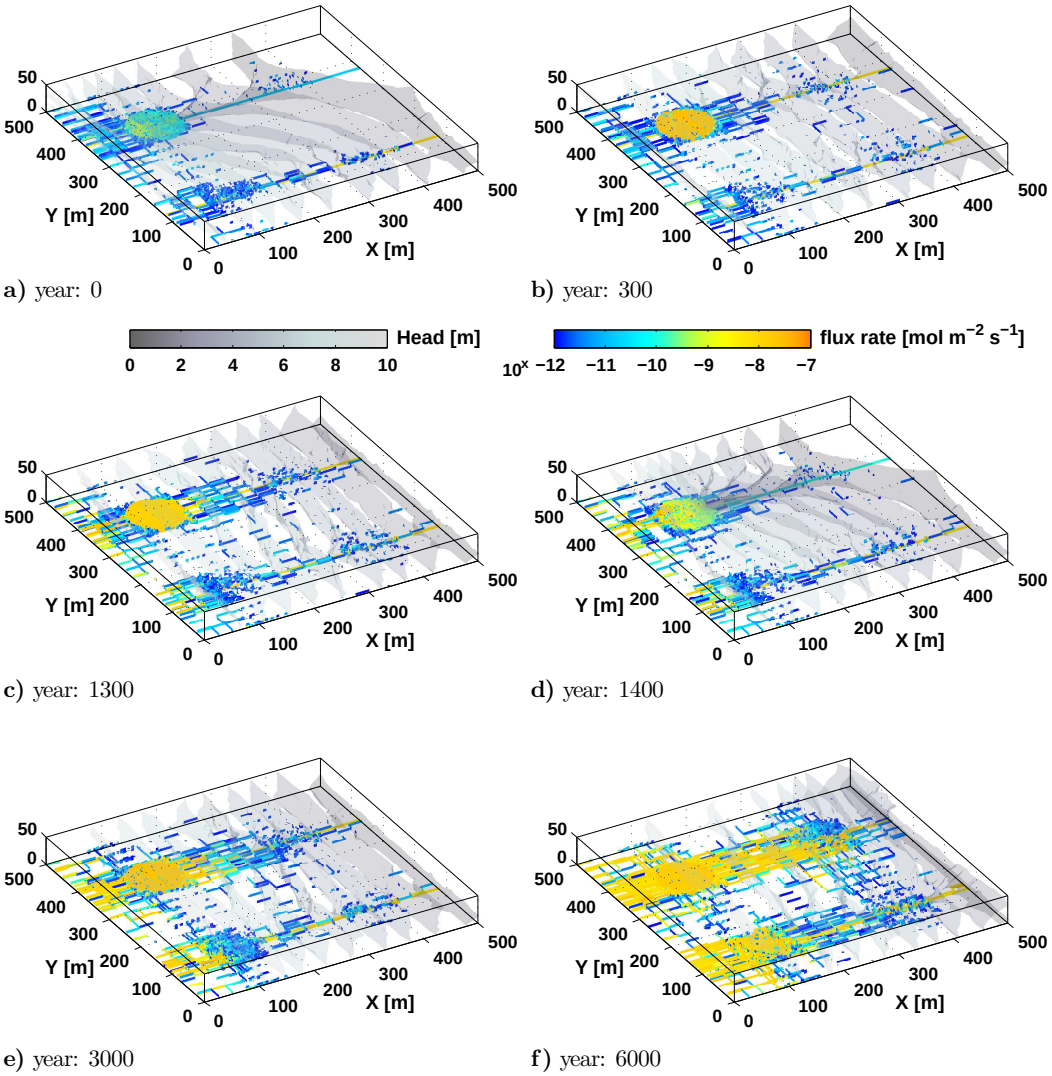


**a)** year: 0 **b)** year: 300

**c)** year: 1300 **d)** year: 1400

**e)** year: 3000 **f)** year: 6000

**Fig. 5.19:** Flux rate evolution of the 3D doline model 2 (total collapsing) for different snapshots in time; Below each subplot the year is given; plotted are the isosurfaces of constant head from low (dark grey) to high (light grey) values and the flux rates inside the conduit on a log–scale from $10^{-12}$ [mol m$^{-2}$ s$^{-1}$] (blue) to $10^{-7}$ [mol m$^{-2}$ s$^{-1}$] (orange).

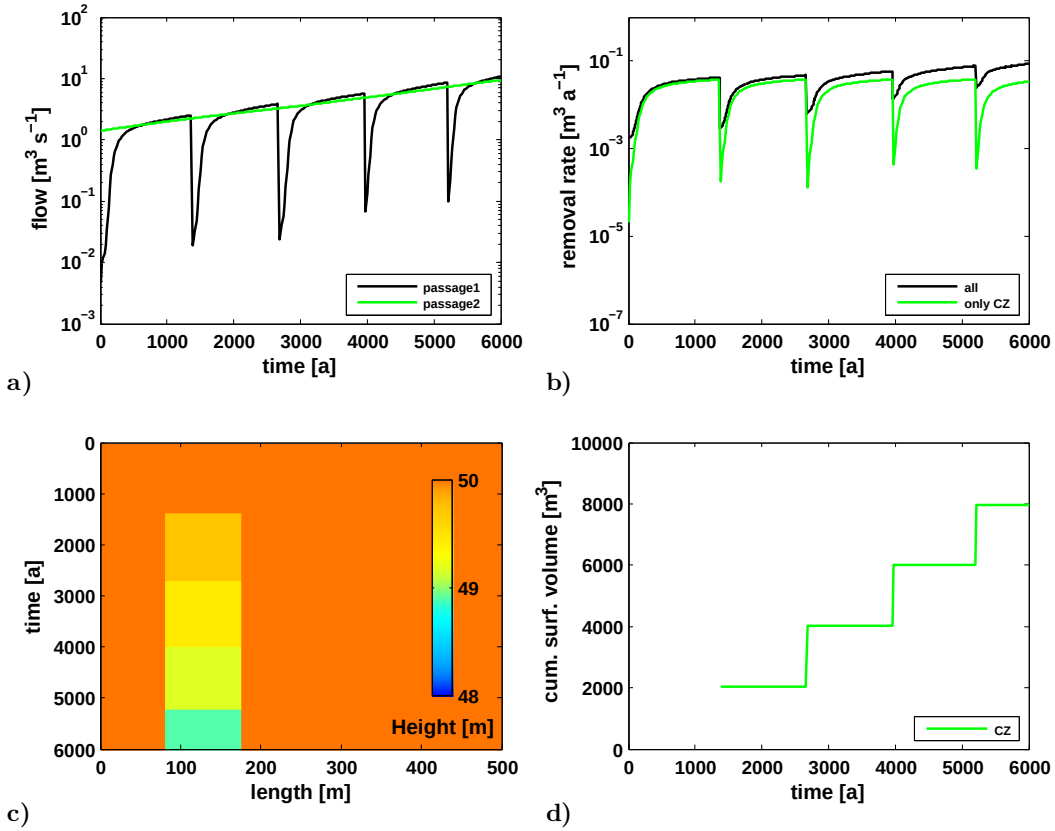


**Fig. 5.20:** Results for 3D doline model 2 (total collapsing); **a)** flow rates at the output of passage 1 (black) and passage 2 (green); **b)** removed material per year for all conduits (black curve) and only conduits inside crushed zone CZ1 (green); **c)** height *spectra* along a surface profile above passage 1 showing the surface lowering over time; **d)** estimated cumulative loss of surface volume for CZ1.

### 5.3.3 Model 3 – two passages, two active crushed zones

In model 3 now a second crushed zone (CZ2) is activated along passage 2 to investigate if and how the two crushed zones interact in their evolution (Fig. 5.21). For this model only the layered collapsing mechanism is considered. The figure showing the evolution of the conduit diameters can be found in appendix B.2.

For the first 1300 years the evolution of model 3, in particular the evolution of the domain along the two passages, is comparable to the evolution of passage 1 in model 2. Both passages in Fig. 5.22a are initially blocked by the crushed zones and it takes again $\approx$ 150 years for the local breakthrough to occur. As for model 2 the highest

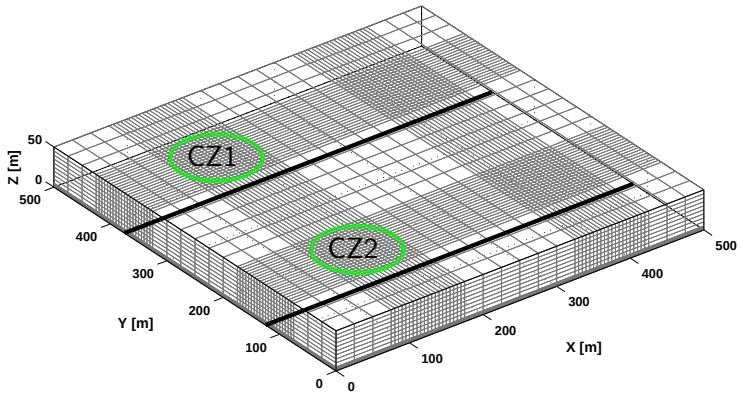


**Fig. 5.21:** Model setup for doline model 3; implemented are two subsurface passages (black lines) and two active crushed zones CZ1 and CZ2 (green circles); the green circles also indicate that only conduits inside the circles are treated as crushed zone conduits; for the parameters used see Tab. 5.1.

flux rates and therewith the fastest evolution are established inside the passages and the crushed zones, respectively. The first collapse event occurs for both crushed zones after $\approx$ 1430 years of evolution as shown in Fig. 5.22d. Generally, as it can be seen from Figs. 5.22 and 5.23 both passage compartments evolve simultaneously. The collapse period is for both crushed zones $\approx$ 1400 years and after 6000 years of evolution the surface above both crushed zones has lowered to $\approx$ 48.7 m (see Fig. 5.23c). When comparing later stages in the evolution of model 2 (Figs. 5.17e+f) and model 3 (Figs. 5.22e+f) one can see that there are less horizontal connections between both passages. This is again due to the wide single channel behaviour of the regions around both passages. They act like two competing channels on their global breakthrough paths as it is known from e.g. Bauer et al. (2003); Kaufmann (2003a); Romanov et al. (2003a) for their 2D benchmark models.

Generally, both passages and both crushed zones evolve independently from each other. Furthermore, as they have similar properties in terms of initial conduit diameter distribution, they evolve in a similar way. It seems that the distance between both passages / crushed zones is too big to have any effect. In B.2.1 another layout for model 3 is presented. There, both crushed zones are connected horizontally. But also this layout has no effect on the general evolution of model 3. This is due to the fact, that both passages / crushed zones start from similar initial conditions but more importantly they are placed in parallel regarding the main direction of flow.

So the geometry or layout of the crushed zones has to be further extended.

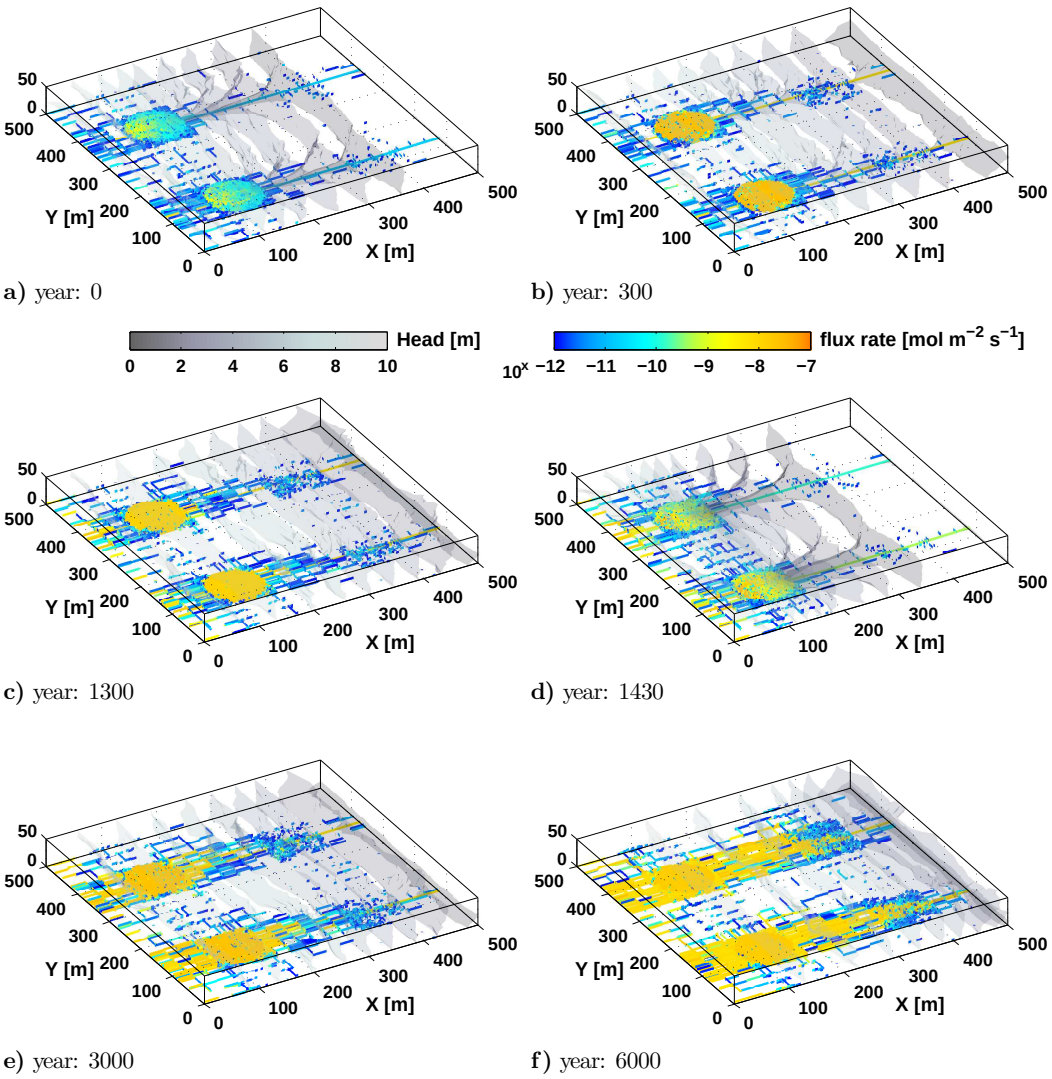


**a)** year: 0 **b)** year: 300

**c)** year: 1300 **d)** year: 1430

**e)** year: 3000 **f)** year: 6000

**Fig. 5.22:** Flux rate evolution of the 3D doline model 3 (layered collapsing) for different snapshots in time; Below each subplot the year is given; plotted are the isosurfaces of constant head from low (dark grey) to high (light grey) values and the flux rates inside the conduit on a log-scale from $10^{-12}$ [mol m$^{-2}$ s$^{-1}$] (blue) to $10^{-7}$ [mol m$^{-2}$ s$^{-1}$] (orange).

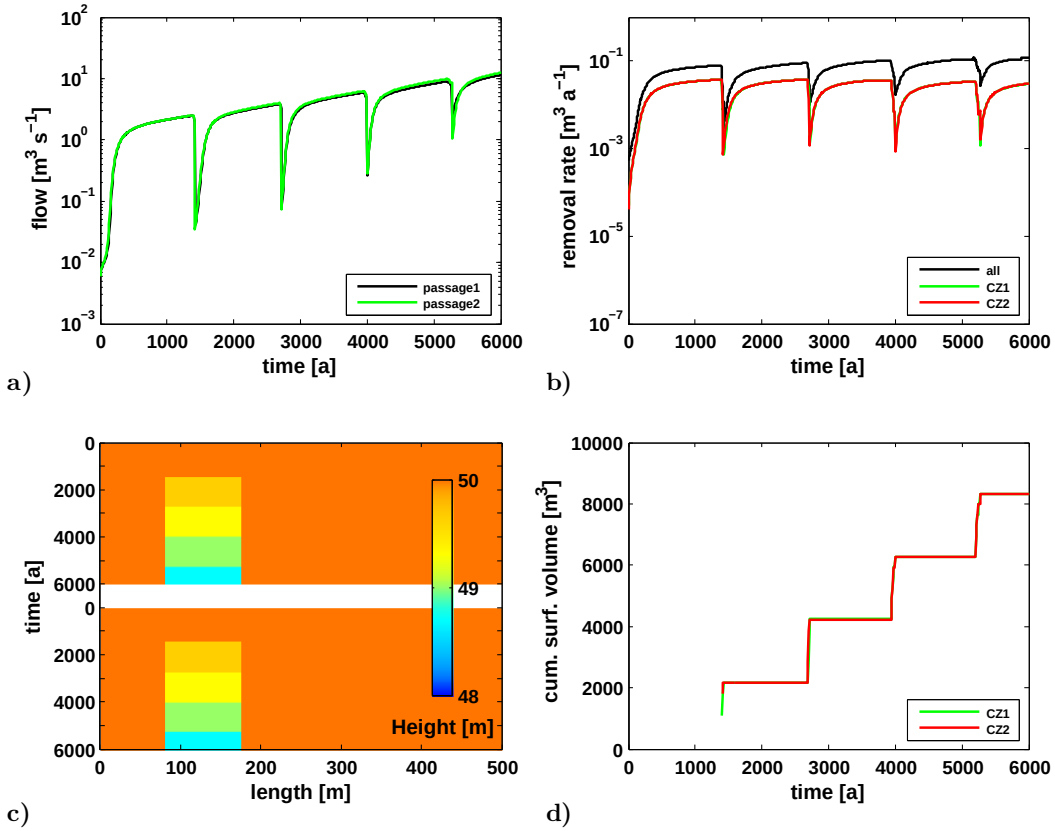


**Fig. 5.23:** Results for 3D doline model 3 (layered collapsing); **a)** flow rates at the output of passage 1 (black) and passage 2 (green); **b)** removed material per year for all conduits (black curve) and only conduits inside crushed zones CZ1 (green) and CZ2 (red); **c)** height *spectra* along surface profiles above passage 1 (top) and passage 2 (bottom) showing the surface lowering over time; **d)** estimated cumulative loss of surface volume for CZ1 (green) and CZ2 (red).

### 5.3.4 Model 4 – two passages, three active crushed zones

Fig. 5.24 shows the setup for model 4. There are again two passages but the number of active crushed zones is increased to three. CZ3 is situated along passage 1 downstream of CZ1. Domain parameters and boundary conditions are again similar to models 1 to 3. The figure showing the relative increase of the conduit diameters can be found in appendix B.3. Here, again only the flux rates are used for describing the domain evolution and only the layered collapsing mechanism is applied.

Due to the interaction of crushed zones CZ1 and CZ3 positioned along passage 1,

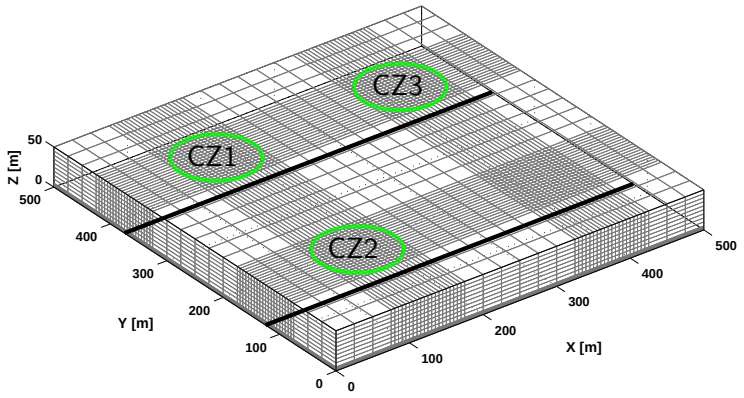


**Fig. 5.24:** Model setup for doline model 4; implemented are two subsurface passages (black lines) and three active crushed zones CZ1,CZ2 and CZ3 (green circles); the green circles also indicate that only conduits inside the circles are treated as crushed zone conduits; for the parameters used see Tab. 5.1.

the evolution of model 4 is more complex compared to the models presented before. Locally, the initial state of the three crushed zones is quite similar. Each crushed zone blocks their corresponding passage and due to the higher conduit diameters inside the crushed zones, compared to the rest of the domain, the flux rates there are one to two orders of magnitude higher. After 300 years of evolution (Fig. 5.25b) the situation is twofold. For passage 2 and crushed zone CZ2 the evolution is comparable to model 2 and 3. After $\approx$ 150 years the local breakthrough event has occurred and high flux rates are established inside the whole crushed zone and along passage 2. The local breakthrough is again clearly visible in Fig. 5.26a (green curve). In contrast to this, higher flux rates are so far only established directly inside passage 1 and along a central region in CZ1. Moderately increased flux rates are also visible in CZ3 but more horizontally spread compared to CZ1. From the head isosurfaces it is clearly visible that inside CZ3 higher gradients have established. Although a central region in CZ1 has evolved, the gradients are so low that the evolution there is much slower compared to CZ3. At first, a local breakthrough occurs in CZ3 and the head gradients are decreasing. Due to the rebounding of the head isosurfaces the gradients inside CZ1 increase and the local breakthrough occurs there too. When the heads are evenly distributed along passage 1 both crushed zones evolve at a constant pace.

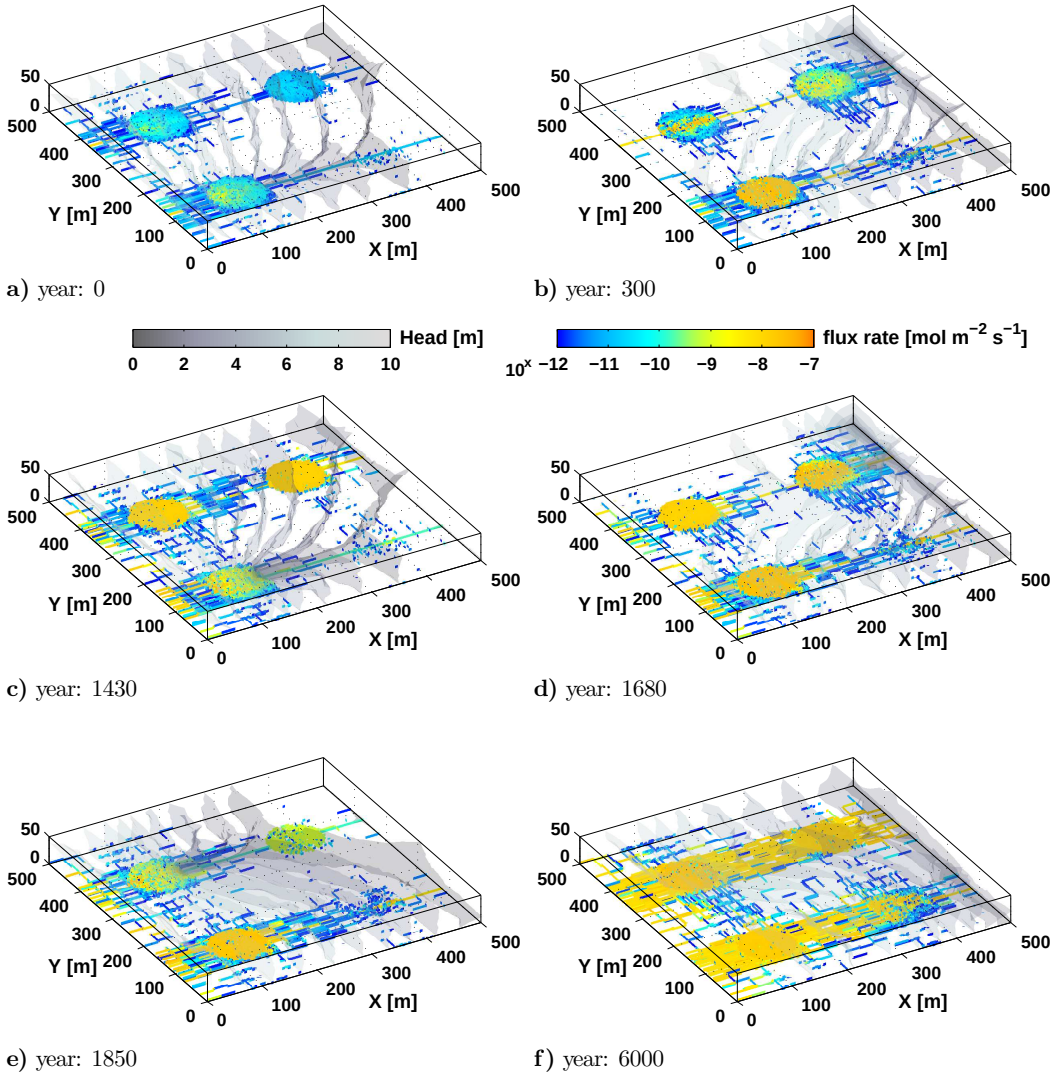


**a)** year: 0 **b)** year: 300

**c)** year: 1430 **d)** year: 1680

**e)** year: 1850 **f)** year: 6000

**Fig. 5.25:** Flux rate evolution of the 3D doline model 4 (layered collapsing) for different snapshots in time; Below each subplot the year is given; plotted are the isosurfaces of constant head from low (dark grey) to high (light grey) values and the flux rates inside the conduit on a log-scale from $10^{-12}$ [mol m$^{-2}$ s$^{-1}$] (blue) to $10^{-7}$ [mol m$^{-2}$ s$^{-1}$] (orange).

Fig. 5.25c shows the evolution after 1430 years. The horizontal layers inside CZ2 have collapsed and passage 2 becomes temporary blocked. Note that every time passage 2 is blocked by a collapse water can flow from passage 1 in direction of passage 2 due to the changed head field. After 1680 years of evolution also the

layers inside CZ3 collapse and passage 1 is blocked there (see Fig. 5.26a – black curve). The reason that CZ3 collapses before CZ1 is due to the initial phase, when higher gradients are established inside CZ3 and therefore the conduit enlargement is accelerated.

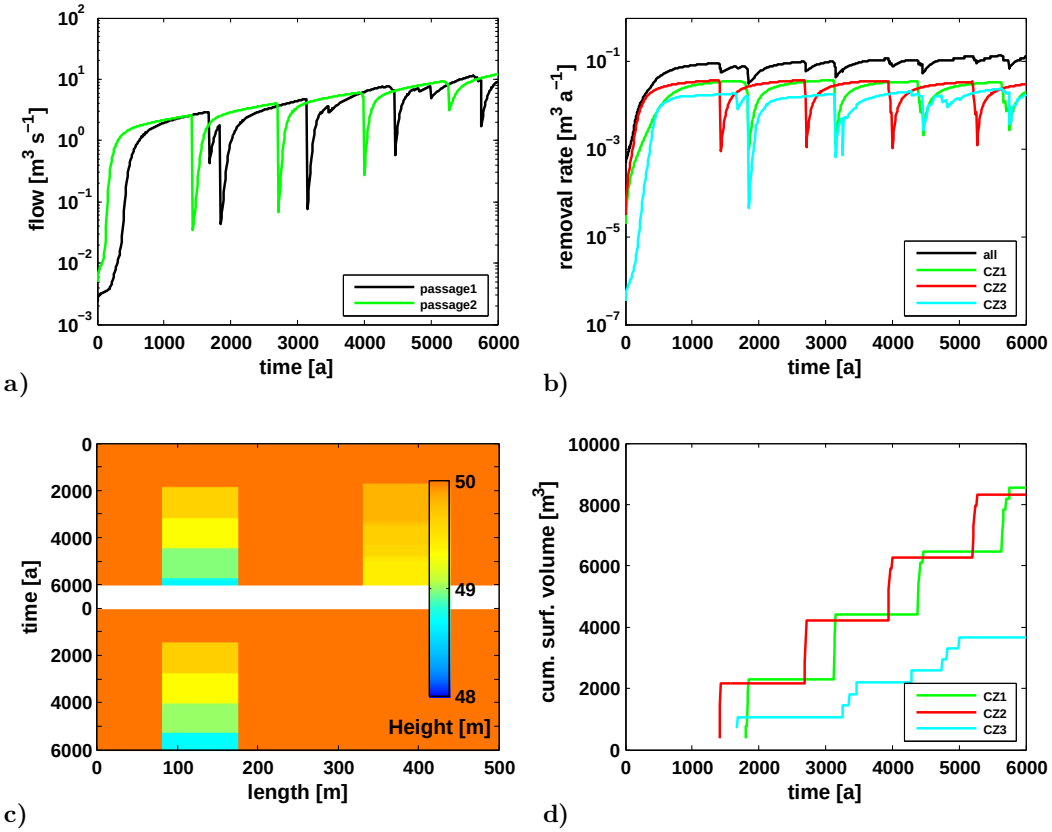


**Fig. 5.26:** Results for 3D doline model 4 (layered collapsing); **a)** flow rates at the output of passage 1 (black) and passage 2 (green); **b)** removed material per year for all conduits (black curve) and only conduits inside crushed zones CZ1 (green), CZ2 (red) and CZ3 (cyan); **c)** height *spectra* along surface profiles above passage 1 (top) and passage 2 (bottom) showing the surface lowering over time; **d)** estimated cumulative loss of surface volume for CZ1 (green), CZ2 (red) and CZ3 (cyan).

The cyan curve in Fig. 5.26d also shows the onset of collapse for CZ3. But in contrast to CZ1 and CZ2 much less material is removed from the surface. This is due to the fact that only the three lowermost layers have collapsed. Only directly after the bottom layer of CZ3 collapses and the passage is blocked, the head gradients

increase and the upper layers of the crushed zone are activated and can evolve. The increase in head gradients can be seen by the distribution of the head isosurfaces in Fig. 5.25d.

After 1850 years of evolution, the layers inside CZ1 collapse (Fig. 5.25e). As here the heads are generally higher due to the boundary condition all layers inside CZ1 collapse and the surface is lowered by almost the same amount as CZ2. Now the gradients inside CZ3 are so small that only the bottom layer is evolving which is also visible in Fig. 5.25e by the small flux rates inside CZ3.

The final stage of this model after 6000 years of evolution is shown in Fig. 5.25f. Material is removed from the crushed zones at high rates, so the system is apparently in between collapse events. Due to the widening of the conduits in between the crushed zones CZ1 and CZ3 and downstream of CZ2 respectively the flux rates are also high there. In contrast to model 3 (Fig. 5.22f) where both passages evolved more or less independently, the region between CZ1 and CZ2 is now more evolved. This may be due to the interaction of both passages caused by their aperiodic blocking. This effect of this aperiodicity is clearly visible in the curves in Fig. 5.26. After 6000 years the surface above CZ1 and CZ2 has lowered to $\approx 48.7$ m, whereas the surface above CZ3 has only lowered to $\approx 49.4$ m due to the less active layers and therefore less often collapsing events.

Also for model 4 an alternative setup was simulated. It is similar to model 3b (B.2.1) where now in model 4b CZ1 and CZ3 are connected and is shown in appendix B.3.1. The results are in a way expected as for model 4b both connected crushed zones act like an elongated single crushed zone. The aperiodicity of the collapsing events is still there but due to the higher heads inside CZ3 all layers can collapse and similar amounts of material compared to CZ1 can be removed.

## 5.4 Conclusions

In this chapter a 3D model for the creation of large collapse dolines was presented. Here, the concept presented by Palmer and Palmer (2006) of a collapsing zone, where local breakdowns of material increase the hydraulic gradients inside a cave passages below an evolving doline was used. The increased gradients lead to an increased dissolution of bedrock material and over time again to a local breakdown. These periodic breakdowns or collapses were simulated with the 3D program

KARSTAQUIFER. A 3D model domain was created containing one or more crushed zones, representing regions of local bedrock collapses. The breakdowns were implemented by resetting the conduit diameters of the conduit network inside the crushed zone to a smaller diameter when a certain critical diameter $d_{crit}$ was reached. By this procedure constant high flux rates were established inside the whole crushed zone. Three different collapsing mechanisms were applied and their effect on the evolution was studied. As all three a rather simple mechanisms, their effect is straightforward in terms of temporal and spatial evolution. The larger the collapsing zone / criteria (blocky, layered and total) the fewer events happen. In future studies of (real) collapse dolines, the mixture of different collapsing mechanisms within one model and the automatic activation of crushed zones over time may enhance the modelling results. With the presented collapsing mechanism the surface lowering inside the doline could be simulated. This collapsing mechanism together with the collapsing parameters could simulate the surface lowering of a doline with a diameter of $\approx$ 100m in the range of $\approx 0.22\,\mathrm{mm\,a^{-1}}$. This rate leads to a collapse doline with 100 m in depth after $\approx$ 460 000 years. This is an acceptable time frame for the creation of a large collapse doline. Note that Dinaric collapse dolines may have formed within in a longer time range, whereas for the large Tiankengs also much shorter creation times are supposed.

Also the interaction of several crushed zones parallel to the major flow direction and / or along one subsurface river was studied. When starting from similar initial conditions, dolines located parallel to the major flow direction (model 3) evolve more or less independently and in a similar way, no matter if they are almost connected or farther away from each other. This effect, however, may be due to the still quite coarse grid discretization and regular grid layout. When a second doline is situated along the same subsurface river then these two dolines show a complex interaction in their evolution. These interaction is characterized by aperiodic collapsing events. Whereas the downstream doline evolves faster up to the first collapsing event, this evolution is slowed down in the advancing simulation. Due to the periodic collapsing of the upstream doline the downstream doline exhibits alternating phases of activity and inactivity due to the changed head field. Also a nearby doline parallel to the major flow direction is effected by this interaction. For this setup, the evolved subsurface conduits between the parallel dolines are more pronounced than without the third downstream doline. This three doline setup (model 4) is clearly the most

interesting one and shows that already in such a basic model setup as presented here, the interaction between dolines appearing in a group can be very complex. The scenarios shown here can easily be extended and used to further study the interaction of groups of collapse dolines especially when considering the constantly increasing computational power.

Like every model also this model has some drawbacks. These are mainly the lack of erosional processes on the bottom of the doline, a correct implementation or estimation of the mechanical properties and so far no climatology influences. Whereas the implementation of some realistic climate data and erosional processes should be a straightforward undertaking, the implementation of correct mechanics could be rather complicated. Nevertheless, this model can be used as a basis for future simulations on the (early) creation of collapse dolines.

# Chapter 6

# Summary & Outlook

This work has shown the development or application respectively of the program KARSTAQUIFER for simulating the evolution of karst aquifer systems in three dimensions under various conditions. The essential findings shall be shortly summarized here.

As the need for a comprehensive understanding of the processes governing the evolution of karst aquifers especially close to dam–sites is obvious, the results presented here are intended to support our understanding of this complex system. Chapter 3 has shown the application of the 3D program for modelling the evolution of karst aquifers beneath dam–sites. Based on a conceptual model, first simple dam–site models have been simulated to understand the influences of several critical parameters on the evolution of the aquifer.

In Chapter 4, the evolution of an aquifer beneath a small dam–site in Switzerland was simulated. As the local bedrock is composed of highly soluble gypsum, the dam–site and the associated change of the aquifer hydraulics has caused severe subsidence of an adjacent highway. The presented model is the first 3D evolution model of a karst aquifer close to a dam–site. The model could show that the dam–site is indeed the major source for the creation of a weathered zone that was identified in the field as the cause for the subsidence. The spatial extent as well as the chemical properties of this weathered zone could be successfully reproduced. Therefore, the model incorporated real topography data, precipitation values from field measurements and realistic boundary conditions. The boundary conditions themselves were constrained by a 3D hydrogeological model and hydraulic head data from well observations. Furthermore, the complex geology of the local bedrock namely the Gipskeuper was successfully implemented by an anisotropic statistical conduit diameter distribution. To give a possible outlook on the evolution of this aquifer a future model for the next 50 years was presented. This model showed that the remedial measures that were carried out to protect the highway can prevent the highway from further subsidence. However, as the dam structure itself may also already be threatened by subsidence the model showed that there is still the potential for the creation of larger voids and fissures below the dam and therefore a risk for this dam–site cannot be excluded.

Finally, in Chapter 5 a natural karst phenomenon that recently has attracted notice by karst scientists working with numerical modelling, has been investigated — large collapse dolines. Especially with a focus on the initial creation of these

large karst surface depressions. The models presented here, simulate the creation of large collapse dolines in limestone bedrock by breakdown events in a mechanically weak zone named here *crushed zone*. These breakdowns ensure that a subsurface river or passage, a necessary criteria for the development of large collapse dolines, is effectively blocked and the local hydraulic head is increased. Furthermore, the breakdown ensures that high dissolution rates are established inside the crushed zone over the entire calculation time. In addition, the interaction of spatially distributed dolines (crushed zones) was investigated and presented. It was shown that, if connected via the same subsurface river two dolines interact in a way, that parts of the downstream doline become periodically active or inactive respectively. This is especially interesting when considering the fact that it is not unlikely to find large collapse dolines occurring in groups in nature and that they are bound to the same karst system. Also simulated by the breakdown or collapsing events was the surface lowering over time. Even if mechanically not correct reasonable lowering rates could be estimated.

The presented modelling studies have shown the large capabilities of the 3D program KARSTAQUIFER and the possibility of its application to a wide range of problems occurring in karst science. It was shown that nowadays were computational power is widely accessible, large and complex three dimensional karst evolution models can be treated. The focus in the interesting field of numerical modelling can be shifted to several topics in future development. As nature can of course be arbitrarily complex it may be advantageous to implement irregular finite element grids and networks. Therewith it is possible to model and focus on complex geometries with high resolution without loosing the ability to model large scale domains. This would be essentially helpful regarding man–made structures in karst. From a process–based perspective the implementation of dissolution inside the matrix and not only along discrete fractures / conduits and their combined interactions is an approach worth to pursue. Furthermore, the complete integration of the vadose zone and the karst processes there, would allow modelling an additional wide range of natural karst systems.

I hope that this work can be taken as one *stepping stone* for future numerical studies of complex karst systems in three dimensions.

# Bibliography


Amestoy, P.R., Duff, I.S., Koster, J. and L'Excellent, J.Y. A fully asynchronous multifrontal solver using distributed dynamic scheduling. *SIAM Journal of Matrix Analysis and Applications*, 23(1): 15–41, 2001.

Amestoy, P.R., Guermouche, A. and L'Excellent, J.Y. Hybrid scheduling for the parallel solution of linear systems. *Parallel Computing*, 32(2): 136–156, 2006.

Annable, W.K. *Numerical Analysis of Conduit Evolution in Karst Aquifers*. Ph.D. thesis, University of Waterloo, Ontario, Canada., 2003.

Bauer, S., Liedl, R. and Sauter, M. Modelling of karst genesis at the catchment scale - influence of spatially variable hydraulic conductivity. *Acta Geologica Polonica*, 52(1): 13–21, 2002.

Bauer, S., Liedl, R. and Sauter, M. Modeling of karst aquifer genesis: Influence of exchange flow. *Water Resources Research*, 39(10): 1285, 2003. doi:10.1029/2003WR002218.

Bauke, H. and Mertens, S. *Cluster Computing*. X.systems.press. Springer Berlin, Heidelberg, New York, 2006.

Beek, W.J. and Muttzall, K.M.K. *Transport Phenomena*. John Wiley & Sons, 1975.

Bögli, A. *Karst Hydrology and Physical Speleology*. Springer New York, 1980.

Bonacci, O., Gottstein, S. and Roje-Bonacci, T. Negative impacts of grouting on the underground karst environment. *Ecohydrology*, 2: 492–502, 2009. doi:10.1002/eco.90.

Bonacci, O. and Josip, R. Water losses from a reservoir built in karst: the example of the Boljunčica reservoir (Istria, Croatia). *Environmental Geology*, 58: 339–345, 2009. doi:10.1007/s00254-008-1599-z.

Buhmann, D. and Dreybrodt, W. The kinetics of calcite dissolution and precipitation in geologically relevant situations of karst areas: 1. Open system. *Chemical Geology*, 48(1–4): 189–211, 1985a. doi:10.1016/0009-2541(85)90046-4.

Buhmann, D. and Dreybrodt, W. The kinetics of calcite dissolution and precipitation in geologically relevant situations of karst areas: 2. Closed system. *Chemical Geology*, 53(1–2): 109–124, 1985b. doi:10.1016/0009-2541(85)90024-5.

Deutsch, C.V. and Journel, A.G. *GSLIB: Geostatistical Software Library and User's Guide*. Oxford University Press, 1997.

DeWaele, J. Interaction between a dam site and karst springs: The case of Supramonte (Central-East Sardinia, Italy). *Engineering Geology*, 99: 128–137, 2008. doi:10.1016/j.enggeo.2007.11.010.

Dreybrodt, W., Laukner, J., Zaihua, L., Svensson, U. and Buhmann, D. The kinetics of the reaction $CO_2 + H_2O + H^+ + HCO_3^-$ as one of the rate limiting steps for the dissolution of calcite in the system $H_2O - CO_2 - CaCO_3$. *Geochimica et Cosmochimica Acta*, 60(18): 3375–3381, 1996. doi:10.1016/0016-7037(96)00181-0.

Dreybrodt, W. *Processes in karst systems - Physics, Chemistry and Geology*. Springer Series in Physical Environments 4. Springer Berlin, New York, 1988.

Dreybrodt, W. The Role of Dissolution Kinetics in the Development of Karst Aquifers in Limestone: A Model Simulation of Karst Evolution. *The Journal of Geology*, 98(5): 639–655, 1990. doi:doi:10.1086/629431.

Dreybrodt, W. Dynamics of karstification: A model applied to hydraulic structures in karst terranes. *Applied Hydrogeology*, 1(3): 20–32, 1992.

Dreybrodt, W. Principles of Early Development of Karst Conduits Under Natural and Man-Made Conditions Revealed by Mathematical Analysis of Numerical Models. *Water Resources Research*, 32(9): 2923–2935, 1996.

Dreybrodt, W. and Gabrovšek, F. Dynamics of the evolution of single karst conduits. In A.B. Klimchouk, D.C. Ford, A.N. Palmer and W. Dreybrodt (editors),

*Speleogenesis: Evolution of Karst Aquifers*, pp. 184–193. National Speleological Society, New York, 2000.

Dreybrodt, W., Gabrovšek, F. and Romanov, D. *Processes of Speleogenesis: A Modeling Approach*. Carsologica. Založba ZRC, 4 edition, 2005.

Eisenlohr, L., Meteva, K., Gabrovšek, F. and Dreybrodt, W. The inhibiting action of intrinsic impurities in natural calcium carbonate minerals to their dissolution kinetics in aqueous $H_2O - CO_2$ solutions. *Geochimica et Cosmochimica Acta*, 63(7–8): 989–1001, 1999. doi:10.1016/S0016-7037(98)00301-9.

Epting, J., Huggenberger, P. and Glur, L. Integrated investigations of karst phenomena in urban environments. *Engineering Geology*, 109(3–4): 273–289, 2009a. doi:10.1016/j.enggeo.2009.08.013.

Epting, J., Romanov, D., Huggenberger, P. and Kaufmann, G. Integrating field and numerical modeling methods for applied urban karst hydrogeology. *Hydrology and Earth System Sciences*, 13(7): 1163–1184, 2009b.

Epting, J., Wüest, A. and Huggeberger, P. Investigating sediments and rock structures beneath a river using underwater ERT. *Central European Journal of Geosciences*, 4(1): 81–93, 2012. doi:10.2478/s13533-011-0052-0.

Farr, T.G., Rosen, P.A., Caro, E., Crippen, R., Duren, R., Hensley, S., Kobrick, M., Paller, M., Rodriguez, E., Roth, L., Seal, D., Shaffer, S., Shimada, J., Umland, J., Werner, M., Oskin, M., Burbank, D. and Alsdorf, D. The Shuttle Radar Topography Mission. *Reviews of Geophysics*, 45: RG2004, 2007. doi:10.1029/2005RG000183.

Ford, D.C. and Williams, P. *Karst Hydrogeology and Geomorphology*. Wiley Publishing Inc., 2007.

Gabrovšek, F. *Evolution of Early Karst Aquifers: From simple principles to complex models*. Ph.D. thesis, University of Bremen, 2000.

Gabrovšek, F. and Dreybrodt, W. Role of Mixing Corrosion in Calcite-Aggressive $H_2O - CO_2 - CaCO_3$ Solutions in the Early Evolution of Karst Aquifers in Limestone. *Water Resources Research*, 36(5): 1179–1188, 2000.

Gabrovšek, F. and Dreybrodt, W. A model of the early evolution of karst aquifers in limestone in the dimensions of length and depth. *Journal of Hydrology*, 240(3–4): 206–224, 2001. doi:doi:10.1016/S0022-1694(00)00323-1.

Gabrovšek, F. and Dreybrodt, W. Karstification in unconfined limestone aquifers by mixing of phreatic water with surface water from a local input: A model. *Journal of Hydrology*, 386(1–4): 130–141, 2010. doi:doi:10.1016/j.jhydrol.2010.03.015.

Gabrovšek, F., Romanov, D. and Dreybrodt, W. Early karstification in a dual-fracture aquifer: the role of exchange flow between prominant fractures and a dense net of fissures. *Journal of Hydrology*, 299(1–2): 45–66, 2004. doi:doi:10.1016/j.jhydrol.2004.02.005.

Gabrovšek, F. and Stepišnik, U. On the formation of collapse dolines: A modelling perspective. *Geomorphology*, 134: 23–31, 2011. doi:10.1016/j.geomorph.2011.06.007.

Golder, E. (editor). *100 Jahre Birswuhr Neue Welt. Die Geschichte eines Bauwerkes.* Baudepartement Basel - Stadt, 1984.

Gould, N.I.M., Hu, Y. and Scott, J.A. A numerical evaluation of sparse direct solvers for the solution of large sparse, symmetric linear systems of equations. Technical Report RAL-TR-2005-005, Council for the Central Laboratory of the Research Councils, 2005. URL `ftp://ftp.numerical.rl.ac.uk/pub/reports/ghsRAL200505.pdf`.

Groves, C.G. and Howard, A.D. Early development of karst systems 1. Preferential flow path enlargement under laminar flow. *Water Resources Research*, 30(10): 2837–2846, 1994a.

Groves, C.G. and Howard, A.D. Minimum hydrochemical conditions allowing limestone cave development. *Water Resources Research*, 30(3): 607–615, 1994b.

Hanna, R.B. and Rajaram, H. Influence of aperture variability on dissolutional growth of fissures in karst formations. *Water Resources Research*, 34(11): 2843–2853, 1998.

Hiller, T., Kaufmann, G. and Romanov, D. Karstification beneath dam–sites: From conceptual models to realistic scenarios. *Journal of Hydrology*, 398: 202–211, 2011. doi:10.1016/j.jhydrol.2010.12.014.

Hiller, T., Kaufmann, G., Romanov, D. and Gabrovšek, F. Formation of large collapse dolines: A three-dimensional numerical perspective. In *Proceedings of the EGU General Assembly – Vienna*. 2012a.

Hiller, T., Romanov, D., Kaufmann, G., Epting, J. and Huggeberger, P. Karstification beneath the Birs weir in Basel/Switzerland: A 3D modeling approach. *Journal of Hydrology*, 2012b. doi:http://dx.doi.org/10.1016/j.jhydrol.2012.04.040.

Howard, A.D. and Groves, C.G. Early development of karst systems 2. Turbulent flow. *Water Resources Research*, 31(1): 19–26, 1995.

Huyakorn, P.S., Lester, B.H. and Faust, C.R. Finite element techniques for modeling groundwater flow in fractured aquifers. *Water Resources Research*, 19(4): 1019–1035, 1983.

Istok, J.D. *Groundwater Modeling by the Finite Element Method*. American Geophysical Union, 1989.

Jeschke, A.A., Vosbeck, K. and Dreybrodt, W. Surface controlled dissolution rates of gypsum in aqueous solutions exhibit nonlinear dissolution kinetics. *Geochimica et Cosmochimica Acta*, 65(1): 27–34, 2001. doi:10.1016/S0016-7037(00)00510-X.

Johnson, K.S. Gypsum-karst problems in constructing dams in the usa. *Environmental Geology*, 53: 945–950, 2008. doi:10.1007/s00254-007-0720-z.

Karimi, H., Keshavarz, T., Mohammadi, Z. and Raeisi, E. Potential leakage at the Khersan 3 Dam Site, Iran: a hydrogeological approach. *Bulletin of Engineering Geology and the Environment*, 66(3): 269–278, 2007. doi:10.1007/s10064-006-0079-5.

Kaufmann, G. Karst aquifer evolution in a changing water table environment. *Water Resources Research*, 38(6): 26–1–26–9, 2002. doi:10.1029/2001WR000256.

Kaufmann, G. A model comparison of karst aquifer evolution for different matrix-flow formulations. *Journal of Hydrology*, 283(1–4): 281–289, 2003a. doi:10.1016/S0022-1694(03)00270-1.

Kaufmann, G. Modelling unsaturated flow in an evolving karst aquifer. *Journal of Hydrology*, 276(1–4): 53–70, 2003b. doi:10.1016/S0022-1694(03)00037-4.

Kaufmann, G. Numerical models for mixing corrosion in natural and artificial karst environments. *Water Resources Research*, 39(6): 1157, 2003c. doi: 10.1029/2002WR001707.

Kaufmann, G. Structure and evolution of karst aquifers: a finite-element numerical modelling approach. In W. Dreybrodt, F. Gabrovšek and D. Romanov (editors), *Processes of Speleogenesis: A modeling Approach*, pp. 323–371. Karst Research Institute, ZRZ SAZU, Postojna, Slovenia, 2005.

Kaufmann, G. Modelling karst geomorphology on different time scales. *Geomorphology*, 106(1–2): 62–77, 2009. doi:10.1016/j.geomorph.2008.09.016.

Kaufmann, G. and Braun, J. Karst aquifer evolution in fractured rocks. *Water Resources Research*, 35(11): 3223–3228, 1999.

Kaufmann, G. and Braun, J. Karst aquifer evolution in fractured, porous rocks. *Water Resources Research*, 36(6): 1381–1391, 2000.

Kaufmann, G. and Dreybrodt, W. Calcite dissolution kinetics in the system $CaCO_3 - H_2O - CO_2$ at high undersaturation. *Geochimica et Cosmochimica Acta*, 71(6): 1398–1410, 2007. doi:10.1016/j.gca.2006.10.024.

Kaufmann, G. and Romanov, D. Cave development in the Swabian Alb, south-west Germany: A numerical perspective. *Journal of Hydrology*, 349(3–4): 302–317, 2008. doi:10.1016/j.jhydrol.2007.11.019.

Kaufmann, G., Romanov, D. and Hiller, T. Modeling three-dimensional karst aquifer evolution using different matrix-flow contributions. *Journal of Hydrology*, 388(3–4): 241–250, 2010. doi:10.1016/j.jhydrol.2010.05.001.

Kranjc, A. Some large dolines in the Dinaric karst. *Speleogenesis and Evolution of Karst Aquifers*, 4(1): p. 4, 2006.

Malkawi, A.I.H. and Al-Sheriadeh, M. Evaluation and rehabilitation of dam seepage problems. A case study: Kafrein dam. *Engineering Geology*, 56(3–4): 335–345, 2000. doi:10.1016/S0013-7952(99)00117-9.

Milanović, P.T. *Geological Engineering in Karst.* Zebra Publishing, Belgrade, Yugoslavia, 2000.

Milanović, P.T. *Water resources engineering in karst*. CRC Press, 2004. Taylor & Francis, London.

Mohammadi, Z. and Raeisi, E. Hydrological uncertainties in delineation of leakage at karst dam sites, the Zagros region, Iran. *Journal of Cave and Karst Studies*, 69(3): 305–317, 2007.

NAGRA. Project Opalinuston: Syntheses of geoscientific investigation results. 2002. NTB: 02-03.

Palmer, A. Origin and morphology of limestone caves. *Geological Society of America Bulletin*, 103(1): 1–21, 1991. doi:10.1130/0016-7606(1991)103⟨0001:OAMOLC⟩2.3.CO;2.

Palmer, A.N. and Palmer, M.V. Hydraulic processes in the origin of tiankengs. *Speleogenesis and Evolution of Karst Aquifers*, 4(1): 1–8, 2006.

Plummer, L.N., Wigley, T.M.L. and Parkhurst, D.L. The kinetics of calcite dissolution in $CO_2$-water systems at $5°C$ to $60°C$ and 0.0 to 1.0 atm $CO_2$. *American Journal of Science*, 278: 179–216, 1978.

Raines, T.W. Sótano de las Golondrinas. *Bulletin of the Association for Mexican Cave Studies*, 2: 1–37, 1967.

Romanov, D., Dreybrodt, W. and Gabrovšek, F. Interaction of Fracture and Conduit Flow in the Evolution of Karst Aquifers. *Speleogenesis and Evolution of Karst Aquifers*, pp. 1–6, 2003a.

Romanov, D., Gabrovšek, F. and Dreybrodt, W. Dam sites in soluble rocks: a model of increasing leakage by dissolutional widening of fractures beneath a dam. *Engineering Geology*, 70(1–2): 17–35, 2003b. doi:10.1016/S0013-7952(03)00073-5.

Romanov, D., Gabrovšek, F. and Dreybrodt, W. The impact of hydrochemical boundary conditions on the evolution of limestone karst aquifers. *Journal of Hydrology*, 276(1–4): 240–253, 2003c. doi:10.1016/S0022-1694(03)00058-1.

Romanov, D., Kaufmann, G. and Hiller, T. Karstification of aquifers interspersed with non-soluble rocks: Fom basic principles towards case studies. *Engineering Geology*, 116(3–4): 261–273, 2010. doi:10.1016/j.enggeo.2010.09.008.

Romanov, D., Kaufmann, G., Hiller, T., Epting, J. and Huggenberger, P. Karstification of an aquifer along the Birs river, Switzerland - a modeling approach. *Engineering Geology*, 2012. doi:http://dx.doi.org/10.1016/j.enggeo.2012.04.009.

Schenk, O. and Gärtner, K. Solving Unsymmetric Sparse Systems of Linear Equations with PARDISO. *Journal of Future Generation Computer Systems*, 20(3): 475–487, 2004. doi:10.1016/j.future.2003.07.011.

Schenk, O. and Gärtner, K. On fast factorization pivoting methods for symmetric indefinite systems. *Electronic Transactions on Numerical Analysis*, 23: 158–179, 2006.

Siemers, J. and Dreybrodt, W. Early development of karst aquifers on percolation networks of fractures in limestone. *Water Resources Research*, 34(3): 409–419, 1998.

Svensson, U. and Dreybrodt, W. Dissolution kinetics of natural calcite minerals in $CO_2$-water systems approaching calcite equilibrium. *Chemical Geology*, 100(1–2): 129–145, 1992. doi:10.1016/0009-2541(92)90106-F.

Unal, B., Eren, M. and Yalcin, M.G. Investigation of leakage at Ataturk dam and hydroelectric power plant by means of hydrometric measurements. *Engineering Geology*, 93(1–2): 45–63, 2007. doi:10.1016/j.enggeo.2007.02.006.

Waltham, T. Tiankengs of the world, outside China. *Speleogenesis and Evolution of Karst Aquifers*, 4(1): p. 12, 2006.

Waltham, T., Bell, F.G. and Culshaw, M.G. *Sinkholes and Subsidence*. Springer Berlin, Heidelberg, New York, 2005.

Zhu, X. and Chen, W. Tiangenks in the karst of China. *Speleogenesis and Evolution of Karst Aquifers*, 4(1): p. 18, 2006.

Zhu, X. and Waltham, T. Tiangenk: definition and description. *Speleogenesis and Evolution of Karst Aquifers*, 4(1): p. 8, 2006.

# List of Figures

# List of Tables

# List of Publications

## First Author

Hiller, T., Kaufmann, G. and Romanov, D., Epting, J. and Huggenberger, P., 2012, Karstification beneath the Birs weir in Basel/Switzerland: A 3D modeling approach, *Journal of Hydrology*, doi:10.1016/j.jhydrol.2012.04.040.

Hiller, T., Kaufmann, G., Romanov, D., Gabrovšek, F., 2012, Formation of large collapse dolines: A three–dimensional numerical perspective, *in prep.*

Hiller, T., Kaufmann, G. and Romanov, D., 2011, Karstification beneath dam–sites: From conceptual models to realistic scenarios, *Journal of Hydrology*, **398**, 202-211, doi:10.1016/j.jhydrol.2010.12.014.

## Co–author

Romanov, D., Kaufmann, G., Hiller, T., Epting, J., Huggenberger, P., 2012 Karstification of an aquifer along the Birs river, Switzerland – a modeling approach, *Engineering Geology*, doi:10.1016/j.enggeo.2012.04.009.

Müller-Petke, M., Hiller, T., Hermann, R. and Yaramanci, U., 2011. Reliability and limitations of surface NMR assessed by comparison to borehole NMR *Near Surface Geophysics*, **9**, 123-134, doi:10.3997/1873-0604.2010066.

Kaufmann, G., Romanov, D. and Hiller, T., 2010. Modeling three–dimensional karst aquifer evolution using different matrix–flow contributions *Journal of Hydrology*, **388**, 241-250, doi:10.1016/j.jhydrol.2010.05.001.

Romanov, D., Kaufmann, G. and Hiller, T., 2010. Karstification of aquifers interspersed with non-soluble rocks: From basic principles towards case studies *Engineering Geology*, **116**, 261-273, doi:10.1016/j.enggeo.2010.09.008.

## Conference Proceedings (selected)

Hiller, T., Kaufmann, G., Romanov, D., Gabrovšek, F., 2012, Formation of large collapse dolines: A three–dimensional numerical perspective, *Proceedings of the 2012 EGU General Assembly – Vienna, Austria.*

Hiller, T., Kaufmann, G., Romanov, D., Epting, J. and Huggenberger, P., 2011. Karstification beneath the Birs weir in Basel/Switzerland: A 3D modelling approach, *Proceedings of the 2011 EGU General Assembly – Vienna, Austria.*

Hiller, T., Kaufmann, G. and Romanov, D., 2010. Karstification beneath dam–sites: From conceptual models to realistic scenarios, *Proceedings of the 2010 EGU General Assembly – Vienna, Austria.*

Hiller, T., Yaramanci, U. and Delhomme, J.P., 2008. Joint Interpretation of Magnetic Resonance Sounding and borehole NMR data, Proceedings of EAGE's Near Surface 2008 Meeting – Krakow, Poland.

Hiller, T., Yaramanci, U. and Delhomme, J.P., 2008. Gemeinsame Interpretation von Magnetischer Resonanz Sondierung und NMR-Bohrloch Daten, *68. Jahrestagung der Deutschen Geophysikalischen Gesellschaft 2008 – Freiberg, Deutschland.*

# Acknowledgement

At this point I would like to thank a few people.

First of all, of course my colleagues at the FU Berlin, Prof. Kaufmann and Douchko Romanov. I have to thank them both for introducing me the interesting field of karst science in all its different facets. In particular I like to thank Prof. Kaufmann for giving me the opportunity to write my phd–thesis and to always encourage me, especially in times when things did not seem to work out well. A very big thanks goes out to Douchko for his patience, the endless discussions about science and beyond and most of all for his sense of humor. I felt very welcome in our small group and really appreciate this.

I like to thank Franci Gabrovšek for also supervising this thesis but especially for his hospitality during our stay in Slovenia. I really enjoyed the time there and will never forget the trips through these impressive caves.

A big thank you goes out to the students in our group, especially Ron and Grit. The time in the institute during your diploma thesis' and the field campaigns, especially the one in Syria, can only be described by one word: hammmmmmmmmmmmmmmmmmmmmmer. Thanks guys.

A very special thanks goes out to my family who always believed in me and granted me with their unconditional support.

Anna. What can I say? Throughout the last years you kept me and my craziness on the ground. One thank you would not be enough.

# Appendix A

# Technical aspects of 3D karst evolution modelling

One aspect that has to be considered in 3D modelling is the performance of the available simulation program. The program has to be able to handle large models in an acceptable time. For karst evolution modelling the possible limitations in terms of needed computational effort are twofold. The first one deals with a typical aspect of finite element modelling, the solution of *large sparse matrices*. Therefore, two well known and established solver routines (PARDISO and MUMPS) are tested and benchmarked on different hardware platforms. The second one is implicitly given by the dissolution process. The *dissolution has to be calculated sequentially* for every single conduit due to the transport of the dissolved material. Thereby, the calculation of the dissolution has also a significant influence on the overall computational performance. Both effects are discussed here.

## A.1 On the performance of KARSTAQUIFER

To estimate the general performance of KARSTAQUIFER the main steps for simulating a karst evolution model need to be reconsidered (see 2.2). These are

1. Reading the input data & Initialization (finite element grid, parameters, etc.)
2. Assembling & solving the system of equations (large sparse matrices) to get the hydraulic heads
3. Apply the dissolution process (flow rate $\rightarrow$ flux rate $\rightarrow$ increase diameter $\rightarrow$ transport)
4. Saving results.

Point 1 needs only to be done once when starting the simulation. For a saturated groundwater flow model point 2 needs to be done at least once in every time step. Depending on the applied solving routine this process can be parallelized. When turbulence is activated and / or an unsaturated groundwater flow model is considered, point 2 has to be performed several times per time step until convergence is reached. Therefore, the simulation may benefit from parallelization. The dissolutional conduit widening in point 3 is per default a sequential process and can not be parallelized. It also needs to be performed in every time step. Depending on the simulated karst evolution model it may be possible to save the results (point 4) less frequent than every time step. For instance for a natural karstification model that

simulates several hundred thousand of years of evolution the data could be saved every 500 or 1000 time steps.

So the two crucial parts when performing karst evolution modelling are solving the linear system of equations (parallel) and conduit dissolution (sequential) respectively. Their impact on the simulation is shown in the next sections.

### A.1.1 Model size vs. calculation time

First, the overall performance of KARSTAQUIFER is tested on different hardware platforms (see Tab. A.1). These are a normal desktop computer with an AMD Athlon X2 processor, a workstation with an AMD Opteron processor and a computer cluster based on Intel Xeon processors. To estimate the dependency of the computation time on the grid discretization, several models were generated. For a list of the models see Tab. A.2.

| **Platform** | **CPU** | **No. of cores** | **Main memory - RAM** |
|---|---|---|---|
| Desktop Computer - PC | AMD Athlon X2 | 2 | 3 GB |
| Workstation - WS | AMD Opteron | 2 | 8 GB |
| Server - SRV | Intel Xeon | 8 | 8 GB |
| Cluster - CLU (24 nodes) | Intel Xeon | 192 | 192 GB |

**Table A.1:** Hardware platforms

For all models the number of nodes in $x$, $y$ and $z$ direction are given. Furthermore, the corresponding number of total grid nodes $N_n$, number of parallelepipedal elements $N_e$ and number of conduits $N_c$ are given. In the last column of Tab. A.2 the number of non–zeros $NNZ$ in the global element matrix is given as this is a measure for the sparsity of the problem. As the first models a rather small only one node of the computer cluster is used (SRV in Tab. A.1). Generally, it is expected due to the sequential nature of any karst evolution model that also for KARSTAQUIFER the calculation time depends mainly on the processor clock. For a first comparison the sequential version of the PARDISO solver was used. As the computer cluster was not used for this test model12 and model13 had to be excluded due to insufficient memory.

Fig. A.1 shows the results for this first test for model1 to model11. In Fig. A.1a the needed disk space for saving the data of one time step is shown as a function of grid nodes. In Fig. A.1b the corresponding calculation time is shown for the desktop computer (PC – blue line), the Workstation (WS – black line) and one

| **Name** | $nx$ | $ny$ | $nz$ | $N_n$ | $N_e$ | $N_c$ | $NNZ$ ([%]) |
|---|---|---|---|---|---|---|---|
| model1 | 13 | 7 | 7 | 637 | 432 | 1 680 | 13 357 (3.292) |
| model2 | 17 | 9 | 9 | 1 377 | 1 024 | 3 744 | 30 625 (1.615) |
| model3 | 21 | 11 | 11 | 1 541 | 2 000 | 7 040 | 58 621 (0.908) |
| model4 | 25 | 13 | 13 | 4 225 | 3 456 | 11 856 | 99 937 (0.560) |
| model5 | 31 | 16 | 16 | 7 936 | 6 750 | 22 560 | 192 556 (0.306) |
| model6 | 41 | 21 | 21 | 18 081 | 16 000 | 52 080 | 450 241 (0.138) |
| model7 | 61 | 31 | 31 | 58 621 | 54 000 | 171 120 | 1 498 861 (0.044) |
| model8 | 81 | 41 | 41 | 136 161 | 128 000 | 400 160 | 3 528 481 (0.019) |
| model9 | 101 | 51 | 51 | 262 701 | 250 000 | 775 200 | 6 863 101 (0.010) |
| model10 | 101 | 61 | 61 | 375 821 | 360 000 | 1 111 420 | 9 861 061 (0.007) |
| model11 | 121 | 61 | 61 | 450 241 | 432 000 | 1 332 240 | 11 826 721 (0.006) |
| model12 | 121 | 61 | 76 | 560 956 | 540 000 | 1 661 655 | 14 767 066 (0.005) |
| model13 | 121 | 76 | 76 | 698 896 | 675 000 | 2 072 520 | 18 438 436 (0.004) |

**Table A.2:** Models used for KARSTAQUIFER performance tests; $nx$, $ny$, $nz$ number of nodes in $x$, $y$, $z$ direction; $N_n$ total number of nodes; $N_e$ total number of parallelepipedal elements; $N_c$ number of conduits; $NNZ$ number of non–zeros in global element matrix (percentage)

server (node) of the computer cluster (SRV – green line). Note that the axes in both plots are logarithmically scaled. For very small model sizes (model1 to model5) the disk space as well as the calculation time does not exceed 10 [MB] and 10 [s] respectively. The required disk space increases linearly up to 340 [MB] for model11. For the calculation time a similar behaviour can be observed. The calculation time for one time step increases more than linearly with increasing nodes. The hardware platform also has a significant effect on the calculation time. The PC has for all models the longest calculation time and could only be used up to model8 due to insufficient memory (see. Tab. A.1). The workstation is for all models a factor of $\approx 1.2$ faster than the PC and needs $\approx 18$ minutes for one time step of model11. The server performs even better and is for bigger models ($\geq$ model8) more than 1.5 times faster than the workstation. The difference between server and workstation increases with increasing model size and model11 only takes $\approx 10$ minutes.

The dashed vertical lines in Fig. A.1a+b mark the range where model size, required disk space and calculation time are sufficiently balanced and have been applied in this work. Whereas the calculation time for large model sizes may be in an acceptable range (1000 time steps for model11 take $\approx 1$ week), the corresponding required disk space is impractically high ($\approx$ 330GB).

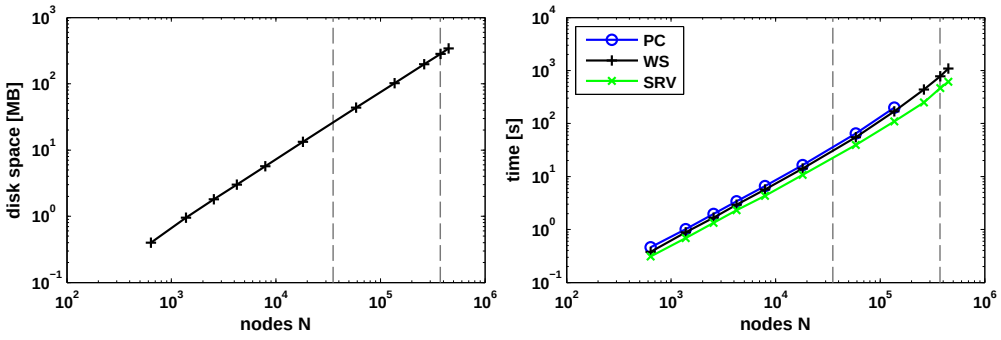


**a)** disk space for one time step $\Delta t$ **b)** calculation time for one time step $\Delta t$

**Fig. A.1:** **a)** disk space for storing simulation results as a function of model size; **b)** calculation time as a function of model size for three different hardware platforms

### A.1.2 Influence of the sparse solvers

#### A.1.2.1 Solving the linear system of equations

To determine the hydraulic heads the sparse system of equations $Ax = b$ based on 2.18 has to be solved. As $A$ and $b$ are given the solution $x$ (head) needs to be found. This can either be done by a direct method or an iterative method, respectively. Generally, the use of direct methods is preferred as they don't need preconditioning prior to solving, which can be computationally expensive. For an overview on available direct solvers see e.g. Gould et al. (2005). Generally, all direct methods apply the following routines:

1. Ordering that exploits the sparsity structure of the matrix $A$ to determine a pivot sequence.
2. Analysis / symbolic factorization that uses the pivot sequence to establish the data structures for factorization.
3. Numerical factorization of $A$ into upper and lower triangular matrices $A = LU$ where $U = L^T$.
4. Solving by forward elimination $Ly = b$ and backward substitution $Ux = y$.

In this list the numerical factorization is the computationally most expensive one. For this study, the two well established sparse solvers PARDISO and MUMPS[1] are

[1] **Mu**ltifrontal **M**assively **P**arallel **S**olver

tested. PARDISO by Schenk and Gärtner (2004, 2006) is a shared–memory multiprocessing parallel direct sparse solver that uses a combination of left– and right–looking for factorization. MUMPS by Amestoy et al. (2001, 2006) was originally designed for distributed–memory computers (clusters) and uses a multifrontal approach for factorization. For a detailed description of the algorithms implemented by the solvers the reader is referred to the given references. The *benchmark tests* done here are rather to get an idea on the overall computation requirements for KARSTAQUIFER than to intensively compare both solvers against each other. For performance tests of several direct solvers the reader is referred to Gould et al. (2005) and the references therein.

#### A.1.2.2 Parallelizing the solving routine

Now the effect of parallelizing the matrix solving routine is examined. In a next step the two matrix solvers are tested.

First the parallel fraction of the program KARSTAQUIFER needs to be determined. In theory this can be done by the use of Amdahl's law (Bauke and Mertens, 2006)

$$1 = S + P, \tag{A.1}$$

where $S$ is the sequential fraction of a program that cannot be parallelized and $P$ is the parallel fraction respectively. Then the speedup $SU$ achieved by parallelization is

$$SU = \frac{1}{S + \frac{P}{N}} \leq \frac{1}{S}, \tag{A.2}$$

with $N$ the number of processors used for the parallel fraction. It is clear from A.2 that the speedup is limited by the sequential fraction of the program and cannot exceed $1/S$, no matter how many processors are used. Furthermore, A.2 is of course highly idealized as the term $P/N$ cannot become zero in reality. Actually, for a given program with a given parallel fraction the speedup decreases again with increasing $N$. This is due to the produced overhead from interprocess communication and data transfer. Therefore A.2 extends to

$$SU = \frac{1}{S + \frac{P}{N} + \Theta(N)} \leq \frac{1}{S}, \tag{A.3}$$

where $\Theta(N)$ is a linear function depending on the number of processors $N$.

**KARSTAQUIFER speedup** To get a rough estimate on the parallel performance of KARSTAQUIFER timing routines were implemented into the program. The total calculation time of one time step as well as the time needed by the solver was measured for different amounts of processors $N$. The calculations were performed on one cluster node (SRV in Tab. A.1) and the PARDISO solver was used. When using only the sequential version of the solver ($N = 1$) it should be possible with A.1 and A.2 to empirically estimate the parallel fraction $P$ of the program and therefore also derive the maximum possible speedup $SU_{max} = 1/S$. By increasing the number of processors $N$ available to the solver, the real speedup $SU(N)$ can be obtained. The results are shown in Tab. A.3

| **Name** | $T(1)[s]$ | $T_P(1)[s]$ **($P$ [%])** | $SU_{max}$ | $SU(2)$ | $SU(4)$ | $SU(6)$ | $SU(8)$ |
|---|---|---|---|---|---|---|---|
| model1 | 0.308 | 0.008 (2.4) | 1.025 | 0.998 | 1.000 | 1.002 | 0.927 |
| model2 | 0.688 | 0.021 (3.0) | 1.031 | 1.007 | 1.005 | 1.010 | 0.969 |
| model3 | 1.330 | 0.048 (3.6) | 1.037 | 1.000 | 1.010 | 1.006 | 1.005 |
| model4 | 2.311 | 0.108 (4.7) | 1.049 | 1.010 | 0.974 | 1.012 | 1.015 |
| model5 | 4.324 | 0.261 (6.0) | 1.064 | 1.015 | 1.019 | 0.952 | 1.022 |
| model6 | 10.744 | 0.978 (9.1) | 1.100 | 1.026 | 0.949 | 1.044 | 1.046 |
| model7 | 39.284 | 7.118 (18.1) | 1.221 | 1.073 | 1.122 | 1.130 | 1.132 |
| model8 | 109.719 | 34.489 (31.4) | 1.458 | 1.144 | 1.244 | 1.260 | 1.259 |
| model9 | 250.894 | 124.689 (49.7) | 1.988 | 1.263 | 1.485 | 1.511 | 1.462 |
| model10 | 464.681 | 248.916 (53.6) | 2.154 | 1.296 | 1.510 | 1.556 | 1.534 |
| model11 | 614.791 | 354.465 (57.7) | 2.362 | 1.328 | 1.605 | 1.624 | 1.599 |

**Table A.3:** Results of the KARSTAQUIFER speedup test for different model sizes; $T(1)$ calculation time (total) for one time step and one processor; $T_P(1)$ calculation time (only solver) for one time step and one processor; $SU_{max}$ theoretical maximum speedup; $SU(N)$ real speedup for different amounts of processors ($N$)

$T(1)$ is the total sequential calculation time[2] for one time step and correspond to the values already shown in Fig. A.1 (SRV). In the third column the time needed by the solver $T_P(1)$ is given. As this is essentially the parallel fraction $P$ of the program, the corresponding percentage is also given. As the total calculation times

[2]The number 1 denotes that only one processor was used and therefore the program runs in sequential mode.

increase from $\approx 0.3$ [s] for model1 to $\approx 615$ [s] for model11 also the parallel fraction of the program increases significantly. For the larger models ($\geq$model7) the parallel fraction increases from $\approx 18$ [%] to almost 58 [%]. Because the small models only have very little parallel fractions the theoretically possible speedup $SU_{max} \leq 1.1$ is also very small. On the other hand, also for the largest model the maximum possible speedup is only $SU_{max} \approx 2.4$ and can be expected to be even lower in reality.

The last four columns show the measured speedups for $N = 2$, $N = 4$, $N = 6$ and $N = 8$ processors respectively. For the small models ($\leq$model6) the use of more processors shows now significant improvement. Actually, due to the overhead produced by using more cores, the parallel performance can be even worse than the sequential one with $SU(N)$ smaller than 1. The highest speedup for every model is marked with red color in Tab. A.3. For the larger models ($\geq$model8) the speedup increases with the increase of available processors up to $N = 6$. If more processors are used the speedup drops again which can be due to internal *friction losses* caused by the increased costs for interprocess communication.

Tab. A.3 also shows what is know in computational science as Gustafson's law Bauke and Mertens (2006)

$$SU(N) = S + N \cdot P, \tag{A.4}$$

which is an extension of Amdahl's law in A.1. It states that the speedup increases linearly with increasing $N$, as long as also the parallel fraction of a program increases and therewith consequently the model size has to increase. The rows of Tab. A.3 correspond to the consequences of Amdahl's law that the speedup for a given problem is limited by the sequential fraction of the program. Whereas the columns of Tab. A.3 correspond to Gustafson's law, that if the model size increases also the speedup increases.

**PARDISO performance** To evaluate the parallel performance of the PARDISO solver Fig. A.2a shows only the speedup of the parallel fraction of the program, the solver routine. The speedup is shown as a function of available processors $N$ for models $\geq$model7. For all shown models the speedup increases significantly when using two processors instead of one. The speedup is close to the ideal speedup (dashed line) and is for models $\geq$model8 $\approx 1.7$. Increasing the number of processors to four the speedup still increases significantly. For model7 and model8 it is less

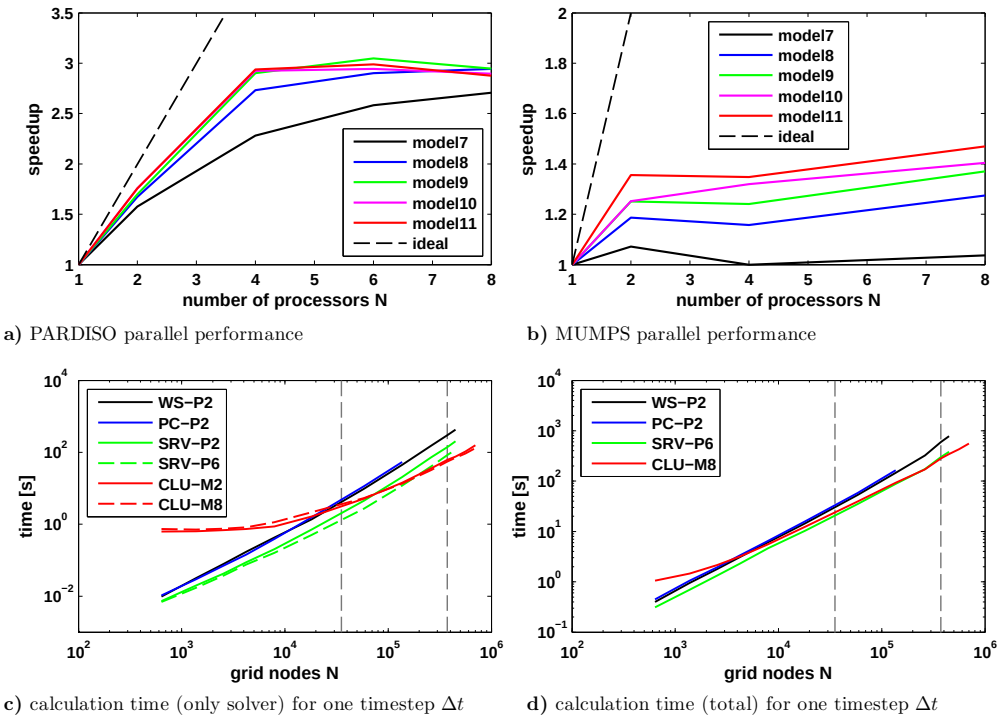


**a)** PARDISO parallel performance

**b)** MUMPS parallel performance

**c)** calculation time (only solver) for one timestep $\Delta t$

**d)** calculation time (total) for one timestep $\Delta t$

**Fig. A.2:** **a)** PARDISO parallel performance (speedup as a function of processors); **b)** MUMPS parallel performance (speedup as a function of processors / nodes); **c)** comparison of calculation times (only for the solver) as a function of grid nodes, for different hardware platforms and sparse solvers; **d)** comparison of total calculation times for one time step as a function of grid nodes, for different hardware platforms and its best performing sparse solver; For the model parameters (**a+b**) see Tab. A.2, for the abbreviations (**c+d**) see Tab. A.1

pronounced but still noteworthy. For models ≥model9 the speedup is ≈ 3 and therewith 75% of the ideal speedup. For $N = 6$ the speedup almost remains static with only a slight increase and for $N = 8$ the speedup already decreases for the larger models (≥model9).

**MUMPS performance** A similar speedup test was done for the MUMPS solver and the results of its parallel performance are shown in Fig. A.2b. Note that because MUMPS is used on a computer cluster, the number of processors now corresponds to the number of cluster nodes. For all models shown here, the speedup increases when using two nodes instead of one but is smaller compared to PARDISO (maximum

of $\approx 1.4$ for model11). For $N = 4$ nodes the speedup decreases for all models but model10 and increases again when $N = 8$. Generally, excluding model7 as it is too small to gain from more nodes, the larger the model size the higher is the speedup, even though it is quite small.

At a first glance these results look much worse compared to the PARDISO solver but they can be explained quite well with the inherent differences of both solvers. As PARDISO runs on shared memory machines (one computer) and MUMPS preferably on distributed memory machines ($X$ computers), the bottleneck when increasing the number of processors is the communication between them. This is of course orders of magnitude slower when done over the network (MUMPS) and not internally (PARDISO). But this network limiting effect levels out and even switches when the model size is significantly increased. This effect is shown in Fig. A.2c. There, the calculation times for the two solvers and the four hardware platforms are compared. The abbreviations correspond to the ones given in Tab. A.1 and P$X$ and M$X$ refer to PARDISO and MUMPS with $X$ processors respectively. For small model sizes (grid with $\leq 2 \cdot 10^4$ nodes) the PARDISO solver on one computer is always faster than MUMPS on a computer cluster due to the communicational *friction losses*. Furthermore, the PARDISO performance is strongly platform dependent and the speedup for the solver routine can increase up to a factor of 3 when using $N = 6$ processors. When the model size increases (grid with $\geq 10^5$ nodes) the MUMPS solver is already faster with two nodes than PARDISO with $N = 6$. And this difference increases with increasing model size and available nodes. For model13 MUMPS with two nodes is as fast as PARDISO with two cores for model10 but both models differ by a factor of two. Note that the two largest models (model12 and model13) could only be solved on the computer cluster.

### A.1.3 Summary of KARSTAQUIFER *benchmark* tests

The results of the above described *benchmark* tests are summarized in Fig. A.2d. There the calculation time for one time step is shown for the four different hardware platforms each with the fastest (possible / tested) solver implementation. It was shown that KARSTAQUIFER can be used on a variety of hardware platforms and that even a normal desktop computer can be used to simulate averagely sized karst evolution models in a reasonable amount of time. For the model sizes used in this work with grid sizes between $\approx 30\,000$ and $\approx 1\,000\,000$ nodes the use of a server or

cluster is recommended as there the calculation is up to three times faster.

There is no significant difference in using one server and the PARDISO solver (green line) or a computer cluster with the MUMPS solver (red line). The relatively high speedup due to parallelization of the PARDISO solver (Fig. A.2a) compared to the MUMPS solver (Fig. A.2b) is leveled out by the better performance of MUMPS for large models ($\geq 10^5$ nodes, Fig. A.2c) and the communicational *friction losses* due to a limited network bandwidth. Note that when the simulations are performed on the computer cluster, the data for storing the results has also to be transported over the network which additionally slows down the overall calculation time.

The limiting criteria for the model size in this work especially for the models shown in chapters 4 and 5, was the needed disk space for storing the simulation results and exploiting the data. Nevertheless, it was shown that KARSTAQUIFER has the capabilities of handling large models and can therewith benefit from future hardware and software improvements.

## Appendix B

# Additional 3D doline plots

## B.1 Model 2 – two passages, one active crushed zone

### B.1.1 Model 2 – blocky collapsing

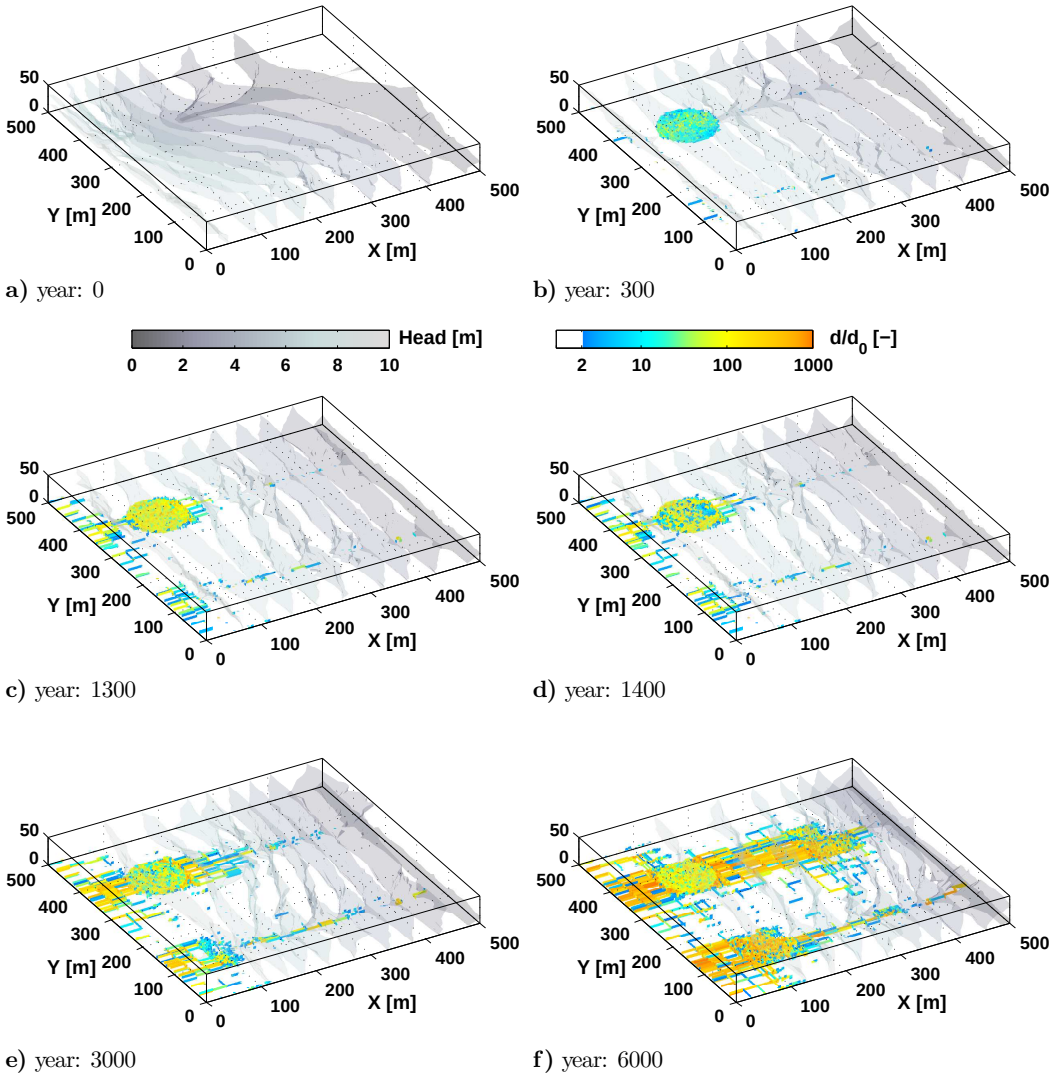


**a)** year: 0 **b)** year: 300

**c)** year: 1300 **d)** year: 1400

**e)** year: 3000 **f)** year: 6000

**Fig. B.1:** Conduit diameter evolution of the 3D doline model 2 (blocky collapsing) for different snapshots in time; Below each subplot the year is given; plotted are the isosurfaces of constant head from low (dark grey) to high (light grey) values and the relative increase of the conduit diameter compared to the initial diameter on a log–scale from 2 (blue) to $\geq 1000$ (orange).

### B.1.2 Model 2 – layered collapsing

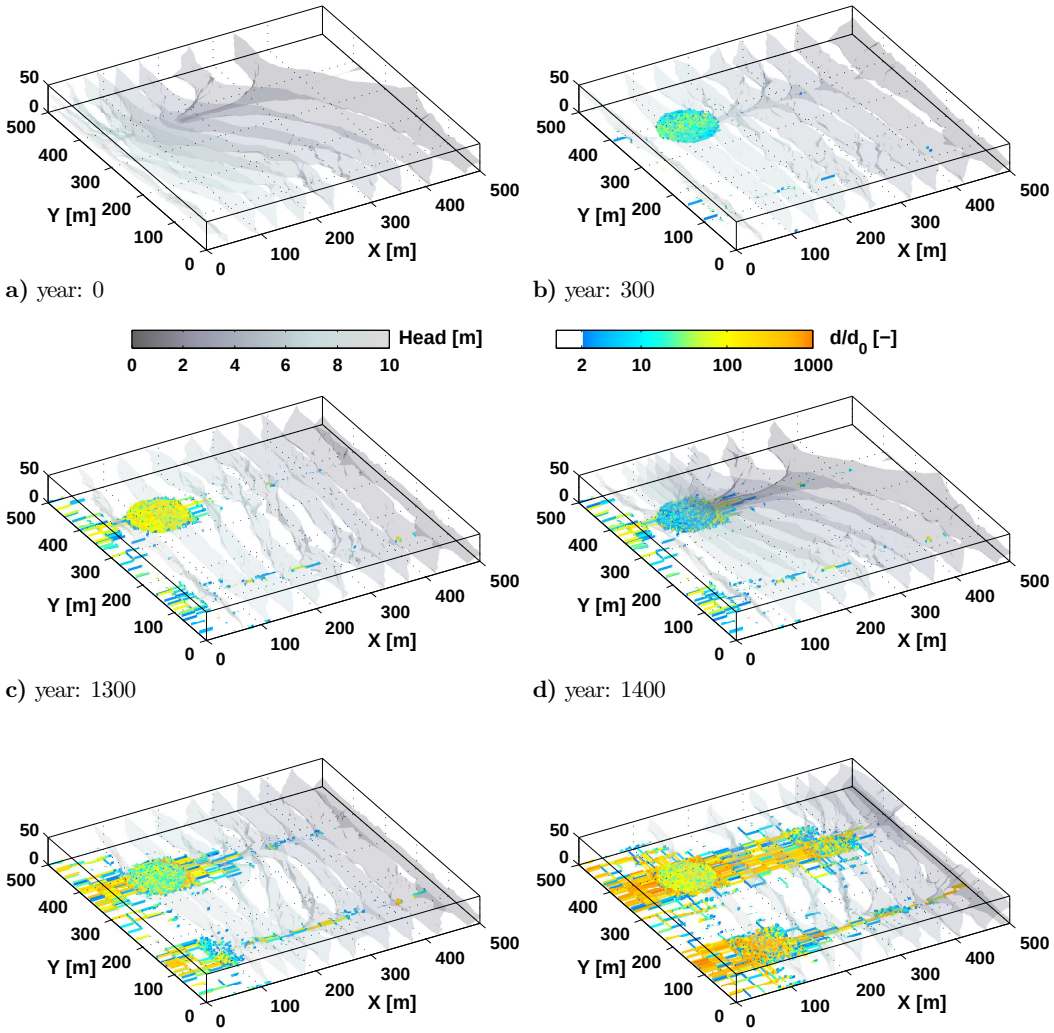


**a)** year: 0 **b)** year: 300

**c)** year: 1300 **d)** year: 1400

**e)** year: 3000 **f)** year: 6000

**Fig. B.2:** Conduit diameter evolution of the 3D doline model 2 (layered collapsing) for different snapshots in time; Below each subplot the year is given; plotted are the isosurfaces of constant head from low (dark grey) to high (light grey) values and the relative increase of the conduit diameter compared to the initial diameter on a log–scale from 2 (blue) to $\geq 1000$ (orange).

### B.1.3 Model 2 – total collapsing

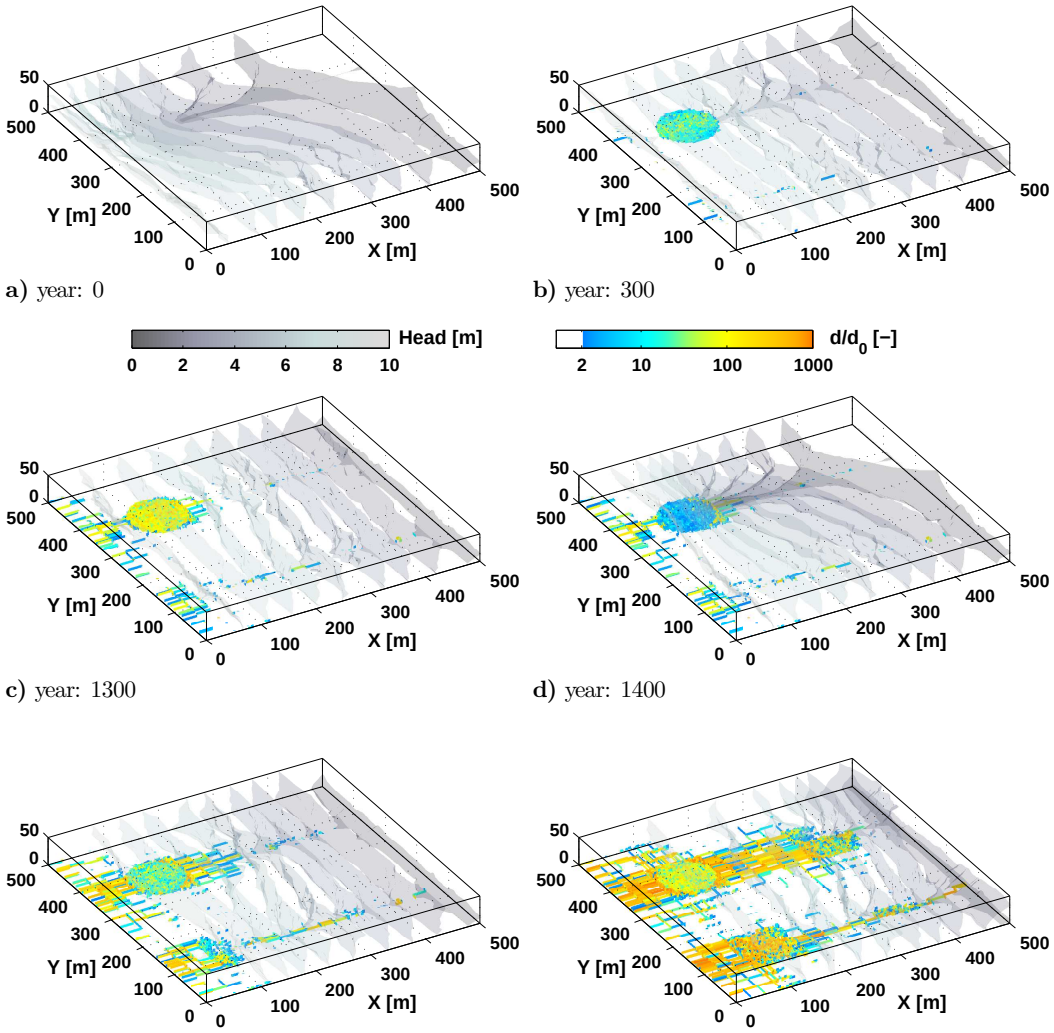


**a)** year: 0 **b)** year: 300

**c)** year: 1300 **d)** year: 1400

**e)** year: 3000 **f)** year: 6000

**Fig. B.3:** Conduit diameter evolution of the 3D doline model 2 (total collapsing) for different snapshots in time; Below each subplot the year is given; plotted are the isosurfaces of constant head from low (dark grey) to high (light grey) values and the relative increase of the conduit diameter compared to the initial diameter on a log–scale from 2 (blue) to $\geq 1000$ (orange).

## B.2 Model 3 – two passages, two active crushed zones

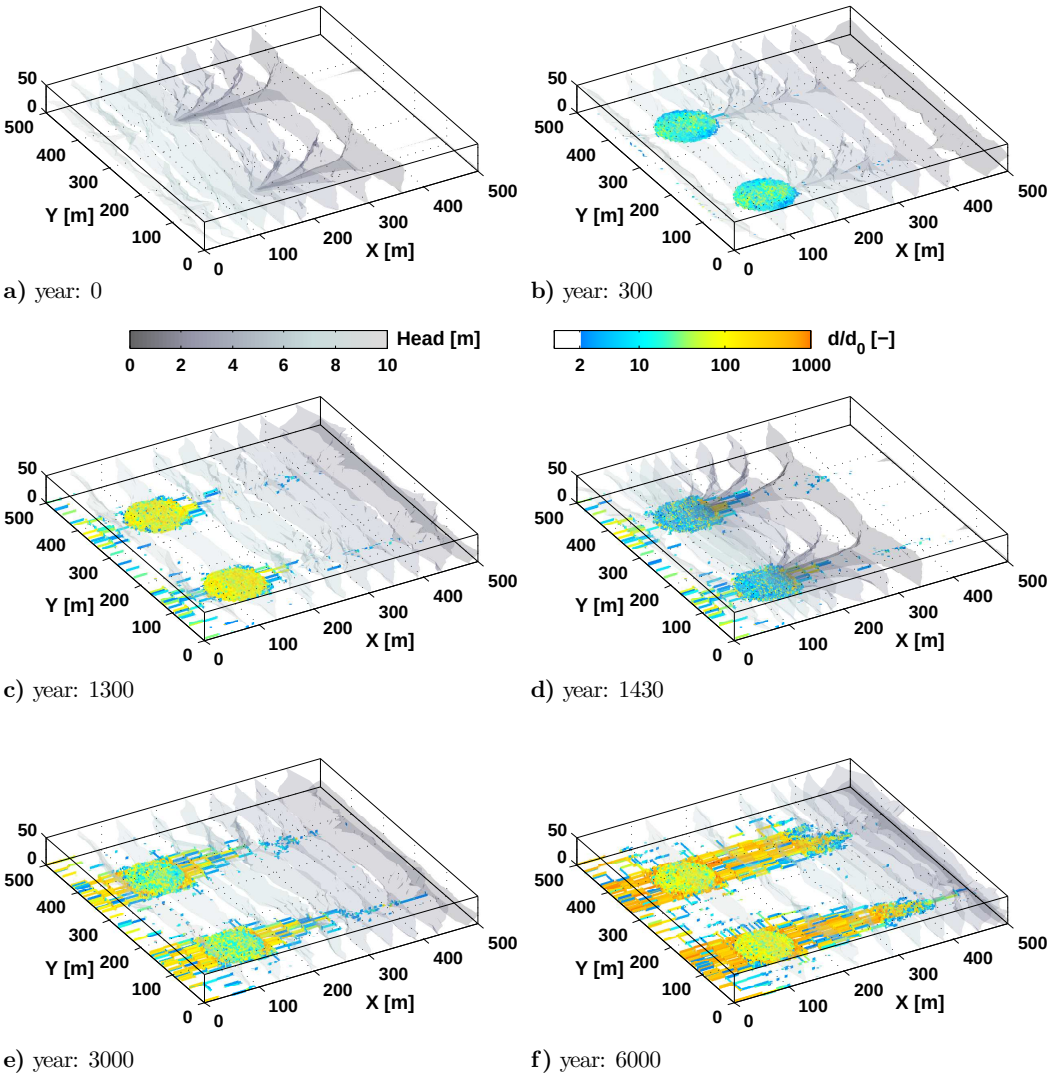


**a)** year: 0 **b)** year: 300

**c)** year: 1300 **d)** year: 1430

**e)** year: 3000 **f)** year: 6000

**Fig. B.4:** Conduit diameter evolution of the 3D doline model 3 (layered collapsing) for different snapshots in time; Below each subplot the year is given; plotted are the isosurfaces of constant head from low (dark grey) to high (light grey) values and the relative increase of the conduit diameter compared to the initial diameter on a log–scale from 2 (blue) to $\geq 1000$ (orange).

### B.2.1 Model 3b – two passages, two active crushed zones

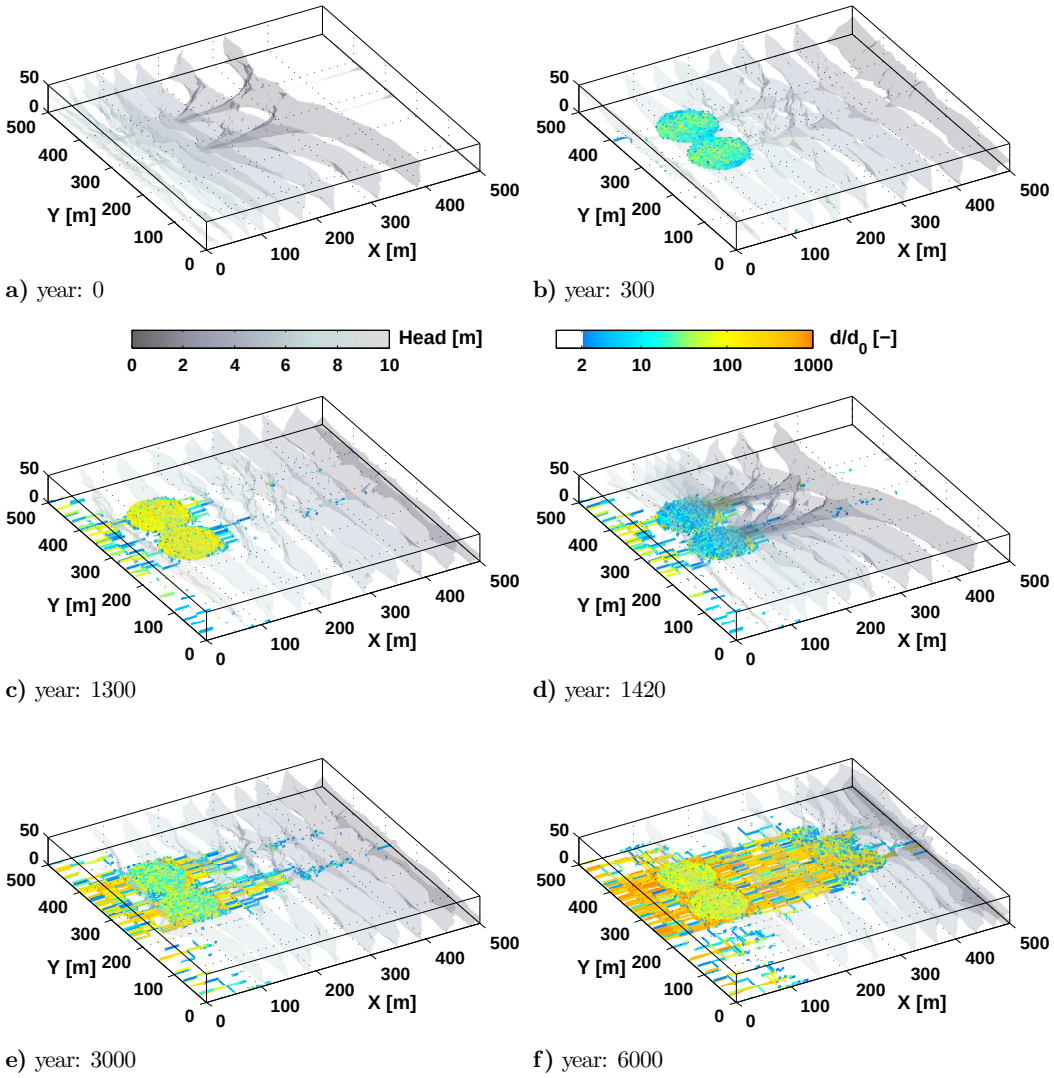


**a)** year: 0 **b)** year: 300

**c)** year: 1300 **d)** year: 1420

**e)** year: 3000 **f)** year: 6000

**Fig. B.5:** Conduit diameter evolution of the 3D doline model 3b (layered collapsing) for different snapshots in time; Below each subplot the year is given; plotted are the isosurfaces of constant head from low (dark grey) to high (light grey) values and the relative increase of the conduit diameter compared to the initial diameter on a log–scale from 2 (blue) to $\geq 1000$ (orange).

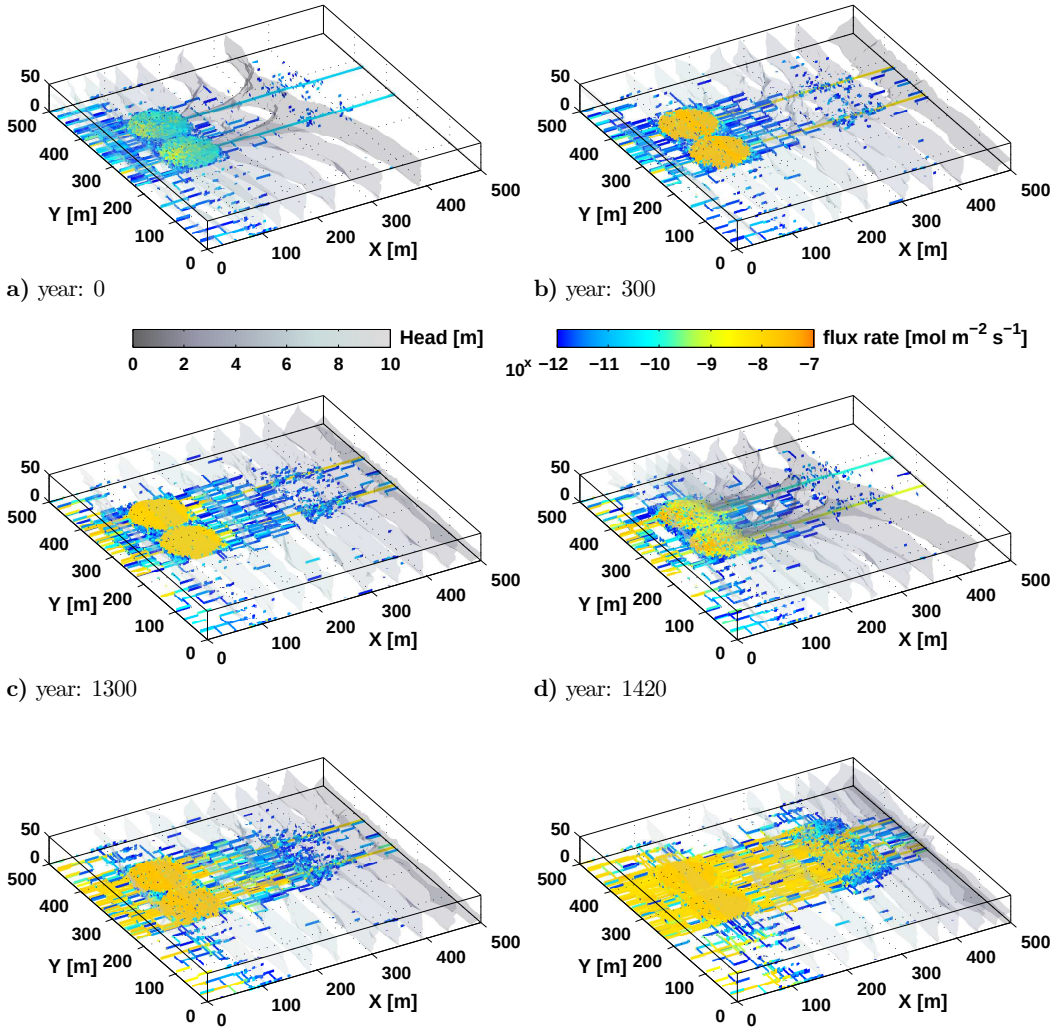


**a)** year: 0 **b)** year: 300

**c)** year: 1300 **d)** year: 1420

**e)** year: 3000 **f)** year: 6000

**Fig. B.6:** Flux rate evolution of the 3D doline model 3b (layered collapsing) for different snapshots in time; Below each subplot the year is given; plotted are the isosurfaces of constant head from low (dark grey) to high (light grey) values and the flux rates inside the conduit on a log–scale from $10^{-12}$ [mol m$^{-2}$ s$^{-1}$] (blue) to $10^{-7}$ [mol m$^{-2}$ s$^{-1}$] (orange).

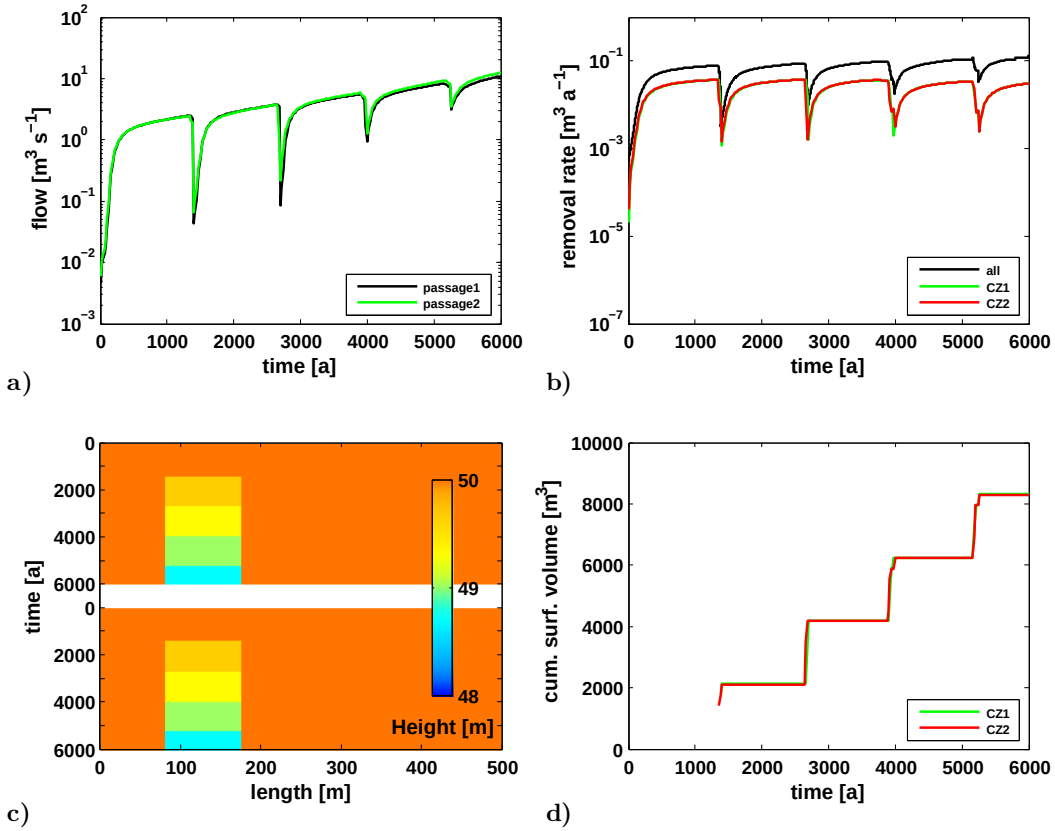


**Fig. B.7:** Results for 3D doline model 3b (layered collapsing); **a)** flow rates at the output of passage 1 (black) and passage 2 (green); **b)** removed material per year for all conduits (black curve) and only conduits inside crushed zones CZ1 (green) and CZ2 (red); **c)** height *spectra* along a surface profile above passage 1 showing the surface lowering over time; **d)** estimated cumulative loss of surface volume for CZ1 (green) and CZ2 (red);

## B.3 Model 4 – two passages, three active crushed zones

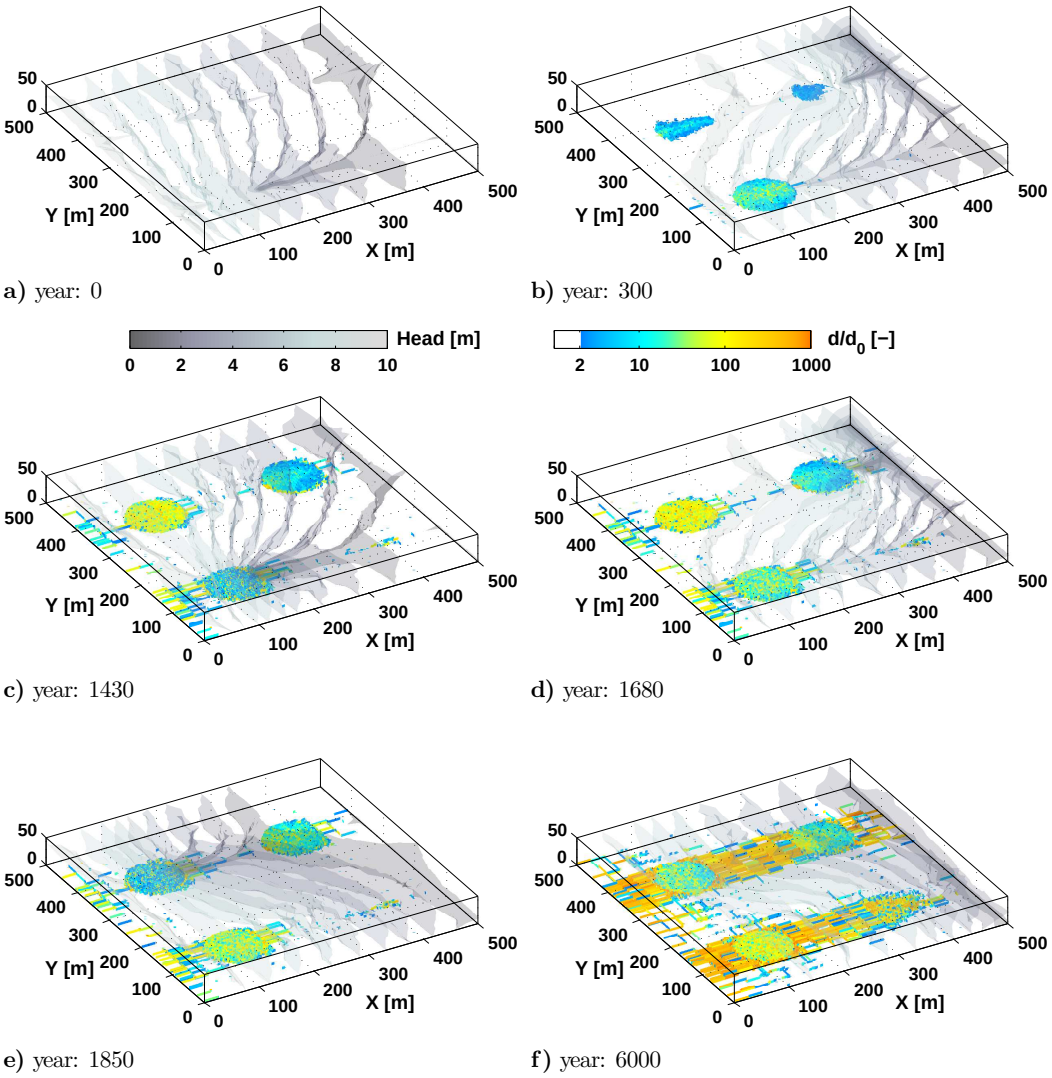


**a)** year: 0 **b)** year: 300

**c)** year: 1430 **d)** year: 1680

**e)** year: 1850 **f)** year: 6000

**Fig. B.8:** Conduit diameter evolution of the 3D doline model 4 (layered collapsing) for different snapshots in time; Below each subplot the year is given; plotted are the isosurfaces of constant head from low (dark grey) to high (light grey) values and the relative increase of the conduit diameter compared to the initial diameter on a log–scale from 2 (blue) to $\geq 1000$ (orange).

### B.3.1 Model 4b – two passages, three active crushed zones

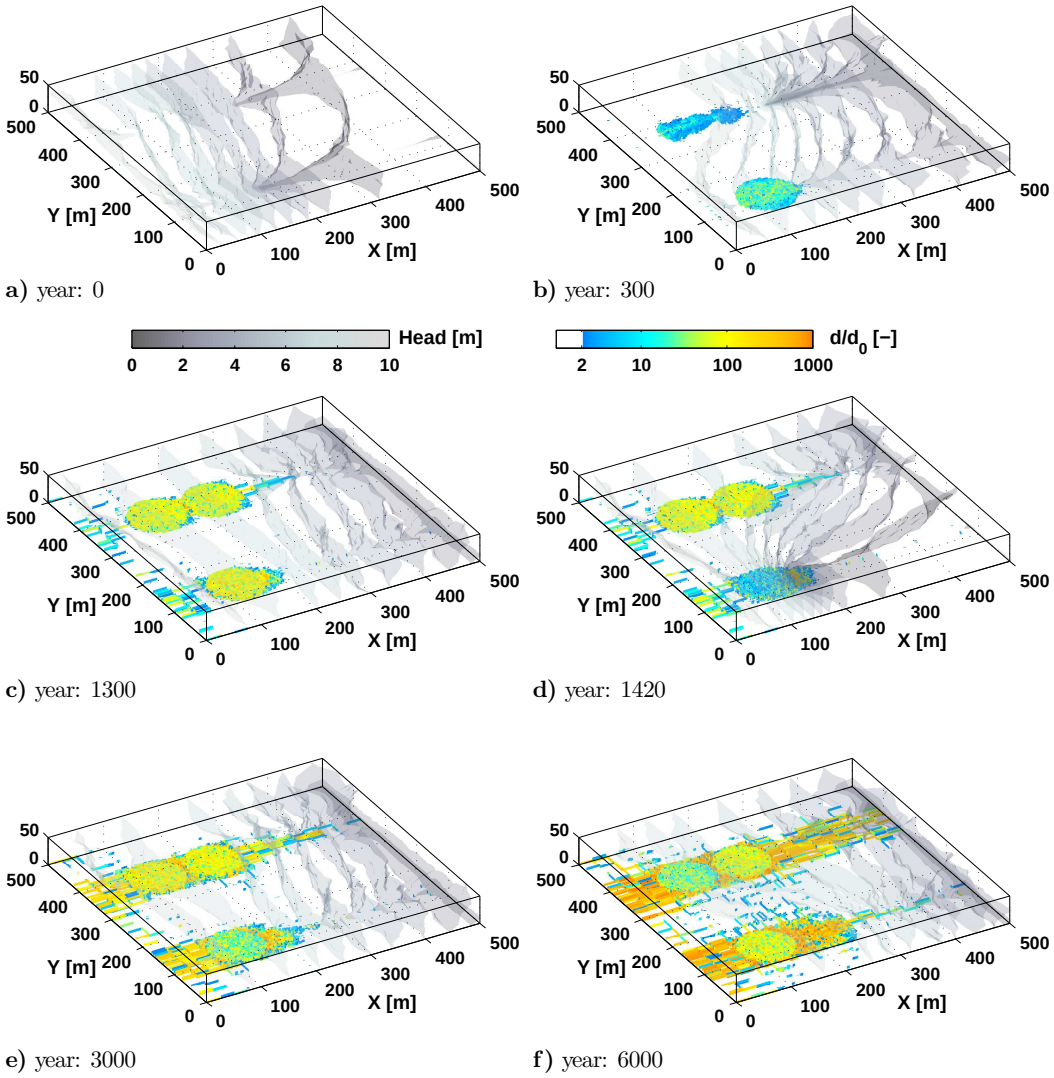


**a)** year: 0 **b)** year: 300

**c)** year: 1300 **d)** year: 1420

**e)** year: 3000 **f)** year: 6000

**Fig. B.9:** Conduit diameter evolution of the 3D doline model 4b (layered collapsing) for different snapshots in time; Below each subplot the year is given; plotted are the isosurfaces of constant head from low (dark grey) to high (light grey) values and the relative increase of the conduit diameter compared to the initial diameter on a log–scale from 2 (blue) to $\geq 1000$ (orange).

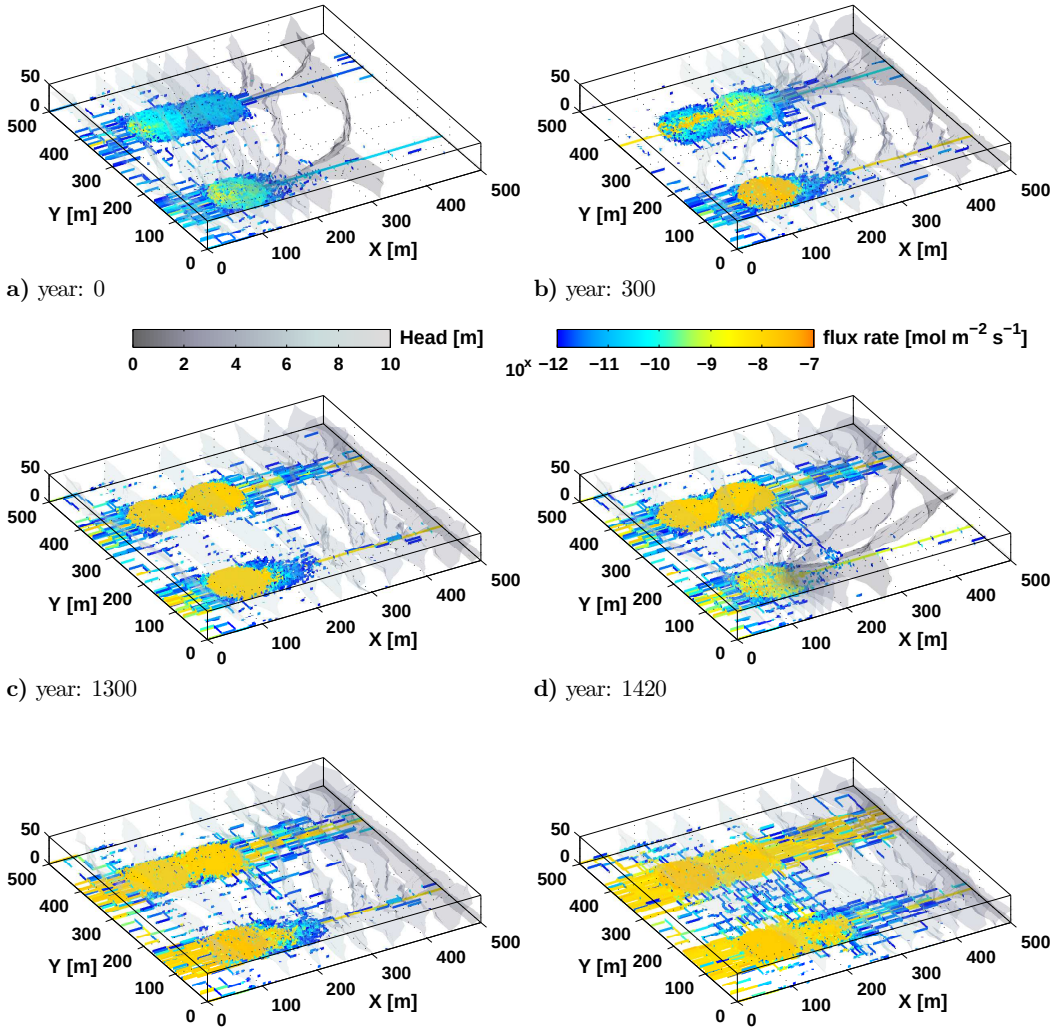


**a)** year: 0 **b)** year: 300

**c)** year: 1300 **d)** year: 1420

**e)** year: 3000 **f)** year: 6000

**Fig. B.10:** Flux rate evolution of the 3D doline model 4b (layered collapsing) for different snapshots in time; Below each subplot the year is given; plotted are the isosurfaces of constant head from low (dark grey) to high (light grey) values and the flux rates inside the conduit on a log-scale from $10^{-12}$ [mol m$^{-2}$ s$^{-1}$] (blue) to $10^{-7}$ [mol m$^{-2}$ s$^{-1}$] (orange).

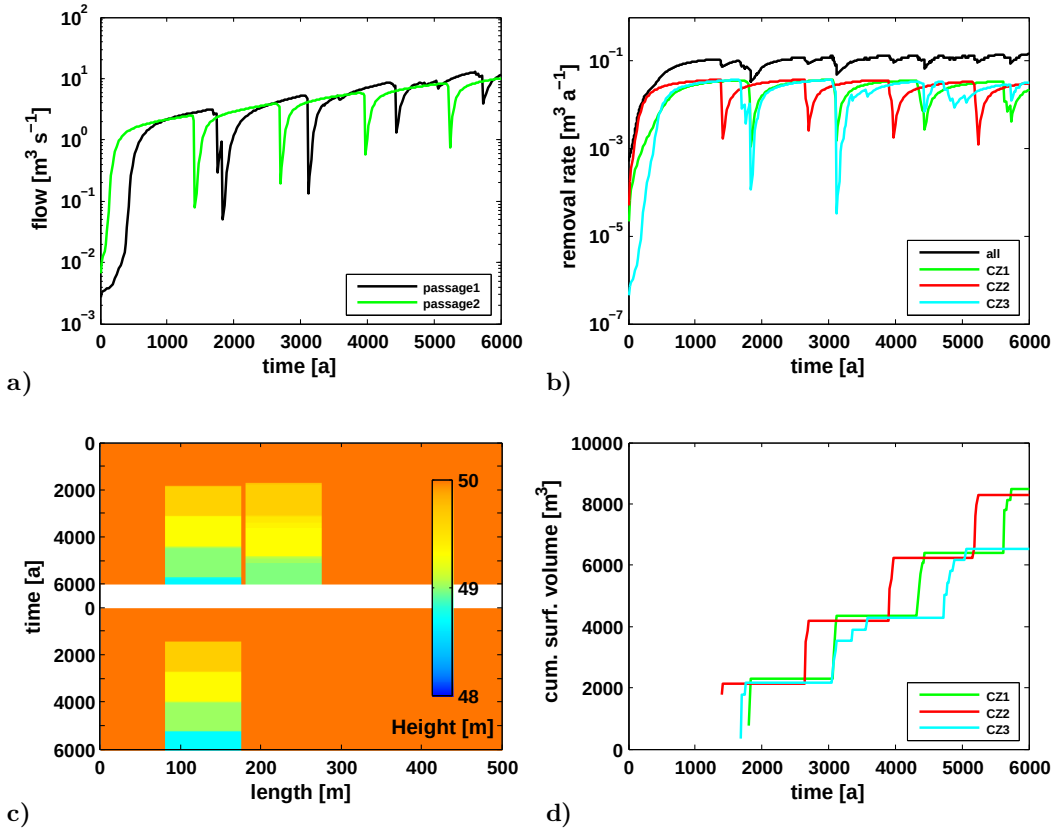


**Fig. B.11:** Results for 3D doline model 4b (layered collapsing); **a)** flow rates at the output of passage 1 (black) and passage 2 (green); **b)** removed material per year for all conduits (black curve) and only conduits inside crushed zones CZ1 (green), CZ2 (red) and CZ3 (cyan); **c)** height *spectra* along surface profiles above passage 1 (top) and passage 2 (bottom) showing the surface lowering over time; **d)** estimated cumulative loss of surface volume for CZ1 (green), CZ2 (red) and CZ3 (cyan);

## Appendix C

# The Karst model creator – KARSTTOOL

When dealing with 3D modelling without a commercial software, a practical way of handling large models is often not available. The program KARSTAQUIFER, used in this thesis is an internal development and based on a 2D program that was extended into the third dimension. See e.g. Kaufmann and Braun (1999, 2000); Kaufmann (2002, 2003a,b,c); Kaufmann and Romanov (2008) for earlier 2D applications and Kaufmann (2009); Kaufmann et al. (2010) for 3D models respectively. From a certain model size on, together with a certain degree of model complexity it is no longer feasible to create the model setup manually. The process has to be automated and all input parameters have to be easily checkable before the time consuming computations are started. For this purpose the software KARSTTOOL was developed. The following pages give a little overview of the capabilities of KARSTTOOL.

## C.1 KARSTTOOL – introduction & layout

KARSTTOOL is written in the MATLAB programming language and needs therefore the MATLAB computing environment installed on a local desktop computer or workstation. It can easily be started by typing

```
>> karsttool
```

at the MATLAB command prompt. The opening screen is shown in Fig. C.1. The layout is based on a tabbed document interface. Here, tabs are used to switch between different parts of the GUI within the same main program window. The red frame A marks the menu bar of the GUI were global settings can be applied. The menu entries are explained in Tab. C.1.

The red frame B in Fig. C.1 marks the tab panel where the user can switch between the different GUI panels to define the model properties. These modifiable properties are the domain and topography properties, the boundary conditions, the network and the material properties, respectively. To check the created model the show / plot panel is used. On the examine results panel the user can load the simulation results and examine the various calculated properties like e.g. the head distribution inside the domain, the increase of the conduit diameter or the calcium flux rate. In the following sections, every tab panel is briefly explained on the basis of an example of a 3D model for simulating the evolution of a collapse doline (see chap. 5).

| Main menu | Sub menu | Purpose |
|---|---|---|
| Create | CREATE Karstdata set | starts creation of the model after all parameters are set |
| | SET default GUI data | resets the GUI to the default parameters |
| Import | LOAD Karstdata set | loads a previously saved Karstdata set |
| | LOAD Boundary Condition set | loads a previously saved boundary condition set |
| | LOAD Network property set | loads a previously saved network property set |
| Export | WRITE Karstdata Input Files | writes the KARSTAQUIFER input files to disk (needs CREATE) |
| | SAVE Karstdata set | saves Karstdata set to disk (needs CREATE) |
| | SAVE Boundary Condition set | saves the boundary condition set to disk |
| | SAVE Network property set | saves the network property set to disk |
| Show | Domain | opens a figure window with the domain layout (needs CREATE) |
| | Boundaries | opens a figure window with the boundary conditions (needs CREATE) |
| | Network Statistics | opens a figure window with the network properties (needs CREATE) |

**Table C.1:** KARSTTOOL; menu bar entries and their utilization

## C.2 KARSTTOOL – domain & topography

In Fig. C.1 the red frame C marks the fields were the basic domain properties like domain extent and discretization are set. North is always in increasing x–direction. Since parallelepipedal elements are used the discretization is fixed in the corresponding direction. Each direction can be independently discretized. Every time one of the fields is edited the information section in frame E is updated. In the example in Fig. C.1 the domain is 500 m × 500 m × 50 m with a horizontal discretization of 25 m and a vertical discretization of 5 m respectively. As one can see in Frame C there are more nodes n[−] in each direction as the given discretization requires. This is due to the setting dolina crushed zone in frame D. When modelling the evolution of dolines (see chap. 5) the discretization inside the doline can be locally increased. This feature is of course not fixed to a doline model only. Any region inside the domain can be assigned with a higher resolution. In frame D the first value corresponds to the horizontal discretization the second value to the vertical

discretization, respectively. Frame D also allows for two other special properties to be set. Per default the top z–layer of conduits is excluded as no horizontal conduits can evolve on the surface. For testing purposes however, the top z–layer can be included. Furthermore, all nodes can be *shook*, which means that the elements themselves can have an irregular shape.

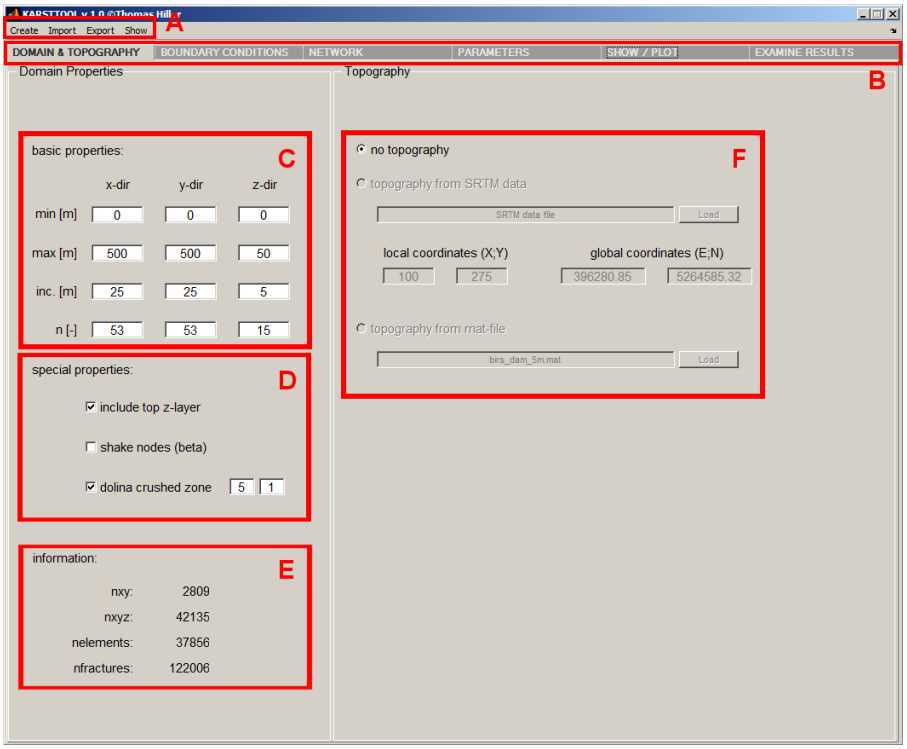


**Fig. C.1:** KARSTTOOL; opening view is the DOMAIN & TOPOGRAPHY tab; red frame A marks the menu bar; red frame B the tab panel respectively; red frames C to F show the different property settings (see C.2 for explanation)

Frame F allows to set the topography of the model. If no topography is set a flat surface at the top layer is assumed. Topography data can be imported in two ways. The first one is by importing a local SRTM[1] data file. Then the topography is linked to the domain via assigning the local coordinates $(X, Y)$ to the global coordinates $(E, N)$ which have to be given as easting and northing values. The Topography values at the surface grid nodes are then interpolated with a cubic

[1] **S**huttle **R**adar **T**opography **M**ission – provides freely available topography data (see Farr et al. (2007))

spline interpolation. The second method is to generate a desired topography in advance and save it as a MATLAB mat–file (data file). The saved topography has to have the same horizontal discretization as given in the basic properties in frame C otherwise an error message is displayed.

## C.3 KARSTTOOL – boundary conditions (BC)

The various BC can be set on the boundary conditions panel (Fig. C.2). Frame A marks the panel for editing the BC. The extent or position of the desired BC is set by the fields xmin [m] to zmax [m]. If a value outside the domain is given the field is reset to the minimal or maximum value of the domain respectively. The boundary type can be one of the following and is chosen via a drop–down list:

- head (constant head BC in [m])
- inflow / outflow (constant flow BC in [$\mathrm{l\,s^{-1}}$])
- calcium (calcium concentration BC, $Ca^{2+}$ in [$\mathrm{mol\,m^{-3}}$])
- rain (precipitation on the surface in [$\mathrm{mm\,a^{-1}}$])
- dam (extent of dam nodes, elements and conduits will be blocked)
- sand (extent of sand nodes, conduits between two sand nodes will be insoluble per default).

The fields value, Ca [mol/m$^3$], T [°C] and pCO2 [atm] have to be set according to the chosen BC. For instance constant head and constant flow BC can also have an initial calcium concentration but for a fixed calcium BC the value field is obsolete. With the LOAD button a previously saved BC file can be loaded (only for one single BC). The tag field is for assigning a unique name to the BC within the BC data set. This name is shown in the list box (frame B). The comment field is for storing comments for the chosen BC. The ADD / UPDATE button adds a newly defined BC to the local set or updates an edited already existing BC. For loading a previously stored BC set the LOAD SET button is used. It has the same function as the IMPORT menu bar. Respectively, SAVE SET is used to save the BC set to the disk. By this feature predefined BC sets can easily be applied to the model. The list box in frame B provides a context menu to either load the chosen BC to the editable field in frame

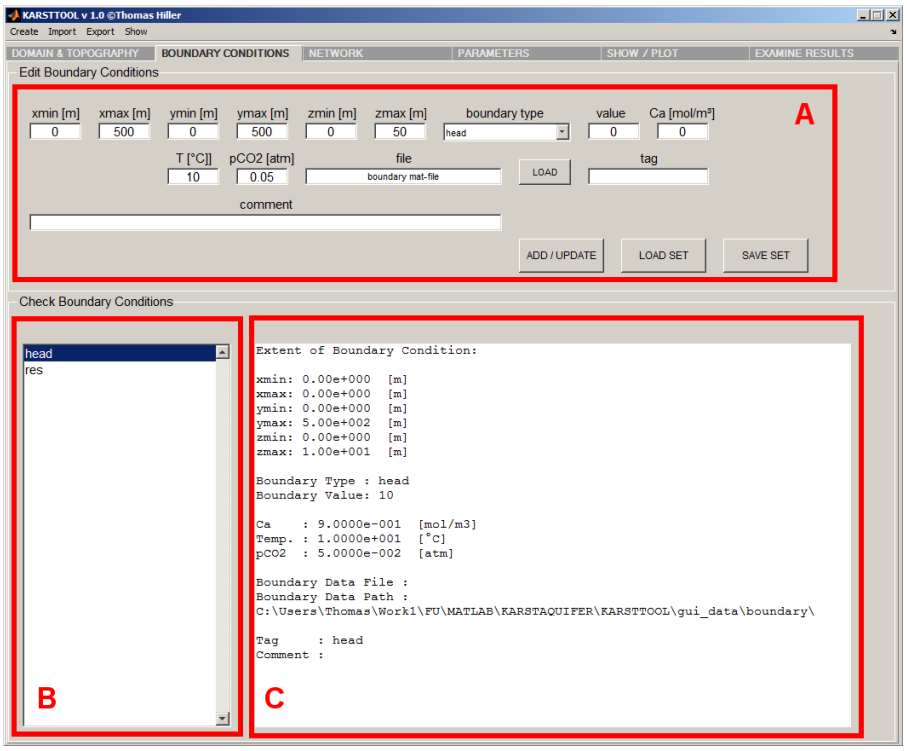


**Fig. C.2:** KARSTTOOL; BOUNDARY CONDITIONS tab; red frame A marks the edit panel where the boundary conditions properties can be set; red frame B is a list box where the created boundary conditions are shown by their tag name; red frame C is the information panel where all information for the marked boundary condition (frame B) is shown; (see C.3 for explanation)

A or to delete it. The example in Fig. C.2 shows two BC named head and res. Both are constant head BC and the information for the head BC is shown in frame C. Here, the constant head BC head extends along the South boundary of the domain (xmin = xmax = 0 m; ymin = 0 m and ymax = 500 m) between zmin = 0 m and zmax = 10 m. The hydraulic head is 10 m and the input calcium concentration is $0.9c_{eq}$ [mol m$^{-3}$]. Temperature and carbon–dioxide partial pressure are the standard values as given in Tab. 2.1.

## C.4 KARSTTOOL – network properties

The network properties of the model can be set in the network panel (Fig. C.3). The layout is similar to the boundary conditions panel with three major parts. The

edit panel (frame A), the list box (frame B) and the information panel (frame C). The position of the network property is again set by the fields xmin [m] to zmax [m] in frame A. The properties can either be set to all conduits in a given 3D part of the domain or to the conduits in a 2D layer. Also a 1D conduit *path* can be defined like e.g. a subsurface channel or stream. Again, several conduit properties can be set via a drop–down list:

- homogen. (uniform initial network; all conduits get the same value)
- statistical (statistical initial network; created with log–normal distribution)
- homogen. lim. (uniform network for maximum diameter; all conduits get the same value)
- statistical lim. (statistical network for maximum diameter; created with log–normal distribution)
- insoluble (marker for insoluble conduits)
- crushed zone (in conjunction with the settings on the domain tab (C.2) defines a region with special properties)
- anisotropxy (factor for diameter of conduits in xy–direction)
- anisotropz (factor for diameter of conduits in z–direction).

The fields mode [m], std and insol. [%] change their meaning and are enabled or disabled according to the chosen property. Like for all editable elements in KARSTAQUIFER, tool tips provide the user with the necessary information. The difference from the boundary conditions tab is the ability to use GSLIB[2] by Deutsch and Journel (1997) for creating spatially correlated conduit properties. If GSLIB is activated via the check box, in the three adjacent fields the axes lengths of the correlation ellipse can be given. With the LOAD button a previously saved network property file can be loaded (only for one property). The tag and comment fields are for assigning a unique name to the network property within the property data set and for comments, respectively. Like before, the tag name is shown in the list box (frame B). There, also a context menu is provided for loading the chosen property

[2] **G**eostatistical **S**oftware **Lib**rary – GSLib needs to be installed additionally on the computer

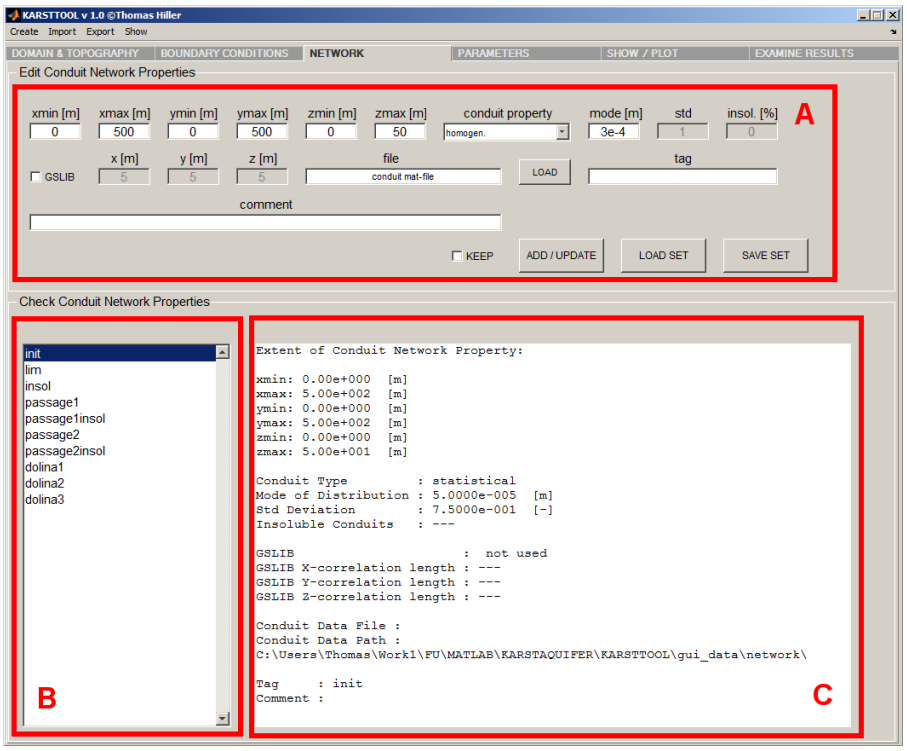


**Fig. C.3:** KARSTTOOL; NETWORK tab; red frame A marks the edit panel where the network properties can be set; red frame B is a list box where the created network properties are shown by their tag name; red frame C is the information panel where all information for the marked network property (frame B) is shown; (see C.4 for explanation)

to the edit panel or to delete it. The ADD / UPDATE button adds a newly defined network property to the local set or updates an edited one. For loading a previously stored property set the LOAD SET button is used. It has the same function as the IMPORT menu bar. Respectively, SAVE SET is used to save the network property set to the disk. By this it is easy to apply different predefined properties to the model.

The first three entries inside the list box init, lim and insol are predefined network properties. They can be edited but not deleted as they are required for any basic Karst evolution model simulated with KARSTAQUIFER. All other properties are superimposed on these three default properties and overwrite the according values. For instance the fourth entry in Fig. C.3 (frame B) passage1 defines a subsurface passage or stream that has a certain increased conduit diameter compared to the

initial network. At the given locations the initial diameters $d_0$ defined in init (here a statistical network created by a log–normal distribution with $\hat{d}_0 = 0.05\text{mm}$ and $\sigma_n = 0.75$) are replaced by the values given in passage1. As in the given example in Fig. C.3 the insoluble property of the whole domain insol is also randomly distributed. The property passage1insol ensures that the passage1 can evolve by dissolution. The same counts for the passage2 property. The properties dolina1 to dolina3 define zones in the domain with different initial conduit diameters and maximum diameters. There the discretization is increased due to the special property dolina crushed zone on the domain tab panel (Fig. C.1 in C.2)

## C.5 KARSTTOOL – parameters

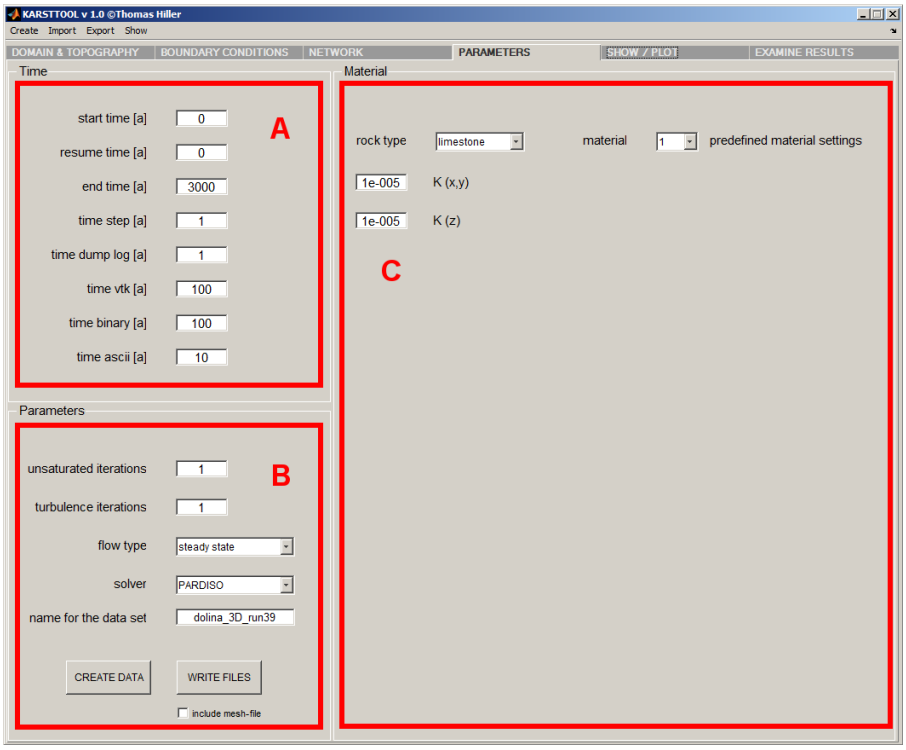


**Fig. C.4:** KARSTTOOL; PARAMETERS tab; red frame A marks the panel where different timing parameters can be set; in red frame B simulation relevant parameters are set; in red frame C material properties can be defined; (see C.5 for explanation)

The parameter tab consists of three main elements (Fig. C.4). On the time

panel (frame A) the start time, end time and the time step can be set. Furthermore, a time interval for updating the KARSTAQUIFER log file as well as time intervals for storing the simulation results on disk (in different data formats) can be set. In frame B the number of iterations to solve the unsaturated groundwater flow equation (optional) can be given. If turbulence is activated the number of iterations can also be set. Furthermore, it is possible to chose between a steady–state or transient groundwater flow model and to chose between PARDISO and MUMPS as sparse matrix solvers. For a comparison of the two solvers see A.1.2.

The material panel (frame C) allows to globally switch the rock type between limestone and gypsum. With a drop–down list predefined material settings can be chosen. Finally, the horizontal and vertical components of the matrix hydraulic conductivity $K_m$ can be defined. In a future version it is planned to assign these material properties also on a local scale. So far this was not needed and is open for future work.

If all settings are made the creation of the Karstdata input set can be started either with the CREATE DATA button in Fig. C.4 (frame B) or via the Create menu in the menu bar. The command prompt provides the user with status information about the generation of the data and when the process is finished. The WRITE FILES button stores the input files on disk and uses therefore the given dataset name as folder name. If the folder already exists a warning messages appears to avoid an accidental deleting of previously generated files.

## C.6 KARSTTOOL – show / plot

The show / plot tab allows for a visual cross check of the various input parameters before they are used for the simulation with KARSTAQUIFER. It consists of two main elements, the control and the plot panel respectively. According to the settings in frame A one of the three domain cross sections can be plotted in the plot panel (frame D) to visualize the grid layout of the model. As an example a small scale picture of KARSTTOOL (E) is shown on top of frame D that shows the current grid layout of the xy–plane. Note the increased horizontal resolution for the regions defined by dolina1 to dolina3 on the network tab panel (Fig. C.3 in C.4). So far as a regular grid / mesh is used the increased discretization is mapped to the whole domain. In a future version the use of irregular meshes is planned.

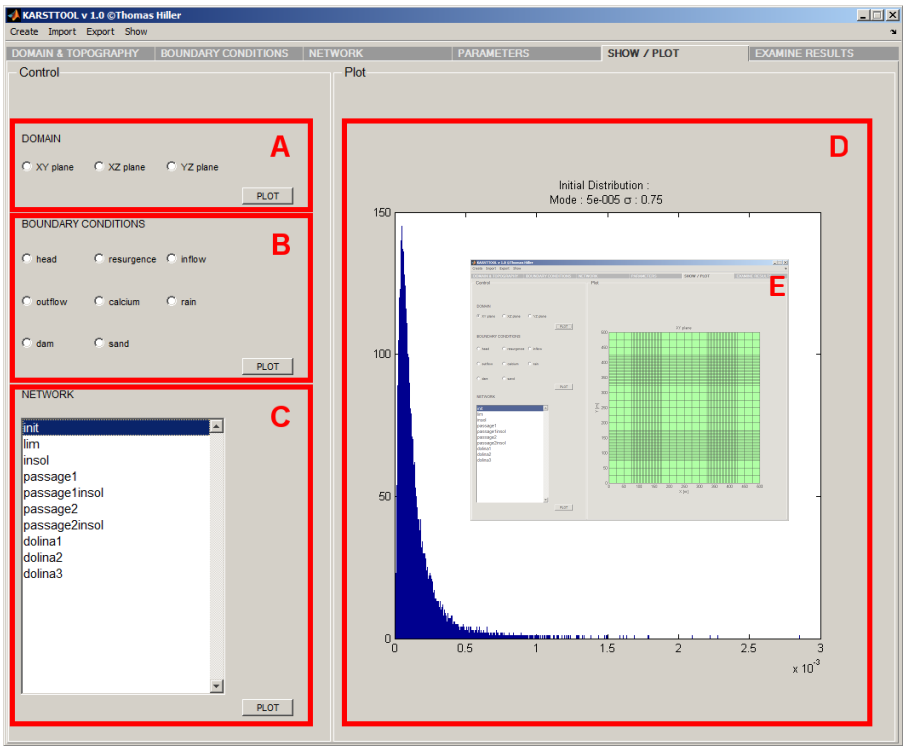


**Fig. C.5:** KARSTTOOL; SHOW / PLOT tab; red frame A is for plotting the grid layout of the domain; red frame B is for plotting the different BC; red frame C is for choosing the network property to be shown; (see C.6 for explanation)

With the radio buttons in frame B it is possible to check the location of the BC inside the model domain. The network properties are visualized with histograms, like e.g. in Fig. C.5 the initial conduit diameter distribution $N_{ln}(\hat{d}_0 = 0.05\text{mm}, \sigma_n = 0.75)$.

## C.7 KARSTTOOL – examine results

Finally, the simulation results can be visualized on the examine results panel. When pressing the LOAD button in frame A a dialog box appears for selecting the directory where the simulation results are stored. The slider is automatically updated with the start and end time of the simulation and is used for selecting the snapshot in time that is shown. This time can also be set in the adjacent field. In the given example 3000 years of evolution have been simulated and the final snapshot in time

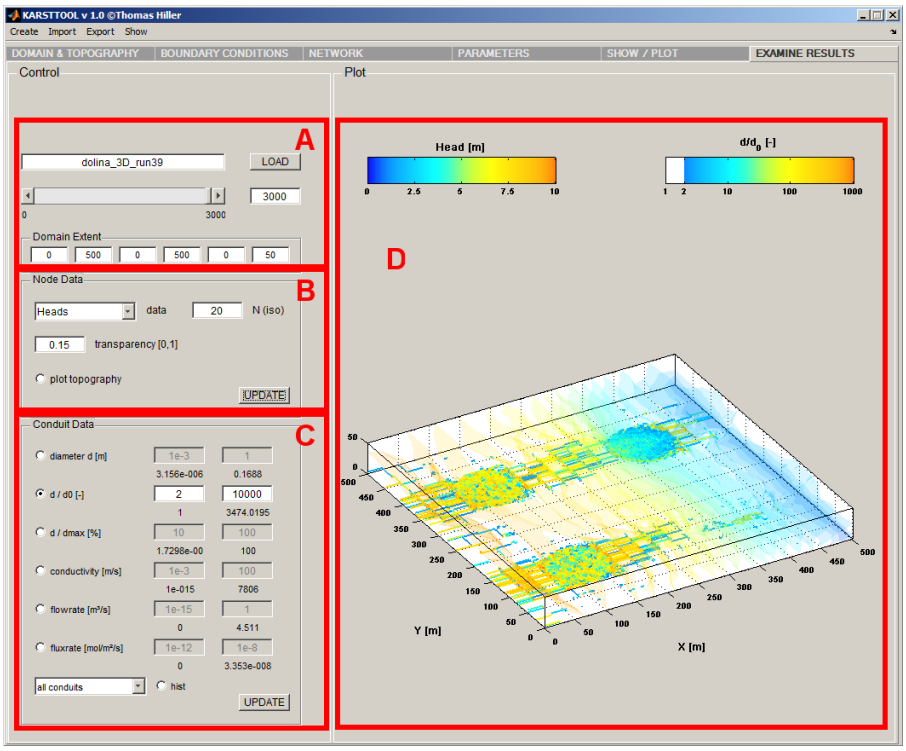


**Fig. C.6:** KARSTTOOL; EXAMINE RESULTS tab; in red frame A the simulation results data set is loaded, the snapshot in time can be chosen and it can be zoomed to a certain part of the domain; in red frame B the node data can be chosen for visualization; in red frame C the corresponding conduit data can be chosen; red frame D contains the plot panel (see C.7 for explanation)

is chosen for visualization. The fields Domain Extent allow for zooming into a certain part of the model.

In frame B the data that was simulated at the nodes of the model (head, calcium concentration or flow) can be chosen via a drop–down list. As this data is plotted along isosurfaces the number of isosurfaces that are linearly spread between the minimum and maximum value can be set. Because normally also some conduit data is plotted the isosurfaces have to be transparent. The value can be set between 0 – completely transparent and 1 – no transparency. In the example 20 isosurfaces of constant head are shown with a transparency of 0.15. The minimum is 0 m (blue) and the maximum 10 m (orange). Every time one of the two UPDATE buttons is pressed the figure in frame D is redrawn.

The conduit data to be plotted is chosen in frame C. This can be one of the

following:

- current conduit diameter $d$ [m]
- relative increase of conduit diameter $d/d_0$ [−]
- current conduit diameter in regard to the maximum diameter $d/d_{max}$ [%]
- hydraulic conductivity $K_c$ [$\mathrm{m\,s^{-1}}$]
- flow rate $Q$ [$\mathrm{m^3\,s^{-1}}$]
- flux rate $F$ [$\mathrm{mol\,m^{-2}\,s^{-1}}$]

If one of the settings is activated the corresponding fields are enabled. Below the left field the minimum and below the right field the maximum values are given, respectively. There, the desired data range can be defined. Only conduits within this data range are plotted (per conduit and colored according to the color scale). Below the radio buttons a drop–down list allows to select whether all conduits, only the horizontal conduits or only the vertical conduits are plotted. A special feature is the possibility to select more than one conduit property to be shown. If two or more properties are chosen they are connected via a logical conjunction. For instance $d \cap (d/d_0)$ means that only conduits that fulfill both conditions are shown. In the given example only conduits that have at least grown by a factor 2 are shown. Because the given upper limit is bigger than the maximum value virtually all conduits with $d \geq 2d_0$ are shown. This is also expressed by the right color scale in frame D where all values smaller than 2 are blanked out.